

Kristine Marie Halvorsen

Synthesis and Characterization of Small Molecule Semiconductive Materials for Applications in Organic Photovoltaic Devices

Master's thesis in Organic Chemistry

Supervisor: Solon Economopoulos

May 2023



Norwegian University of
Science and Technology

Kristine Marie Halvorsen

Synthesis and Characterization of Small Molecule Semiconductive Materials for Applications in Organic Photovoltaic Devices

Master's thesis in Organic Chemistry
Supervisor: Solon Economopoulos
May 2023

Norwegian University of Science and Technology
Faculty of Natural Sciences
Department of Chemistry



Norwegian University of
Science and Technology

Abstract

In pursuit of new materials for applications in bulk heterojunction organic photovoltaic (BHJ OPV) devices, semiconducting small molecules were synthesized and characterized. A naphthalene diimide based molecule has been designed according to the current design rule recommendations. The acceptor-donor-acceptor type structure of a naphthalene diimide-carbazole-quinoline arrangement is a novel design which aims to optimize electron mobility and interfacial electronic properties. The groundwork for the synthesis of this molecule has been developed, although issues of solubility of the precursor molecules have inhibited the ability to achieve high yields. Recommendations for future methods of alkylation at the imide nitrogen of the NDI core are given in order to facilitate future work.

The second part of this thesis is focused on the quinoline-squaraine based molecules, IDQ-SQ and IDQ-SQ-P, which have been investigated for their application as donor materials. Modifications to synthesis and improvements in purification have improved the yields of these molecules. Photophysical characterization of the absorbance, emission, and quenching behavior was executed in addition to electrochemical characterization. It was found that in spite of IDQ-SQ-P having strong absorbance within the solar spectrum (757 nm, $211,500 \text{ M}^{-1} \text{ cm}^{-1}$), the propensity for aggregation even at low concentrations (10^{-7} M) and frontier orbital energies (HOMO of -3.79 eV and LUMO of -5.05 eV) make it a poor candidate as a donor material.

Sammendrag

Nye halvedende små molykyler har blitt syntisert og karakterisert for potensiell bruk til «bulk heterojunction» organiske solceller (BHJ OPVs). Nafthalendiimid ble valgt for bruk i et akseptor-type molekyl, og designet i henhold til teoretiske designanbefallinger. Den teoretisk oppbygningsmåten, akseptor-donor-akseptor, har blitt anvendt til å designe et naftalendiimid-karbazol-kinolin-basert molekyl som tar sikte på å optimalisere elektronmobilitet og elektroniske egenskaper på grensesnittene. Grunnlaget for syntesen av dette molekylet er utviklet, men problemer med løselighet av forløpermolekylene har hindret høye utbytter. Derfor er anbefalinger for fremtidige metoder for alkylering ved imidnitrogenet i NDI-kjernen beskrevet.

Fokuset i den andre delen av oppgaven er undersøkelse av donormaterialer, laget av kinolin-squaraine-baserte molekyler, IDQ-SQ og IDQ-SQ-P. Utvikling av metoder og opprensing har forbedret utbytte av disse molekylene. Fotofysisk karakterisering av absorbanse, emisjon, og quenching-atferden ble utført i tillegg til elektrokjemisk karakterisering. Det ble funnet at IDQ-SQ-P har sterk absorbanse innenfor synlig-lysspekteret (757 nm, $211,500 \text{ M}^{-1} \text{ cm}^{-1}$), men tendensen til aggregering ved lave konsentrasjoner (10^{-7} M) og de elektroniske nivåene (HOMO på -3,79 eV og LUMO på -5,05 eV) gjør dette til en dårlig kandidat som donormateriale.

Preface

The work of this thesis "Synthesis and Characterization of Small Molecule Semiconductive Materials for Applications in Organic Photovoltaic Devices" was carried out from fall 2022 to spring 2023 at the Norwegian University of Science and Technology's Department of Chemistry under the guidance of Associate Professor Solon Economopoulos.

I would like to thank my support here in Trondheim, the friends I have made in the last two years, and those who support me from afar, my parents and best friend back in the US. Special shout out to kanelbolleonsdag, sometimes the only reason I remembered to take a break and talk to people on long lab days.

Til Farmor

Contents

Abstract	i
Sammendrag	ii
Preface	iii
Contents	iv
Glossary	vii
1 Introduction	1
1.1 <i>Organic photovoltaics</i>	1
1.2 <i>Design rules of organic semiconductors for use in for OPVs</i>	2
1.3 <i>Characteristics of previously investigated materials</i>	4
1.3.1 <i>Fullerenes</i>	4
1.3.2 <i>Naphthalene Diimides</i>	5
1.3.3 <i>Squaraines</i>	6
1.3.4 <i>Quinoline</i>	8
1.4 <i>Effect of donating and withdrawing groups on energy levels</i>	9
1.5 <i>Aggregation and its effects on photophysical properties</i>	10
1.6 <i>Graphene, pi-stacking, and its consequences in optoelectronics</i>	11
1.7 <i>Photophysical characterization methods</i>	13
1.7.1 <i>UV-Visible spectroscopy</i>	14
1.7.2 <i>Photoluminescence spectroscopy</i>	15
1.7.3 <i>Time Correlated Single Photon Counting</i>	17
1.7.4 <i>Cyclic Voltammetry for determination of HOMO and LUMO levels</i>	18
1.8 <i>Aim of the thesis</i>	19
2 Results and Discussion	20
2.1 <i>Naphthalene diimide based acceptor</i>	20
2.1.1 <i>Process for bromination and imidation of naphthalene dianhydride</i>	21

2.1.2	<i>Suzuki couplings of brominated naphthalene diimide</i>	26
2.1.3	<i>Next steps for NDI based small molecule semiconductors</i>	28
2.2	<i>Synthesis and photophysical characterization of squaraine-quinoline based dyes</i>	29
2.2.1	<i>Optimization of synthetic procedures and purification methods</i>	30
2.2.2	<i>Absorbance data and aggregation behavior of IDQ</i>	31
2.2.3	<i>Absorbance and emission of IDQ-SQ and IDQ-SQ-P</i>	34
2.2.4	<i>Solvent effect on emission</i>	36
2.2.5	<i>Energy level determination with cyclic voltammetry</i>	38
2.2.6	<i>Emission quenching behavior</i>	40
2.2.7	<i>TCSPC for determination of time constants and quenching mechanisms</i>	44
2.2.8	<i>Applying photophysical and electrochemical data to possible device function</i>	50
3	Methods	51
3.1	<i>Synthetic methods for molecules based on naphthalenediimide core</i>	52
3.1.1	<i>Immidation of 1,4,5,8-naphthalenetetracarboxylic dianhydride</i>	52
3.1.2	<i>Dibromination of 1,4,5,8-naphthalenetetracarboxylic diimide</i>	52
3.1.3	<i>Alkylation of 2Br-NDI with 2-(Ethyl)-Hexyl bromide</i>	53
3.1.4	<i>Alkylation of 2Br-NDI with Iodo-propane</i>	54
3.1.5	<i>Imidation of naphthalene dianhydride with ethyl hexyl amine</i>	55
3.2	<i>Synthesis of dye based on squaraine core</i>	56
3.2.1	<i>Alkylation of quinoline with iodododecane</i>	56
3.2.2	<i>Di-substitution of squaric acid with 6-bromo- N-dodecyl-2-methyl-quinolinium</i>	56
3.2.3	<i>Suzuki coupling of Pyrene and IDQ-SQ</i>	57
3.3	<i>Preparation of graphene</i>	58
3.3.1	<i>Exfoliation by sonification</i>	58
3.3.2	<i>Quantification with Thermogravimetric Analysis</i>	58
3.3.3	<i>Photophysical characterization</i>	58
3.3.4	<i>Ultraviolet Visible spectroscopy</i>	58

3.3.5	<i>Photoluminescence spectroscopy</i>	58
3.3.6	<i>Time Correlated Single Photon Counting</i>	58
3.3.7	<i>Cyclic Voltammetry</i>	59
4	Conclusion	60
5	References	61
6	Supplemental Information	68

Glossary

^{13}C - heavy carbon isotope

^1H - proton

A - Absorbance

A - Acceptor

alk - alkyl group

BHJ - Bulk HeteroJunction

CE - Counter Electrode

CV - Cyclic Voltammetry

D - Donor

d - Doublet (in NMR)

DBH - 1,3-DiBromo-5,5-dimethylHydantoin

DEA - Diethyl Amine

DMF - N,N-Dimethyl Formamide

dq - Doublet of a Quartet (in NMR)

E - Energy (further descriptors in super-/sub- scripts)

eV - Electron Volt

HOMO - Highest Occupied Molecular Orbital

$h\nu$ - light radiation

I - Intensity

I_0 - Initial intensity

ICT - Intramolecular Charge Transfer

LUMO - Lowest Unoccupied Molecular Orbital

M - molar

m - multiplet (in NMR)

MS - Mass Spectrometry

NDI -Naphthalene Diimide

nm -Nanometer

NMP - N-Methyl-2-Pyrrolidinone

NMR - Nuclear Magnetic Resonance spectroscopy

ns - nanoseconds

opt - Optical

OPV - Organic Photovoltaic

ox - Oxidation

P3HT - Poly 3-Hexyl Thiophene-2,5-diyl

PCE - Power Conversion Efficiency

Pd(OAc)₂ - Palladium (II) Acetate

Pd(PPh₃)₄ - Tetrakis(triphenylphosphine) Palladium (0)

PDI - Perylene Diimide

PL - Photoluminescence

ps - picoseconds

PV - Photovoltaic

RE - Reference Electrode

red - Reduciton

RPM - Revolutions Per Minute

s - Singlet (in NMR)

S₀ - Ground State

S₁ - First Excited State

sept - Septet (in NMR)

Sphos - 2-Dicyclohexylphosphino-2',6'-dimethoxybiphenyl

SQ - Squaraine

T - Transmittence

t - Triplet (in NMR)

TCSPC - Time Correlated Single Photon Counting

THF - TetrahydroFuran

UV - Ultraviolet Light

UV-Vis - Ultraviolet and Visible Light Absorption Spectroscopy

V - potential

V0 - Ground Vibrational State

V1 - First Vibrational State

Voc - Open Circuit Voltage

WE - Working Electrode

τ - Time constant

χ^2 - "goodness" of fit

μg - microgram

1 Introduction

1.1 Organic photovoltaics

Between the climate crisis driven by the use of fossil fuels and the energy crisis driven by socio-political conflicts, the demand for the development of a variety of new energy production methods is only increasing. While all the different ways we use energy in our society will need different solutions, one important area to develop is organic photovoltaics (OPVs). These solar devices, in contrast to their classical, silicate counterparts, have simpler fabrication without the need for cleanrooms, reduced use of precious materials, and the ability to target absorbance of specific parts of the solar spectrum. There is also the potential to offer several advantageous properties like flexibility or transparency that would allow for wearability or more aesthetic integration into architecture.

There have been several generations of organic photovoltaics since the initial discovery of the photovoltaic effect in organic chromophores around the 1960s¹. Some of the first PV devices were based on metal-phthalocyanins, where the chromophore was "sandwiched" between two conducting electrodes. These earliest devices had Power Conversion Efficiencies (PCEs) on the order of 10^{-3} percent², but they were the beginning of what would be a massive field of study for chemistry, materials science, and engineering. Significant improvements came after 1985 when the concept of using two thin-film layers of different dyes was introduced. C. W. Tang reported a PCE of 0.95% for his device consisting of copper phthalocyanine and a perylenebisimide with an extended pi system³. While both of the materials were technically chromophores, one of the dyes was acting as an electron transporting material (or electron acceptor) while the other as a hole transporting material (electron donor). Moving into the 1990s, the impact of semiconducting polymers on optoelectronics was beginning to grow exponentially and polymers as absorbing materials were being studied, however their efficiencies remained low¹. As the physics of the organic solar cells were better understood, it became obvious that the exciton generation and dissociation which leads to the generation of current occurs at the interface of two the donor and acceptor materials, meaning this needed to be maximized. Since its conception, a great deal of focus has stayed on these Bulk Heterojunction (BHJ) photovoltaics. BHJ cells are largely based on the successful intermixing the donor and an acceptor – such that there is increased surface area where the two meet and favorable generation of photocurrent is achieved (figure 1 A).

1.2 Design rules of organic semiconductors for use in for OPVs

In a BHJ device, the energy levels of all the materials in the "sandwich" need to match in a particular way (figure 1 B). The donor is the primary absorber of light and generates the initial hole-electron pair called the exciton. A good donor should be strongly absorbing in the visible light range and have its Highest Occupied Molecular Orbital (HOMO) at an energy compatible with that of the anode to allow for hole transport. On the other side of the device, the acceptor's Lowest Unoccupied Molecular Orbital (LUMO) is what must be higher than the cathode's work function to allow for electron collection.

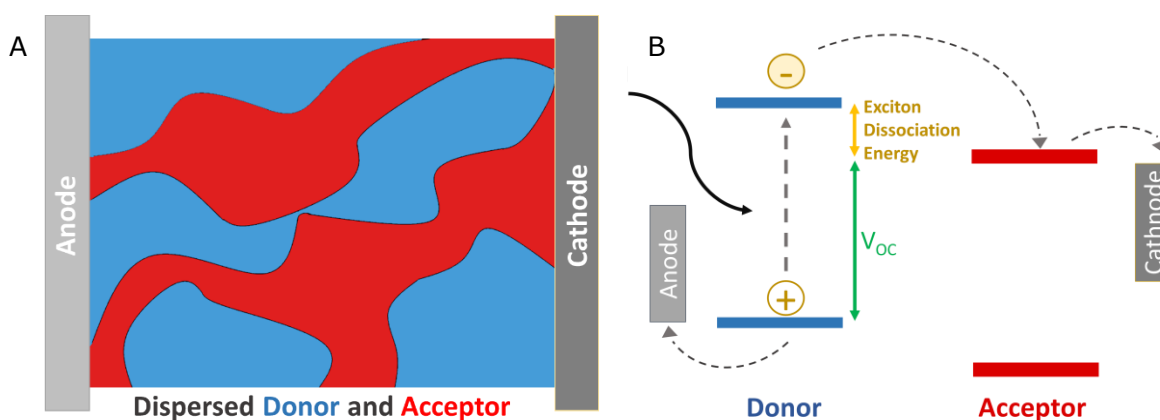


Figure 1: A) illustration of dispersion of donor and acceptor in BHJ devices B) Energy level diagram of each of the components of a BHJ device

As introduced in section 1.1, yet another crucial compatibility aspect is at the interface of the donor and acceptor. The energy of the LUMO of the acceptor must be lower than that of the LUMO of the donor because the difference in energy is the driving force that allows the splitting of the loosely bound exciton to separate the charges. The transfer of the electron from the donor to the acceptor is the dissociation and the difference between the energy levels is termed the Exciton Dissociation Energy.

The above considerations are important when selecting materials that can be paired into a functional device, but there are further design rules to consider when seeking to synthesize new optoelectronic materials. Where there are donor and acceptor materials in the context of BHJs, there are also donor and acceptor moieties within a molecule. While the terminology may seem confusing, the operating principals are consistent between the two contexts; acceptors are electron deficient and have an increased electron affinity while donors are electron rich and have a decreased electron affinity. The way in which these

donor and acceptor moieties are bonded to each other and how their energy levels are allowed to blend determine the overall character of the molecule. For application in OPV devices it has been shown that designs based on alternating acceptor and donor groups yield molecules with desirable optical characteristics, while at the same time allowing for molecular engineering of the HOMO-LUMO levels of the resulting molecule⁴. Some of the reasons for this have to do with electron mobility and exciton dissociation at the phase interface. The electrostatic potentials across an Acceptor-Donor-Acceptor (A-D-A) arranged molecule allows for lattice organization in the bulk phase where pi-pi stacking in parallel or perpendicular orientations minimizes the distance between molecules (figure 2). This organization allows for bending of the energy levels to reduce the bias at the interface of donor and acceptor materials in the BHJ and favorable charge transfer state dissociation.

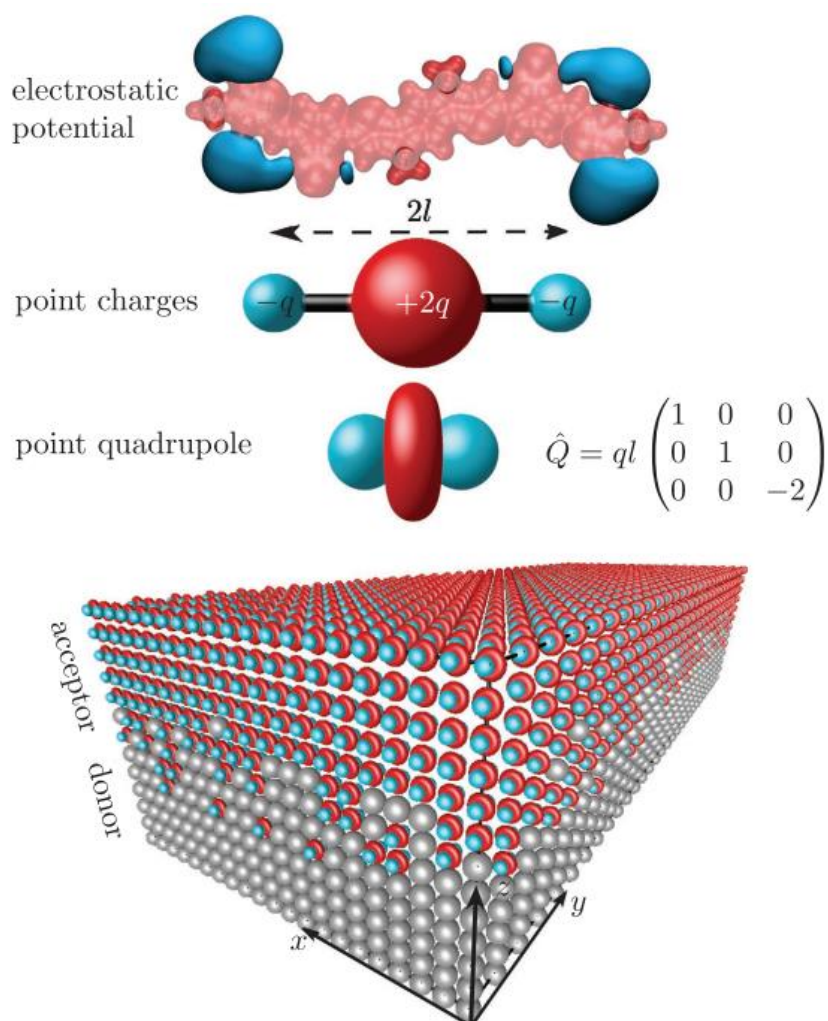


Figure 2: Figure illustrating an A-D-A molecule that behaves as a quadrupolar point charge and how that defines to its self organization in the bulk state and into the interface with a donor material 4.

With these design rules in mind, informed planning of future materials is more effective. Even more understanding could be found by looking at specific donor and acceptor moieties that have been utilized by other researchers in order to identify advantageous behaviors that could be applied to new molecules for BHJ applications.

1.3 Characteristics of previously investigated materials

1.3.1 Fullerenes

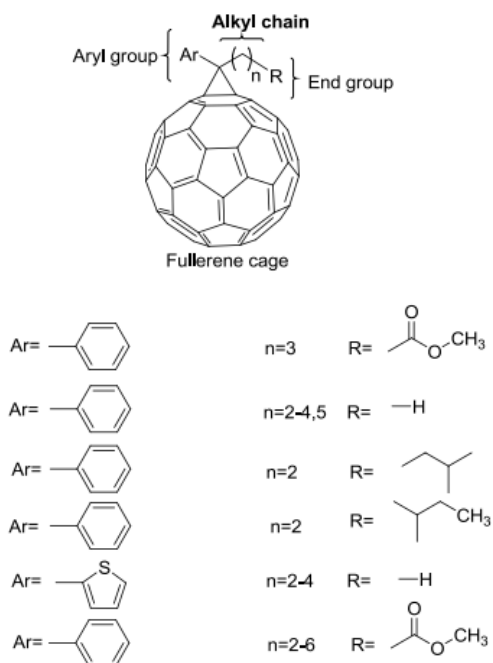


Figure 3: Examples of cyclopropanated fullerene derivatives⁷

Some of the first acceptors that ushered in the concept of polymer-based solar cells and later BHJs were fullerenes^{5,6}: spherical, conjugated carbon nanostructures. Fullerene's high electron affinity, conductance, and low impedance to light passing through the device made it an attractive molecule for BHJ development. One issue with fullerenes, however, is their low solubility. The ability to mix the acceptor and donor materials is necessary when fabricating BHJ cells, so to combat this a large range of functionalizations have been made in order to improve dispersibility. One main way that fullerenes can be substituted is via cyclopropanation reactions, sacrificing one of the double bonds but maintaining the conjugation across the rest of the sphere's surface.

The general substitution pattern of most common substituted fullerenes involves an aryl group and an alkyl group where the chain ends in an ester⁷. With variations in aryl ring type, chain length, and end group identity, a large library of fullerene derivatives have been synthesized and assessed in devices (figure 3). When tested with poly 3-hexyl thiophene-2,5-diyl (P3HT) as a standardized donor polymer, some of these cyclopropyl substituted fullerenes have achieved PCEs between 5-6%. Other substitution types have also been explored, such as Diels-Alder type additions, pyrrolidine addition, and di- or tri- substitutions, where the best candidates have PCEs as high as almost 7% with P3HT.

A common characteristic across fullerene derivatives is their LUMO levels, which vary with substitution but most often lie between -3.5 eV and -4.0 eV. This is why when other acceptor materials are characterized, LUMO levels in this range are cited a good sign. On the other hand, the push to design non-fullerene acceptor molecules stems from the need to access compatibility with other donors and electrode types, improve absorbance in the visible light region, and reduce the cost of the materials.

1.3.2 Naphthalene Diimides

One base molecule that has been investigated for non-fullerene acceptor materials is Naphthalene Diimides (NDIs). These are naphthalenes with cyclic imides which draw electron density from the aromatic rings. While naphthalene has a smaller aromatic system than perylene, previous work had found this to be an advantage of NDIs over Perylene Diimides, as they maintain planarity and resist twisting which is needed for efficient electron transport^{8,9}. Both small molecule and polymer-based NDI acceptors have shown high air and heat stability which are important practical considerations for their use in OPVs¹⁰. Core expanded NDIs tested by *Gao et al.* (figure 4) showed almost no change in their electron mobility when tested before and after 5 weeks in ambient conditions¹¹.

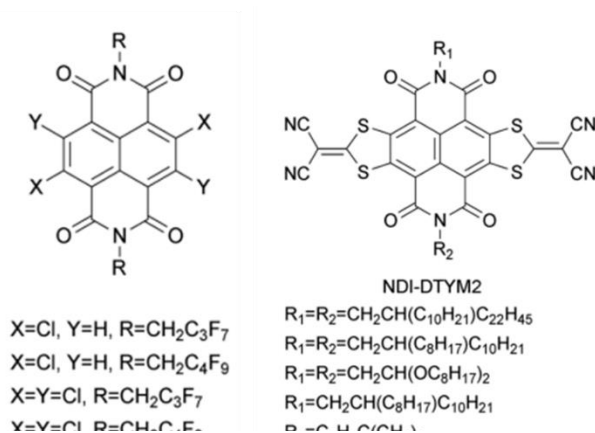


Figure 4: Naphthalene diimide derivatives that have demonstrated high air stability and electron mobility¹⁰.

NDI cores are attractive for the above reasons, while relatively under explored compared to many other electron acceptor moieties and thus were selected as a target in the synthesis of small molecule acceptors for OPVs.

1.3.3 Squaraines

A small, electron deficient cyclobutene based moiety, squaraine has been utilized in a number of dyes intended for optoelectronic applications. They can be substituted both symmetrically and asymmetrically to imbue different properties and are especially fascinating due to their often zwitter ionic structures.

The absorbance properties of squaraine based dyes have the potential to vary widely depending on substitution as evidenced by the set of molecules synthesized by Vuk *et. al.*¹². The four molecules vary at the phenyl by the identity of the para-position amine and having an alcohol or methoxy group at the meta-positions, but these differences have significant consequences with respect to absorbance (figure 5).

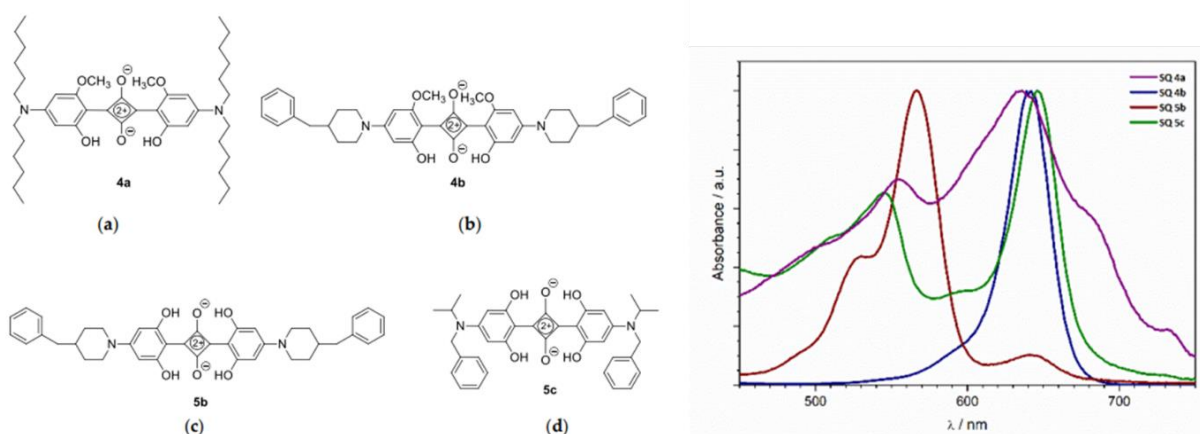


Figure 5: Structures and normalized absorbance spectra of the squaraine based dyes reported by Vuk *et. al.*¹².

When looking at the absorbance spectra of this set of dyes, the maxima of 4a, 4b, and 5c all lie around 640 nm, and absorbances between 600 nm and 700 nm are the target range for applications in OPVs, however the broadness and location of other local maxima are seen to be quite different between these molecules. Interestingly, the dye 4b differs only from 5b by the replacement of one alcohol on each phenyl by a methoxy group, and yet their absorbance maxima differ by approximately 80 nm. The large differences observed may be a result of axes symmetry and the consequences they have on aggregation behaviors. The LUMOs of 4b, 5b, and 5c were reported to be -3.24 eV, -3.52 eV, and -3.68 eV respectively while the energy gaps were 1.66 ± 0.01 eV. These LUMO energies are somewhat higher than the common fullerene acceptors, however this may give them improved charge separation or compatibility with different types of donors.

Some other squaraine dyes substituted with benz(*cd*)indole moieties have been synthesized that are able to absorb strongly into the short-wave infrared region¹³. This low energy absorbance indicates the capability of squaraine dyes to have very narrow energy gaps. They also clearly demonstrate the effect of adding donor end groups – here phenyl, carbazole, and thiophene – on the bandgap, as there is a clear redshift in both absorbance and emission spectra and an increase in absorbance intensity relative to bis-benz(*cd*)indole-squaraine (SQ1) (figure 6).

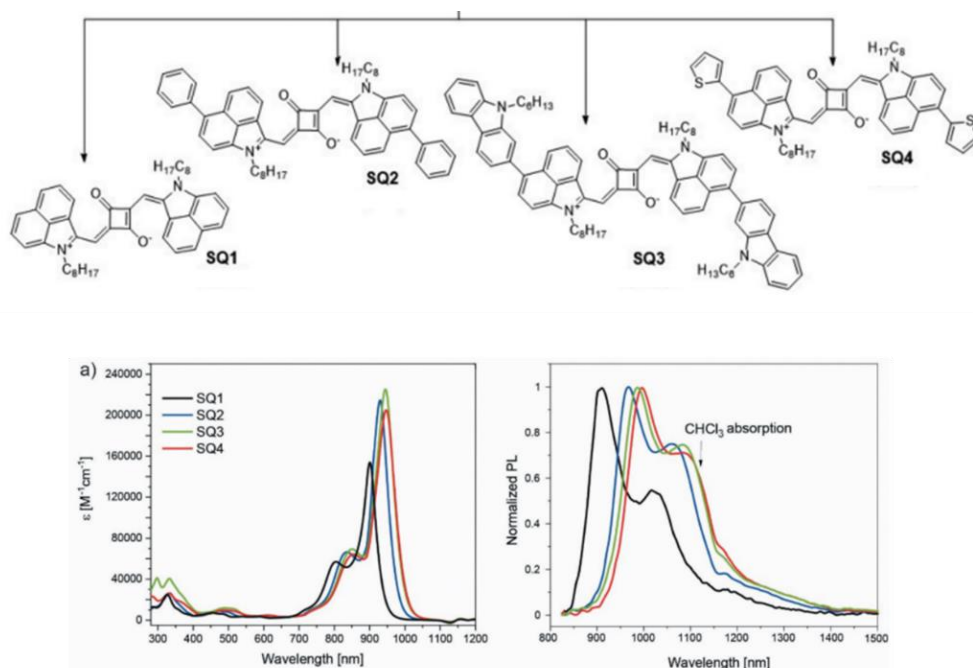


Figure 6: Structures of bis-benz(*cd*)indole-squaraine dyes and their absorbance and emission spectra¹³.

In addition to their interesting absorbance properties, the versatility of functionalizations that can be made to squaraine and frequently metal free synthetic routes make them highly attractive for chromophore design.

1.3.4 Quinoline

Like the other sub-structures mentioned, quinoline has been shown to have good acceptor characteristics, as a result of the electron deficient hetero nitrogen, and unusually intense absorbance and fluorescence for its size.

Quinolines have been used extensively for electron transporting layers in organic light emitting diodes and subsequently as a building block in a number of polymer and small molecule materials for OPVs¹⁴. In particular they have been used in dye sensitized solar cells, where the relative ease of adding anchoring groups to the 2-position of quinoline and physical bulk are attractive for adsorption onto electrodes. Quinolines with diphenyl amines in the 6-position (figure 7) which absorb across the visible range of light have been used to fabricate devices with have PCEs of 3.07%¹⁵. These DSSCs were, however, found to have decreased efficiency as a result of dye aggregation. A common problem with DSSC type OPVs, the addition of additives to reduce aggregation is a common practice, however this inherently also reduces the quantity of dye adsorbed onto the electrode surface, leading to tradeoffs in performance.

Another example of quinoline based optoelectronic materials is its addition to perylene diimides (PDIs) as executed by *Aivali et. al.* where they functionalized PDI according to the A-D-A design rules, in which phenyl and phenoxy spacers acted as the donors and quinolines as acceptors (figure 8). Upon evaluation of their optoelectronic properties, the group found that their library of mono and disubstituted dyes had LUMO levels between -3.8 and -4.2 eV. These values are comparable to fullerene-based materials such as PC₆₁BM that has a LUMO of about -4.0 eV, which as previously described have long been the standard

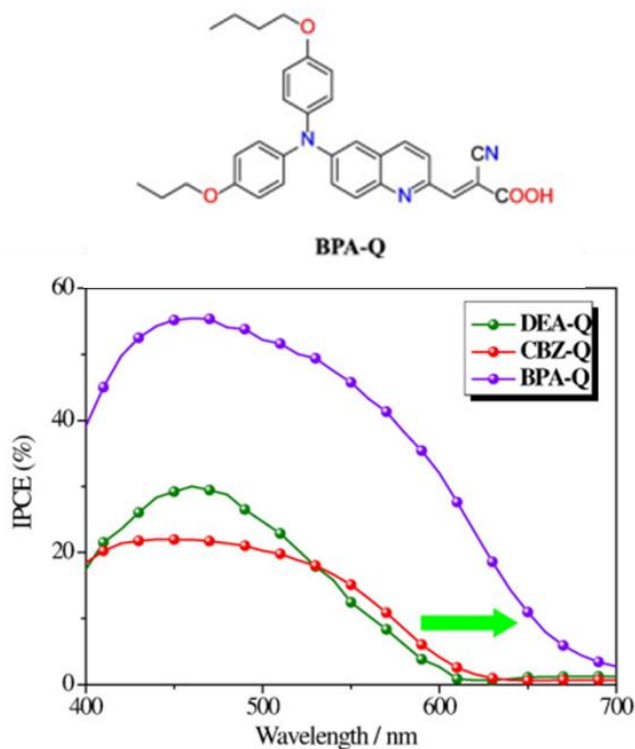


Figure 7: Structure of BPA-Q and measured Incident Photon Conversion Efficiency in a DSSC device with TiO₂ and platinum electrodes and iodine/iodide electrolyte¹⁵

for BHJ acceptors. These energy levels suggest that these quinoline and PDI molecules have the potential to be good acceptors in BHJ devices.

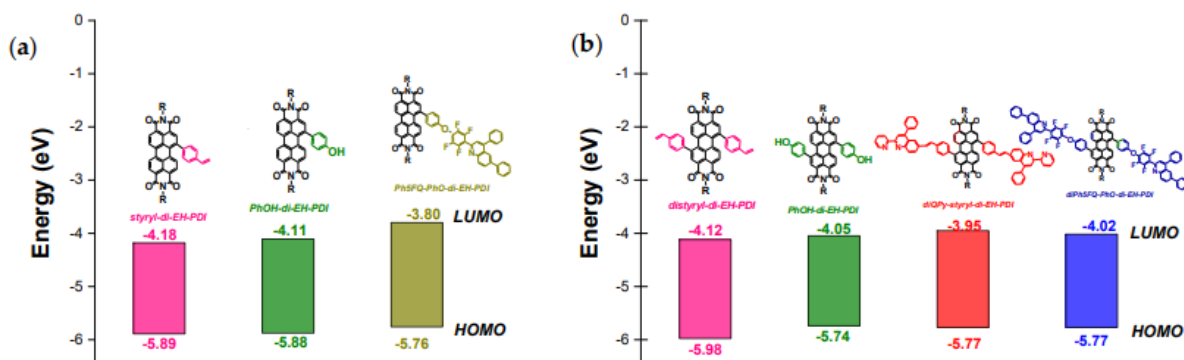


Figure 8: HOMO and LUMO values of quinoline substituted PDI dyes¹⁶

1.4 Effect of donating and withdrawing groups on energy levels

An important phenomenon to consider in designing and understanding of properties is the effects of electron donating and withdrawing groups. Even when the effects are not through conjugation and are purely inductive, they can have significant influence on the distribution of electron density and HOMO and LUMO levels of a given molecule. Inductively electron donating groups increase the electron density at the location of the LUMO and will destabilize it, making it more unfavorable to fill, therefore raising the energy. The other side of that same coin is that electron withdrawing groups adjacent to the HOMO will stabilize it, making favorable conditions for the electrons in the orbital, and lowering the energy. The orbitals not mentioned in each case are affected the same way for the same reasons, but typically to a lesser degree. The overall effect on the bandgaps is that electron donating groups increase the bandgap and withdrawing groups decrease it. These trends have been supported by both computational and experimental studies of chromophores^{17,18}.

The frontier orbitals of pyrene, for example, are calculated at -5.55 eV for the HOMO and -1.72 eV for the LUMO¹⁹. One study demonstrated the practical effects of the inductive influence of functional groups by substituting pyrenes with only electron donating groups (methoxy-, ketal-), only electron withdrawing groups (cyano-), or a combination of the two.

In comparison to the base molecule pyrene substituted with donor groups had elevated HOMO levels both experimentally and computationally (figure 9)²⁰. Pyrene derivative 7 had the strongest donating group and exhibited the greatest elevation of the HOMO, to -5.13 eV

experimentally and -4.63 eV experimentally. Conversely pyrene derivative 9 exhibits a computational HOMO of -6.69 eV, supporting a significantly stabilized energy level.

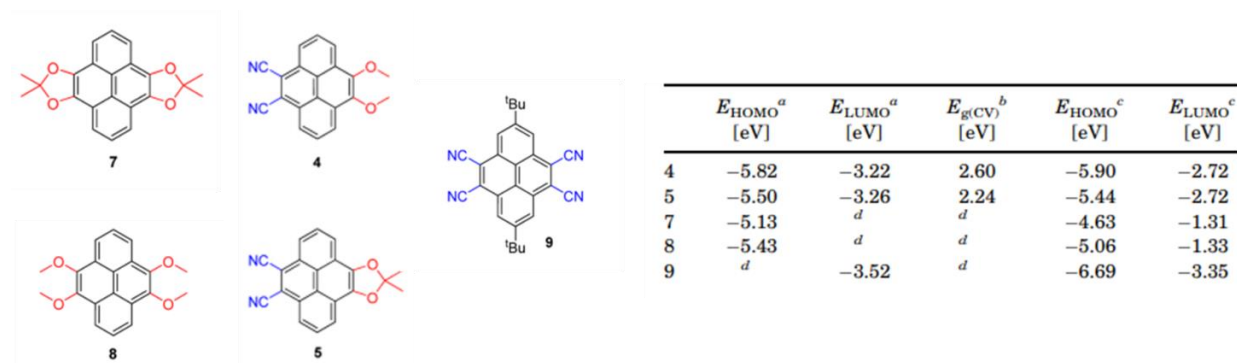


Figure 9: Structures of substituted pyrenes and the experimentally (^a) and computationally derived (^c) frontier energy levels ²⁰.

When the derivatives with both donor and acceptor groups exhibit less straightforward effects on the frontier orbitals but reduced bandgaps relative to unsubstituted, EDG only substituted, and EWG only substituted derivatives. This narrowing of the bandgap is desirable in pursuit of solar spectrum absorbing molecules.

1.5 Aggregation and its effects on photophysical properties

The excitation behavior of most dye molecules is not, in reality, as simple as direct intramolecular HOMO to LUMO transitions. There are also intermolecular factors at play. Kasha's model for aggregate excitation gives better insight to features in the observed spectra of photoactive molecules²¹. The theory states that aggregation has an effect on the absorbance of a molecule and that the orientation of the individual molecules relative to each other has an effect on whether the absorbance maxima are shifted to higher or lower energies (figure 9). Only excited states where the sum of the dipole vectors is not zero are allowed and will contribute to absorption, therefore when individual molecules are arranged in parallel, the energy of the aggregate is increased, leading to a blue shifted spectrum. Conversely if they are arranged in a "head to tail" manner the overall energy is lowered, resulting in a red shifted spectrum. In cases where asymmetrical molecules are arranged at an intermediate angle, or oblique orientation, band splitting may be observed, seen as two peaks rather than one.

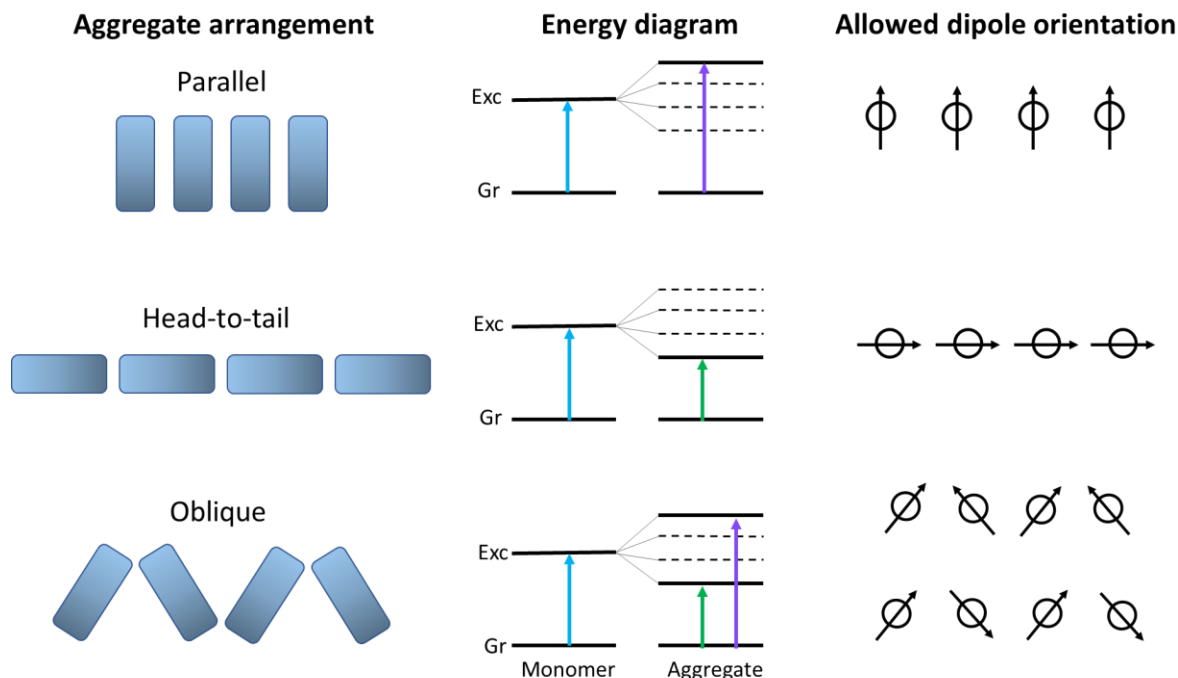


Figure 9: Illustrations of the three possible aggregate orientations, their energy level diagrams, and dipole orientations of the allowed transition states.

These aggregation effects are crucial to consider when characterizing photoactive molecules, as determination of energy gaps (to be discussed further in section 1.6), may be complicated by variation of peaks in spectra. The type of aggregation that occurs in solution may also have an effect the morphology of thin films, which affects device performance, performance via charge traps, diminished metal-organic interfacial contact resulting in poor charge collection, or even short circuits with the deposited electrode materials, so it is important to understand this phenomenon when working toward BHJ devices.

1.6 Graphene, pi-stacking, and its consequences in optoelectronics

Graphene is a sheet of carbon arranged in tessellated hexagons where every carbon atom (except those at the edges or imperfections) is sp² hybridized. This organic semiconductor therefore possesses nearly metallic properties, as its continuous conjugation across the surface is able to act as a conduction band as opposed to discrete orbitals, like those seen in most organic materials. The ability of electrons to flow quickly and freely along the surface of graphene has made it very attractive for applications in optoelectronics, but in order to realize these uses there are certain properties that must be tuned. One way to modify

graphene is through taking advantage of Van der Waals interactions that can occur between pi systems, referred to as pi-pi stacking. In pi-pi stacking the attractive forces between areas of higher and lower electron density allow a dye to "stick" to graphene and create a nanoensemble with properties encompassing both materials. The Fermi level of a material is the mid-point between the filled and unfilled energy levels, meaning it can be between the HOMO and LUMO (or between the Valence and Conduction bands in conductive materials). The fermi level of graphene is at -4.57 eV relative to vacuum²², and so when the HOMO and/or LUMO of the dye overlap with the favorably with the graphene, as defined by being above or below the fermi level, there can be electron transfer between the two²³. For example, if the paired molecule absorbs visible light, the graphene will act as an acceptor and promote exciton dissociation from the dye. The opposite is also true, although despite graphene's broad absorption within the visible spectrum, the percentage of incident photons it will actually absorb is low. Graphene's transparency is very high (about 97%) so it is much more likely to act as an acceptor than a donor.

Quenching of emission by fluorescent molecules can be seen when mixed with carbon nanomaterials such as fullerenes, carbon nanotubes and graphene. Provided that some conditions are met, such as energy level matching and proximity of the excited chromophore and the electron acceptor, photoluminescence quenching can occur through many mechanisms. This can be either by pi-pi stacking where, as described above, the graphene acts as an acceptor and takes the excited electron via electron transfer, or through other non-radiative relaxation interactions, such as heat transfer. The types of quenching which occur between Phthalocyanine and graphene, as well as graphene oxide, and single walled carbon nano tubes was investigated by *Zhang et al*²⁴. This particular study looked at the effects of all three, but the focus was on graphene as it had the strongest effect. The major absorbance of this phthalocyanine dye when on its own was at 675 nm, however after graphene was added to the solution it was found that it pi-pi stacked onto graphene, and a new, lower energy peak at 711 nm appeared. At the same time the emission of the dye at 685 nm was quenched completely.

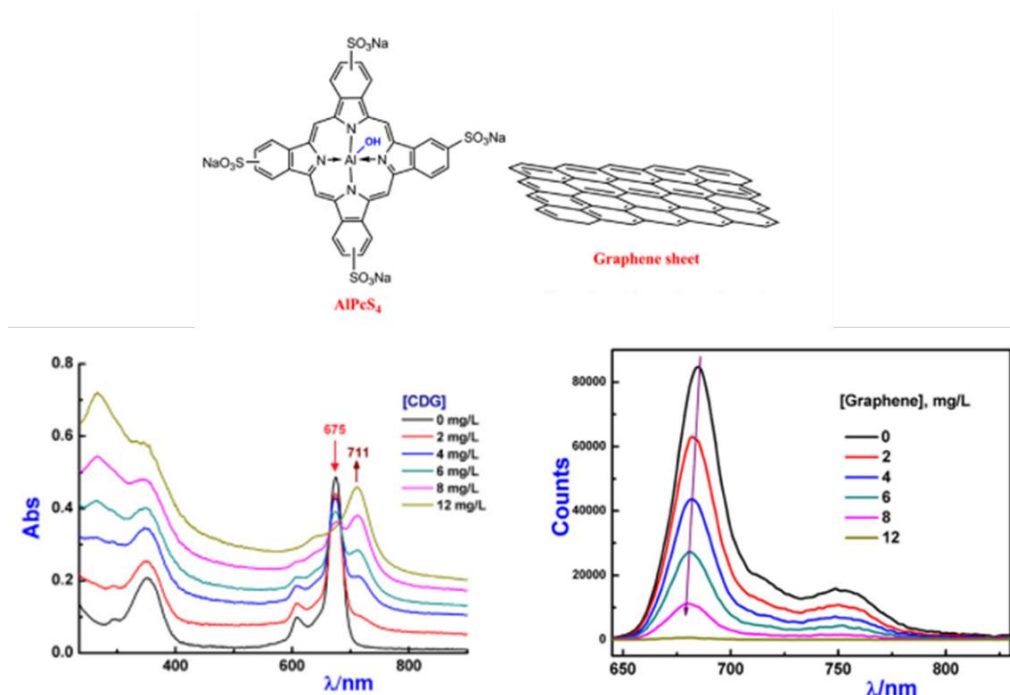


Figure 10: A) structure of phthalocyanine dye and graphene B) absorbance spectra of AlPcS₄ with additions of graphene C) fluorescence quenching of AlPcS₄ by graphene²⁴

Based on the conversion of the absorbance peak to the new red shifted peak, they attributed these changes largely to Static Quenching, or the formation of a new complexed species via coupling between graphene and the ground state of the dye (figure 10A). On the other hand, Dynamic Quenching can occur when the already excited species interacts with the graphene. Dynamic quenching as a class of interactions can result in emission by the acceptor or other methods of energy transfer, but the key factor is that the fluorescent species was excited and returns to the ground state without its major fluorescence. Graphene's low reduction potential relative to many other carbon nano materials makes it efficient at this type of quenching for many systems where it can act as an acceptor.

1.7 Photophysical characterization methods

As the energy levels of all components in BHJ device are so crucial to its function, the photophysical characteristics of a designed molecule must be characterized to understand its behavior and potential compatibility with a given system. The characterization of these properties involves determining the HOMO and LUMO values, investigating emission

behavior, and other electronic characteristics which need to be elucidated through a collection of methods.

1.7.1 UV-Visible spectroscopy

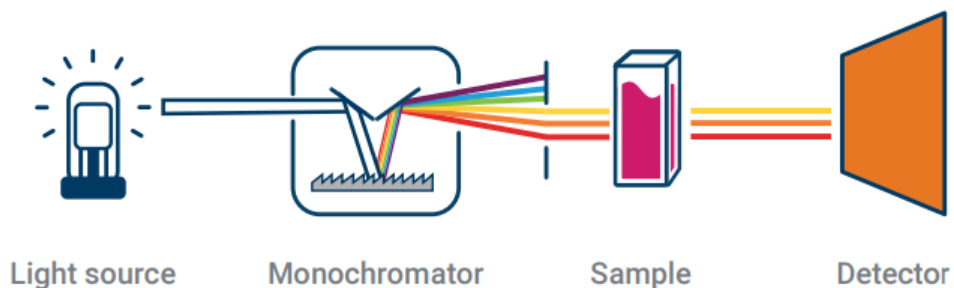
Ultraviolet-Visible Spectroscopy (UV-Vis) allows determination of the range of wavelengths in the ultraviolet and visible light range able to be absorbed by a molecule. A single beam instrument, as available for use in this project, utilizes a white light source and a UV light source, in this case a tungsten lamp and a deuterium lamp, and a monochromator to filter out a beam containing one wavelength of light at a time²⁵. The beam is shone through the sample of interest, and the intensity of light that reaches the detector on the other side is measured (scheme 1). In the single beam instrument, a baseline must be measured first. This is done by running a scan on the cuvette containing only the matrix in which the molecule of interest will be dissolved, in order to establish the intensity that would reach the detector if none is absorbed by the analyte. When the signal of the baseline is subtracted from the signal of the analyte containing measurement, the difference in intensity is attributed to the absorbance of the analyte. For example, if a beam of 450 nm light is sent through a sample, and the intensity at the detector is half of that of the uninterrupted beam, it is assumed that half of the 450 nm photons were absorbed by the molecules in the sample.

The relationship between the intensity at the detector and the absorbance is shown by equations 1 and 2.

(equation 1) $T = I/I_0$

(equation 2) $A = -\log T$

Transmittance (T) is the ratio between intensity from the sample measurement (I) divided by the intensity of the baseline (I_0). The negative log of T is then taken to convert to absorbance (A). With this relationship, if I is equal to I_0 it indicates that all of the given wavelength passed through the sample and A is zero, whereas if T is equal 0.1, indicating that only 10% the given wavelength passed through the sample, A is one. By convention, absorbances greater than one are not considered valid.



Scheme 1: Basic schematic of a single beam UV-Vis instrument²⁵

When collecting an absorbance spectrum, the monochromator transitions through a range of wavelengths in the determined window of interest, and measures the absorbance of the sample at each. The resulting spectrum is a curve, or collection of curves, that shows what wavelengths the analyte absorbed. Because of light's constant speed, wavelength is easily translated into a corresponding energy. When looking at a UV-Vis spectrum, the lowest energy transition of the molecule will be seen as the onset of the peak at the longest wavelength. The energy of this absorption corresponds to the HOMO to LUMO transition of the molecule.

1.7.2 Photoluminescence spectroscopy

Photoluminescence spectroscopy operates on many of the same principles as UV-Vis, but rather than looking at the excitement of a molecule, it allows investigation of the relaxation behaviors. With respect to instrumentation, the primary difference is that the detector must be at 90° relative to the light source to avoid detection of photons that are not those emitted by the analyte, and that there is no need to acquire a baseline, as the signal is counts of photons as opposed to a difference in current generated.

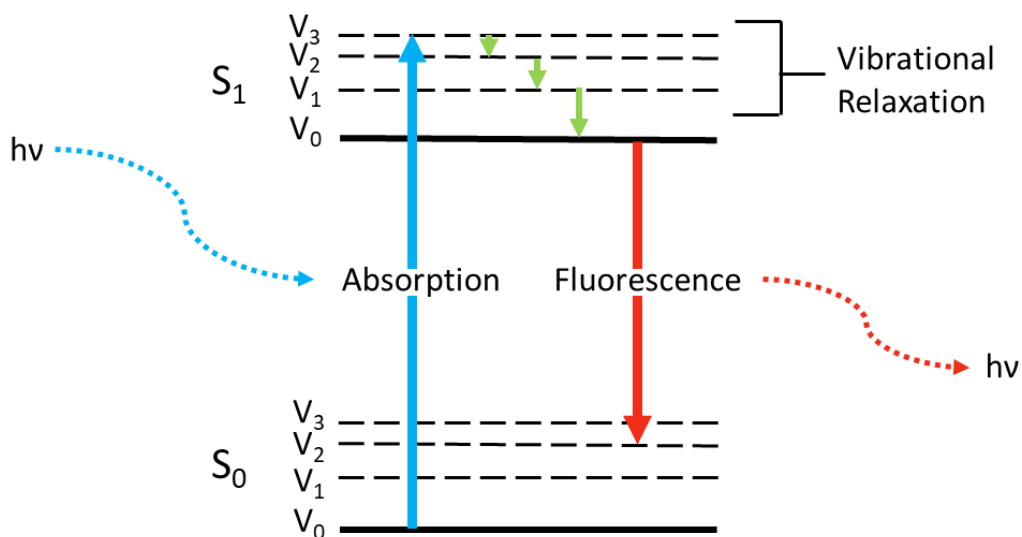


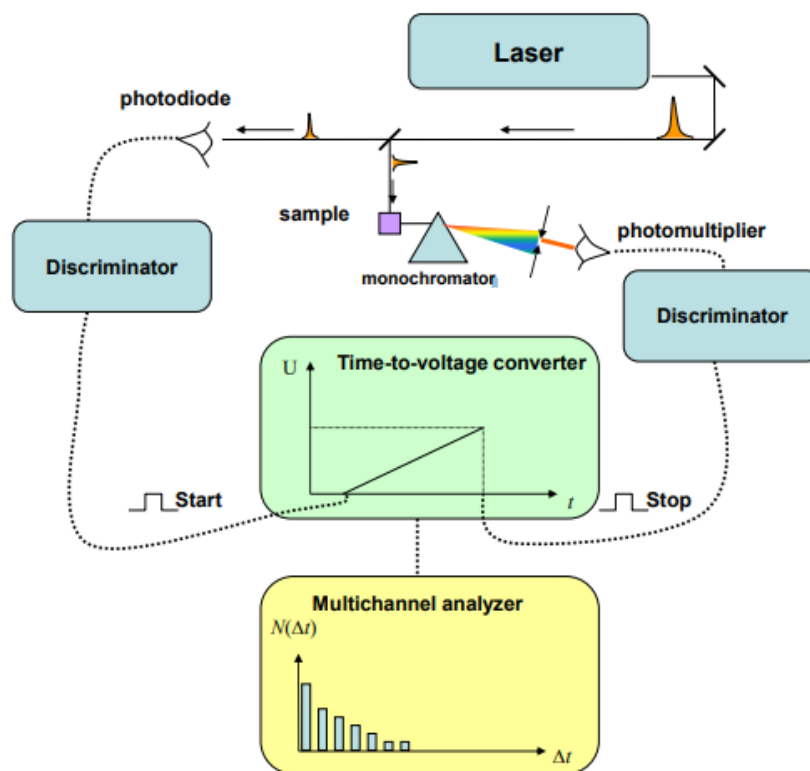
Figure 11: Jablonski diagram illustrating absorption and vibrational relaxation prior to emission

When an electron has been moved from its ground state (S_0) to an excited state (S_1), it is in an unstable form. The electron will find routes to release its excess energy so that it can return to its more stable ground state. One of these routes is through the emission of a photon, which is referred to as fluorescence. The wavelength of light emitted by a molecule is normally near to that of the major absorbance, however it will be red shifted. This occurs as a result of an additional set of energy levels present in a molecule called vibrational levels. These increments are much smaller than that of the major energy levels, and transitions between them are non-radiative. When an electron is excited, it can “over-shoot” and land in a higher vibrational level, from which it will relax before undergoing fluorescence. Fluorescence may also not return to V_0 of the ground state, resulting in the emission of photons with even lower energy than that of the difference between V_0 of S_0 and V_0 of S_1 . The details of the selection rules for vibrational transitions are not required for this work, but the overarching concept of the red shift that occurs between absorption and emission, called the Stokes Shift, will be referenced.

If fluorescence is not strong in a chromophore, this indicates that its major routes of relaxation occur by other methods. As touched on in section 1.5, these fluorescence quenching mechanisms can include heat transfer, collisions, and electron transfer to other species in a sample.

1.7.3 Time Correlated Single Photon Counting

Time Correlated Single Photon Counting utilizes an ultra-fast pulsed laser to excite a sample at a single wavelength and then measure the time it takes after the pulse for the instrument to receive emission photons. The instrument (scheme 2) fires a pulse from the laser which is then split so that it is sent to both the sample and a photo diode. When the signal is received at the photo diode it indicates the "start" time, or zero, to the computer. Once the sample has been excited and then relaxed, its emission is filtered with a monochromator and detected by a photomultiplier tube. When this signal is received it indicates a "stop" time. The computer sorts this signal to a bin based on the length of time between the "start" and "stop" signal and it is added to a histogram.



Scheme 2: Schematic illustrating the simplified construction and principles of the instrument for TCSPC ²⁶

Analysis of the data is done by the computer fitting an equation to the histogram. The fit follows the format in equation 3.

$$\text{(equation 3) } R(t) = B_1 * e^{(-t/\tau_1)} + B_2 * e^{(-t/\tau_2)} + \dots B_n * e^{(-t/\tau_n)}$$

The fitting function ($R(t)$) can contain as many terms as the number of processes which contribute to the type of emission measured, but most often there are between one and four. The τ -values in the exponential correspond to the lifetime of a given relaxation process. The software will also provide the relative population of each term as a percentage, allowing determination of how much each process contributes to the overall observed emission.

1.7.4 Cyclic Voltammetry for determination of HOMO and LUMO levels

Cyclic Voltammetry (CV) is a method which can be used to measure the redox behavior of a molecule of interest²⁷. There are usually three electrodes used in the system: the working electrode (WE), counter electrode (CE), and reference electrode (RE). The WE applies the potential to the system and is where the analyte is reduced or oxidized. The CE completes the circuit of the potentiostat and allows current to flow. The RE contains a known redox pair that is very sensitive to potential, though internal references can also be used. In essence the three-electrode system, operates in "pairs" where the WE/CE pair are responsible for the current measurements (typically the Y-axis in a voltammogram) and the WE/RE pair is what provides the values for the voltage (typically X-axis). The potential measured by the potentiostat is not an absolute value and depends on many conditions of the system, so the reference is a well-defined reaction that the measured result can be adjusted against. The potential of the system is increased until the energy at the WE is higher than that of the LUMO of the analyte, an electron transfer will occur to fill the empty orbital. When most of the reduction is occurring, the current in the system is at a maximum, corresponding to point B in figure 12. After this point the concentration of reduced analyte at the WE begins to buildup faster than it can diffuse away, it begins to insulate the electrode, and current is reduced (point C in figure 12). The potential is then scanned in the reverse direction, and the inverse current increases as the analyte gives up the excess electron, allowing determination of the oxidation potential.

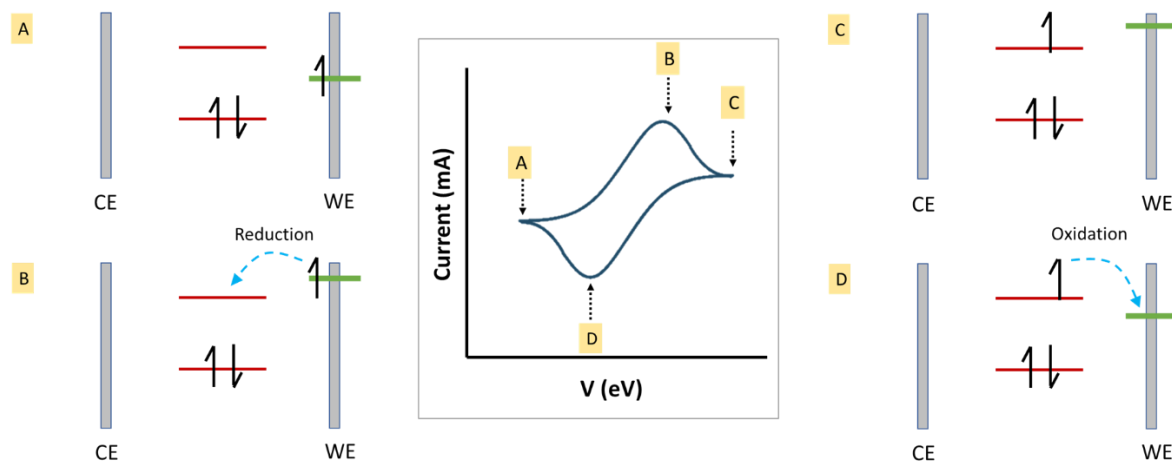


Figure 12: Example of a hypothetical CV scan with energy level diagrams corresponding to key points A) initial condition B) reduction C) saturation of reduced species D) oxidation

When using CV to characterize organic systems, it is standard to use ferrocene as an internal reference, as it has a known HOMO at -5.1 eV relative to vacuum²⁸. Therefore the HOMO and LUMO of the analyte can be calculated as follows:

$$\text{(equation 4) } E_{\text{HOMO}} = -e (E_{\text{ox}}^{\text{onset}} + 5.1)$$

$$\text{(equation 5) } E_{\text{LUMO}} = -e (E_{\text{red}}^{\text{onset}} + 5.1)$$

The difference between E_{HOMO} and E_{LUMO} is defined as the energy gap, E_g , and when converted to wavelength should match with the onset of absorbance seen in the UV-Vis measurements.

1.8 Aim of the thesis

With the goal of creating new materials for OPV applications, target molecules were designed based on the design rules and moieties discussed: NDIs, squaraines, and quinolines. Efforts to synthesize a new NDI based acceptor were begun and will be outlined in the discussion. Upon encountering roadblocks in the synthetic pathways attempted, however, a transition was made to work with squaraine based dyes. While the synthetic pathway of these dyes were originally achieved by previous master's students, significant improvements to methodology were made and photophysical characterization was completed to further understand the behavior of the chromophores.

2 Results and Discussion

2.1 Naphthalene diimide based acceptor

Based on the A-D-A design strategy described in section 1.2 and the acceptor type moieties described in section 1.3, a target acceptor for BHJ applications was designed with naphthalene diimide as the central acceptor unit. Adding it to a carbazole introduces the donor unit, which would be further substituted with quinoline as another acceptor. This extended alternation of acceptor and donor units hoped to maximize the push-pull effect. The carbazole moiety (in addition to NDI) can be decorated with alkyl chains, which play an important role in both solubility and other properties in the active layer. Although alkyl chains have very little, if any, effect on the solution absorbance properties of chromophores, comparison of the thin films can exhibit significant variations in the observed absorbance as a result of the orientations and crystallinity allowed by different varieties of alkyl chains²⁹. The relationship between chain length and morphological character of a film, such as roughness, is also not always linear or easily predictable³⁰, so the ability to create a library of varied groups is an advantage. These morphological differences ultimately also affect the hole and electron mobilities of the semiconductive materials³¹, which is as crucial to device efficiencies as the compatibility of energy levels. The overall structure of the target molecule is shown in figure 13.

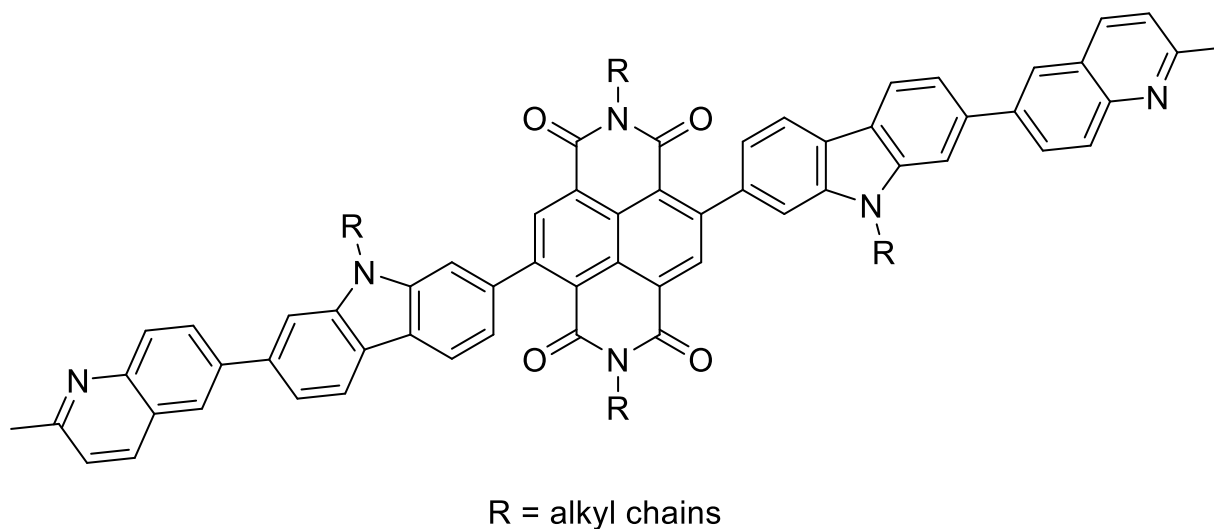


Figure 13: Structure of target acceptor molecule

2.1.1 Process for bromination and imidation of naphthalene dianhydride

With naphthalene diimide derivatives selected as an acceptor core, it needed to be prepared for functionalization. Suzuki reactions are common and desirable for aromatic couplings, as they have relatively mild reaction conditions, tolerant to water and often to air, and require one brominated and one boronic acid functionalized reagent. As boronic acid derivatives of many donor moieties are available to purchase, the NDI core needed to be the brominated component. There were two initial routes explored to achieving the brominated NDI molecules: imidation followed by bromination, or vice versa (figure 14).

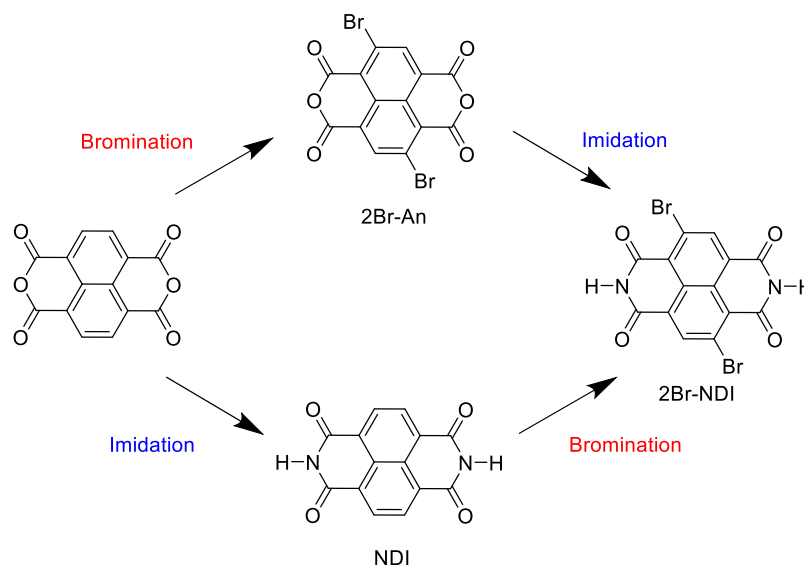


Figure 14: Possible synthetic routes for achieving brominated NDI

The bromination of naphthalene dianhydride is known from literature to be difficult by some classical brominating reagents like elemental bromide or N-bromosuccinimide³². 1,3-Dibromo-5,5-dimethylhydantoin (DBH) was selected as the brominating agent, as it has been used by other researchers with success³³. The first route pursued was bromination followed by imidation. While dibromination was successful in the first step, yielding 70% of 2,6-dibromo-1,4,5,8-naphthalenetetracarboxylic acid dianhydride (2Br-An), the subsequent imidation step executed by reacting with ammonium hydroxide³⁴, only yielded 30% of 2,6-dibromonaphthalene-1,4,5,8-tetracarboxydiimide (2Br-NDI). This overall yield of 21% across two steps was undesirable, so the alternate order was attempted. Reversing the order of the reactions, so that imidation was done first resulted in 60% yield of NDI, then a 90% yield of 2Br-NDI, for a 55% yield over the two steps. This is a significant improvement over the first method described. This molecule has been synthesized before, however the

method was developed as a combination of several procedures found in the literature. The identity of the product was confirmed with ^1H NMR (figure 15) and Even Electron Mass Spectrometry (SI 2.1). It is noted that the integration of the peak associated with the imide proton in 2Br-NDI is lower than expected, but the ease of exchange of this proton with the solvent due to the nitrogen's participation in conjugation with adjacent carbonyls can stabilize the cation and cause this effect. Additionally, the use of MS to further support the formation of the desired product showed a peak at 422.8620, where the theoretical exact mass is 422.8616, giving strong indication for the presence of the expected product.

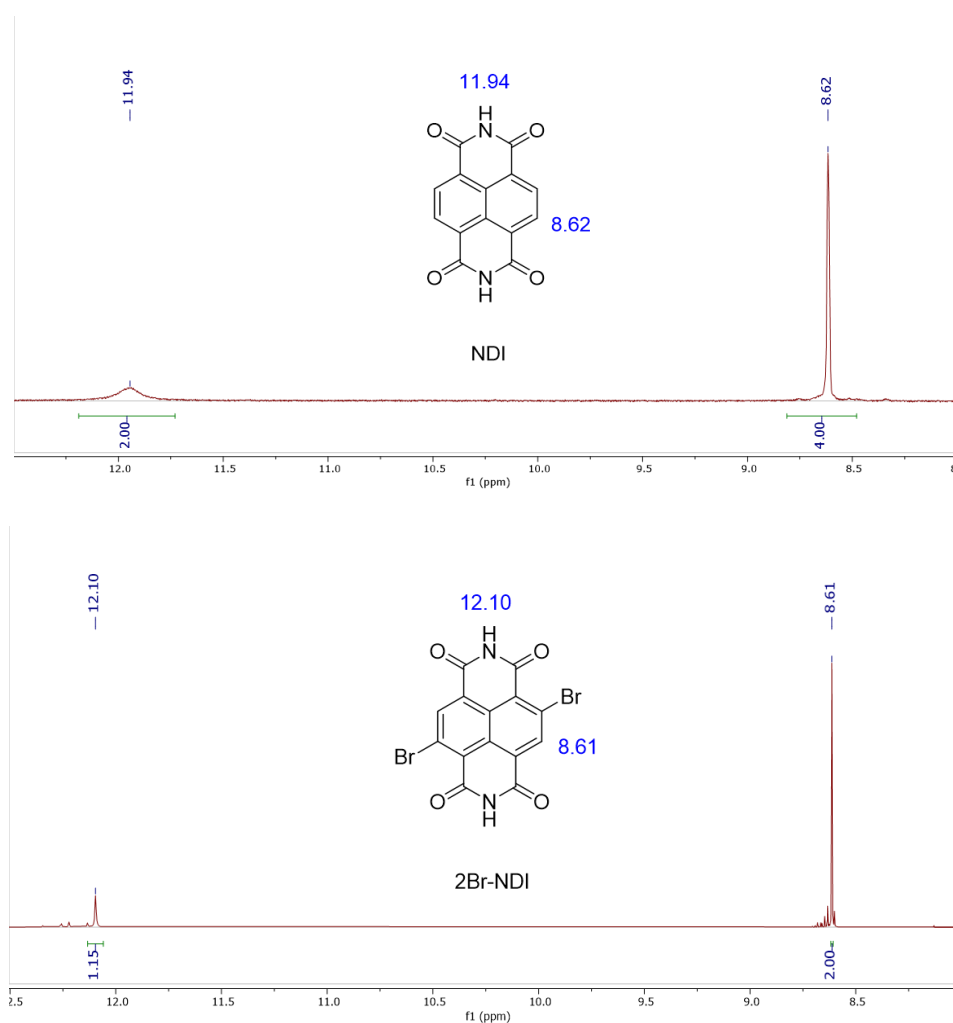
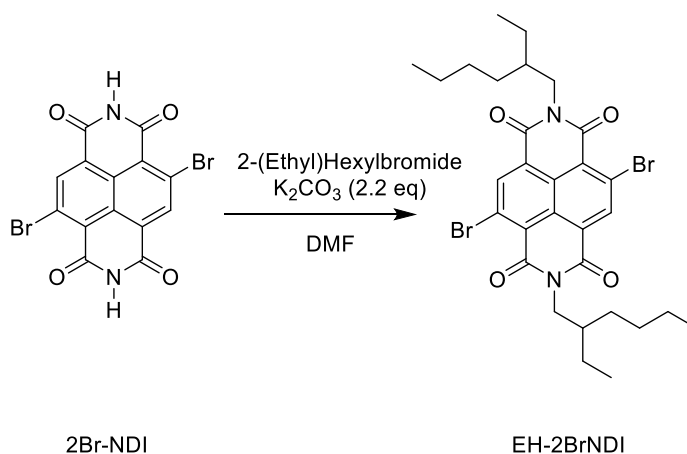


Figure 15: ^1H NMR (600 MHz, d_6 -DMSO) (zoomed to show peaks of interest) of NDI (upper) and 2Br-NDI (lower) with shift assignments, full spectra are shown in SI 1.1 and SI 1.2

While 2Br-NDI was synthesized, it is a molecule which is insoluble in most organic solvents, as well as water. It has poor to moderate solubility in polar-aprotic, high boiling solvents such as dimethyl sulfoxide and dimethyl formamide. For these reasons the next step was to alkylate at the diimide nitrogens in order to promote solubility. The first alkyl chain selected was 2-ethyl-hexyl, as the longer branched chain would be helpful to combat aggregation in the final molecules. Initial synthetic attempts were based on literature procedures of other alkylations of naphthalene diimide derivatives where yields greater than 70% were reported and DMF was used as the solvent³⁵, as this was necessary for solubility of the 2Br-NDI. The main parameters adjusted were time, temperature, and heating method. Increased yields were found after the reaction was heated to 85°C as opposed to 50°C. The best reaction time was 6.5 hours which was determined by monitoring the reaction with TLC (30:70 Petroleum Ether:CHCl₃) until excessive formation of spots not associated with the product was observed. Attempts to run the reaction longer resulted in degradation to a dark purple solution with no product visible in ¹H NMR. Despite the variety of conditions that were attempted (table 1), yields greater than 19% were not achieved.



Scheme 3: General reaction scheme for the synthesis of EH-2BrNDI

Table 1: Iterations of alkylation methods attempted for synthesis of EH2Br-NDI

Trial	Temperature (°C)	Time (hr)	Heating method	Yield
1	50	8	Bath	Trace
2	50	16	Bath	11%
3	50	24	Bath	None
4	50	0.66	Microwave	Trace
5	85	6.5	Bath	19%
6	85	18	Bath	None
7	85	0.66	Microwave	6.5%
8	85	3	Microwave	15%

* all with K_2CO_3 as the base in dry DMF

This work reports a new method of product isolation of EH-2BrNDI, as the product was found to be soluble in chloroform but not acetone, which made a simplified purification process possible relative to literature methods which described the use of column chromatography. After the standard organic workup, the product was agitated in acetone by sonication for 30 seconds, then centrifuged with acetone for five minutes at 4,000 rpm, then the supernatant removed. This process was repeated twice. The supernatant contained the red/pink biproduct that developed from the reaction and the yellow solid of the pure product remained. The (N, N')-(β -ethyl-hexyl)-2,6-dibromonaphthalene-1,4,5,8-tetracarboxydiimide (EH-2BrNDI) product that was isolated was fully characterized with 1H NMR, ^{13}C NMR, and two dimensional NMR methods (SI 1.4).

Table 2: ^1H and ^{13}C NMR shifts of EH-2BrNDI

Position	^1H Shift (multiplicity, quantity)	^{13}C Shift
1	---	161.26
2	---	125.43
3	---	127.91
4	---	128.52
5	9.0 (s, 1H)	139.32
6	---	124.23
7	---	161.19
8	4.15 (dq, 2H)	45.29
9	1.94 (sept, 1H)	37.91
10	1.34-1.42 (m, 2H)	30.76
11	1.28-1.32 (m, 2H)	28.67
12	1.28-1.32 (m, 2H)	23.21
13	0.88 (t, 3H)	14.22
14	1.34-1.42 (m, 2H)	24.11
15	0.94 (t, 3H)	10.71

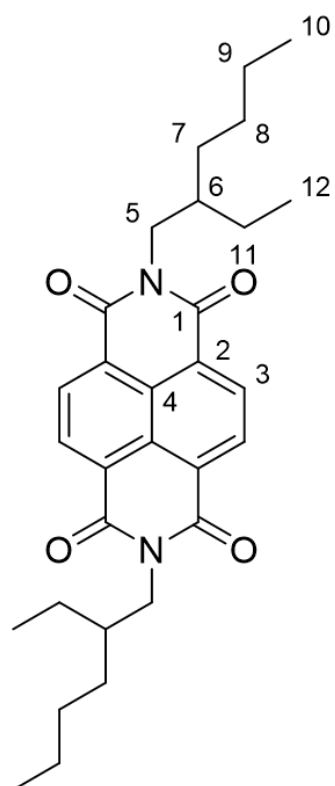
Because the previous products, NDI and 2Br-NDI have such low solubility, carbon spectra were difficult to obtain, and two dimensional spectra were not possible, therefore the two dimensional spectra obtained of the alkylated EtHex-2BrNDI helped to confirm the identity of these previous products. Most importantly it confirms the dibromination on the naphthalene core, as a greater or lesser degree of bromination would have resulted in a different number of inequivalent quaternary carbons and an incorrect ratio of the aromatic proton to the alkyl protons. The obtained spectra have the expected seven inequivalent aromatic carbon environments, with 6 of them quaternary. If products with different degrees of bromination were included in the 2Br-NDI used in the reaction they were not visible in NMR, however it is not expected that they would have been separated from EH-2BrNDI in the applied purification process, and thus were very unlikely to be present.

One attempt was made based on the best method (number 5 in table 1) but with iodo-propane in place of 2-(ethyl)-hexyl bromide. This reagent has less steric bulk and a better leaving group, however the yield was still only approximately 25% crude product, and contained a 4:1 ratio of di alkylated to mono alkylated product. The tradeoff for this moderate increase in alkylation yield was that the product exhibited low solubility in chloroform, meaning that ultimately the propane would not be as helpful in combating

aggregation as longer or branched alkyl groups. This led to the need to redesign the synthetic pathway to be able to incorporate these longer alkyl chains.

Initially the decision to imidate and alkylate in two different steps was based on the hope of being able to easily vary alkyl groups in a library of final acceptors, however as that had proved difficult, it was decided to add these functionalities in one reaction step with an alkylamine. Because it had previously been shown that bromination occurred in the highest yield after imidation, this order was maintained. Based on a similar methodology for the synthesis of perylene diimides, 2-(Ethyl)-hexylamine was reacted with naphthalene dianhydride in toluene at 110°C overnight³⁶, which similarly to literature, resulted in 25% yield of alkylated NDI (table 3).

Table 3: ¹H and ¹³C NMR shifts of EH-NDI



Position	¹ H Shift (multiplicity, quantity)	¹³ C Shift
1	---	163.37
2	---	126,73
3	8.75 (s, 2H)	131.16
4	---	126.88
5	4.13 (dq, 2H)	44.74
6	1.93 (sept, 1H)	38.08
7	1.35-1.41 (m, 2H)	30.83
8	1.26-1.31 (m, 2H)	28.77
9	1.26-1.33 (m, 2H)	23.18
10	0.88 (t, 3H)	14.21
11	1.35-1.41 (m, 2H)	24.21
12	0.93 (t, 3H)	10.74

Unfortunately, the subsequent bromination using the previously successful procedure did not give any product, only returning the starting materials as confirmed with ¹H NMR.

2.1.2 Suzuki couplings of brominated naphthalene diimide

At this point since all methods attempted for alkylation had proved so poor, it was decided to couple 2Br-NDI with a donor before alkylation. The target molecule contained carbazole,

so the first Suzuki coupling was done with carbazole-2-boro-pinacol ester. Because of the insolubility of 2Br-NDI, the first synthetic procedures were designed to be all-organic Suzuki couplings. For these rather than the salt of a base in aqueous solution, triethyl amine was used, as TEA is miscible in organic solvents. The reaction was stirred at ambient temperature overnight, using distilled DMF, but no product was formed, and starting materials were the only peaks visible in NMR. Due to the cost of carbazole-2-boro-pinacol ester, further optimization of the procedure (table 3) was executed with pyrene-1-boronic acid instead which is another donor group which could be of interest for characterization later.

Table 4: Suzuki reaction conditions for coupling 2Br-NDI with donor groups

Trial	Donor	Solvent system	Base	Catalyst	Temp	Yield
1	Carbazole	DMF	TEA	Pd(PPh) ₄	ambient	None
2	Pyrene	DMF	TEA	Pd(PPh) ₄	ambient	none
3	Pyrene	DMF	TEA	Pd(PPh) ₄	80°C	none
4	Pyrene	EtOH:Toluene:H ₂ O (0.18 : 1 : 0.5)	K ₂ CO ₃	Pd(PPh) ₄	70°C	none
5	Pyrene	H ₂ O:Dioxane (2 : 1.7)	K ₂ CO ₃	Pd(OAc) ₂ :SPhos (1 : 2.1)	37°C	Possible trace

The all-organic coupling attempts only returned the starting materials after reacting overnight. The conditions of trial 4 were adapted from published Suzuki couplings used for brominated perylene diimides (PDIs)³⁷, where a mixture of ethanol, toluene, and water was used, however there was still very poor solubility of the 2Br-NDI and the reaction mixture remained nearly solid and yielded no product. A final attempt was designed with H₂O, Dioxane, and SPhos. Dioxane is a common solvent used in Suzuki couplings and is used in other syntheses executed by the lab group and SPhos is one of the latest generation of catalysts for Suzuki couplings. It has been used in particular for couplings of boronic acids of donors and brominated electron deficient heterocycles³⁸. Following this reaction, new peaks not attributed to the starting materials were found in the ¹H NMR spectrum, however TLC revealed that many side products had been generated, and column chromatography had poor separation, so products were not isolated such that they could be identified.

2.1.3 Next steps for NDI based small molecule semiconductors

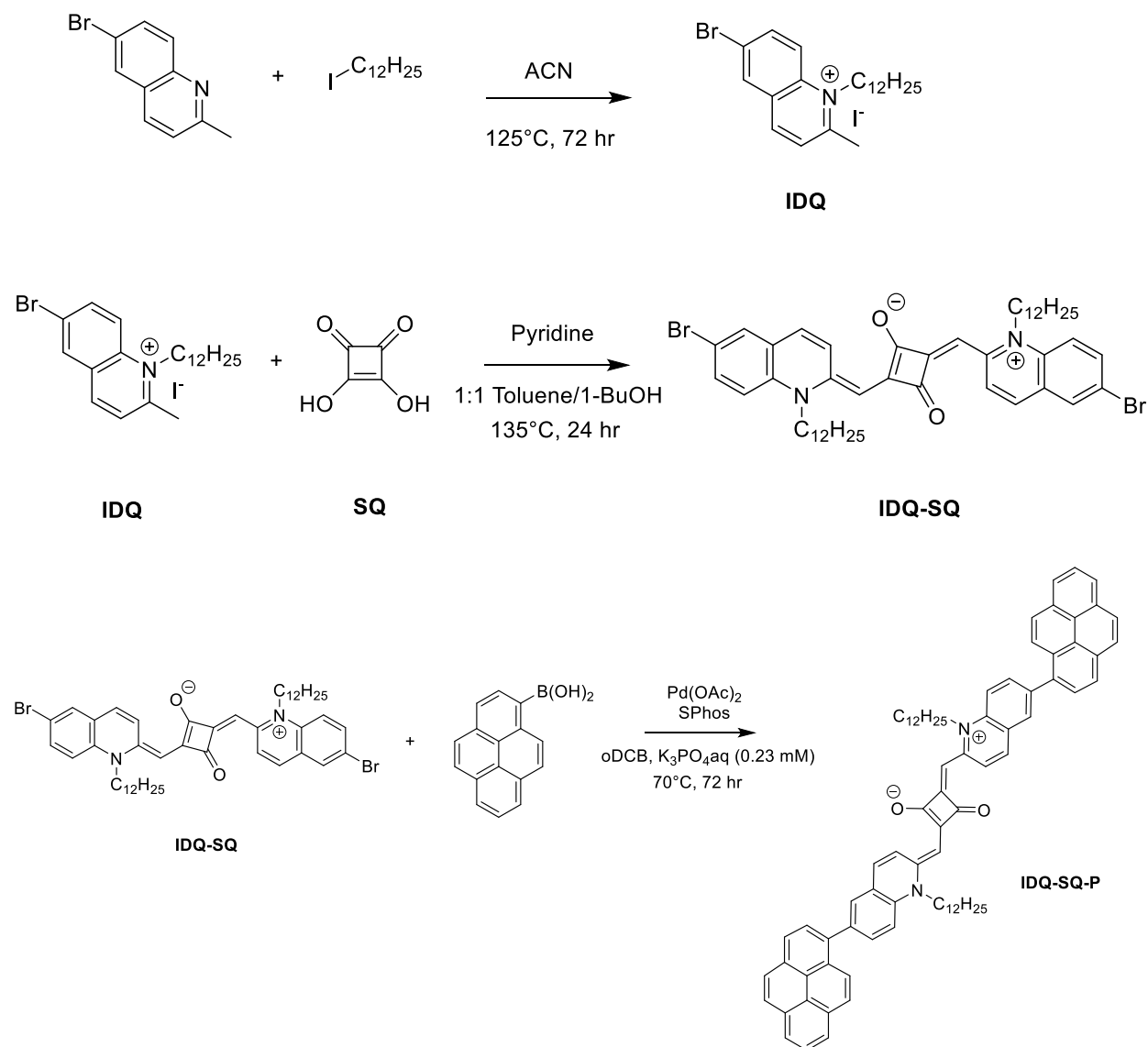
By this point it was determined that the synthesis of the target NDI acceptors was not going to result in product yields within a reasonable amount of time such that meaningful photophysical data could be attained in the course of this master's project. For these reasons a transition was made to focus on the synthesis, scaling up of reactions, and characterization of other semiconductor molecules that were originally synthesized by previous students. While difficult to work with, groundwork has been laid for future work on the synthesis of NDI based semiconductors. It is the belief of this researcher that they should continue to be developed, and so here some suggestions for future work will be described.

Future pursuit of these molecules should still focus on establishing an alkylated NDI prior to Suzuki coupling. Without these side chains, the solubility issues prevent access of the catalyst to the reactants and do not favor good yields. Other publications have reported bromination of the naphthalene dianhydride first then reacting with an alkyl amine to reach a desired alk-2BrNDI. Although literature procedures with this route also consistently report low yields across both steps, acid catalyzed imidation using acetic acid and 2-Ethylhexylamine has been published with up to 55% yield³⁹. In theory, with the established method of synthesizing 2Br-An with DBH, which had a 70% yield, and the aforementioned procedure, an approximately 40% yield of EH-2BrNDI could be achieved over two steps. Once an alk-2BrNDI has been synthesized, there are many reported Suzuki couplings without the need for unusual conditions like the water free Suzuki couplings attempted in this work. EH-2BrNDI has been synthesized with Pd(PPh₃)₄, THF, aqueous base, and mild heating^{40,41}. It has also been shown that bromination of aromatic groups after they have been coupled to alk-2BrNDI is possible, such as with a thiophene substituted NDI, so the addition of further functionalization to extend conjugation should be achievable⁴⁰.

2.2 Synthesis and photophysical characterization of squaraine-quinoline based dyes

A chromophore of interest for BHJ applications based on a central squaraine moiety was explored. These small molecules were coupled with electron deficient quinaldinium salts to generate A- π -A structures which have been very efficient at absorbing visible light radiation, exhibiting UV-Vis absorbances over 700 nm. The brominated end positions also allow for further substitution to further tune their properties. The core molecule, 2,4-(((N)-dodecyl-6-pyrenyl)-bromo)-methyl-3-oxocyclobutenolate (IDQ-SQ), was synthesized, as well as the main D-A- π -A-D structured target, 2,4-(((N)-dodecyl-6-pyrenyl)-quinolinium)-methyl-3-oxocyclobutenolate (IDQ-SQ-P). While these have been synthesized previously⁴², attention was given to optimizing the methods to allow for the synthesis of gram scale quantities. Following synthesis the main focus was placed on photophysical characterization in order to elucidate phenomena which take place in such D-A- π -A-D systems.

2.2.1 Optimization of synthetic procedures and purification methods



Scheme 4: Total synthetic pathway to IDQ-SQ and IDQ-SQ-P

The alkylation of the quinolinium salts was executed in acetonitrile in a sealed vial at 130°C for 72 hours. Previous work up necessitated column chromatography with a methanol:chloroform system for the eluent, however a simplified purification process was done using ethyl acetate and centrifugation. The starting quinoline is soluble in ethyl acetate while the alkylated salt product remains precipitated, allowing for easy separation by removal of the supernatant. Further improvement was made with respect to the atom economy of the reaction, as the ratio of quinoline to iododecane was reduced from 1:4 to

1:1.5. Finally the scale of the reaction was increased to give over 3g of product reproducibly at yields of 40-50%. The increase in yield may largely be owed to the improved purification method.

Coupling the quinoline (IDQ) with squaric acid had previously resulted in high yields (from 60-95%), however purification of the product remained difficult. Despite the use of flash chromatography, the separation of the base used in the reaction, be it pyridine or quinoline, was not consistently achievable. This work reports nearly gram scale isolation of pure IDQ-SQ by precipitation, where solvents were removed from the crude reaction mixture before the addition of MeOH and stirring overnight. Following filtration and drying under reduced pressure, 0.9 g (70% yield) of pure product was collected, and confirmed with NMR (SI 1.7).

The Suzuki coupling of IDQ-SQ with Pyrene was executed without further optimization.

2.2.2 Absorbance data and aggregation behavior of IDQ

The characteristics of IDQ, IDQ-SQ, and IDQ-SQ-P have had some brief study, and preliminary BHJ device fabrication was done with IDQ-SQ-P as a donor and PC₆₁BM, a fullerene adduct, as the acceptor. Poor device characteristics were recorded, with a Fill Factor of only 28%, which was attributed to aggregation and morphological incompatibilities between donor and acceptor. This study focuses on more in depth photophysical characterization in order to understand the results and potentially identify better systems.

To understand the influences on the aggregation behavior of the larger molecules, focus was first placed on the quinoline moiety. As mentioned in section 1.3.4, quinoline containing dyes characterized by other researchers have also been prone to aggregation, so the behavior of Iodo Dodecyl Quinoline (IDQ) itself was characterized. The emission spectrum of IDQ when excited at its absorbance maximum (300 nm) shows a marked complexity relative to its structure (figure 16). To further understand where each of the peaks originate, a series of spectra were taken while the concentration was incrementally increased to see how the formation of aggregates influenced the emission of IDQ.

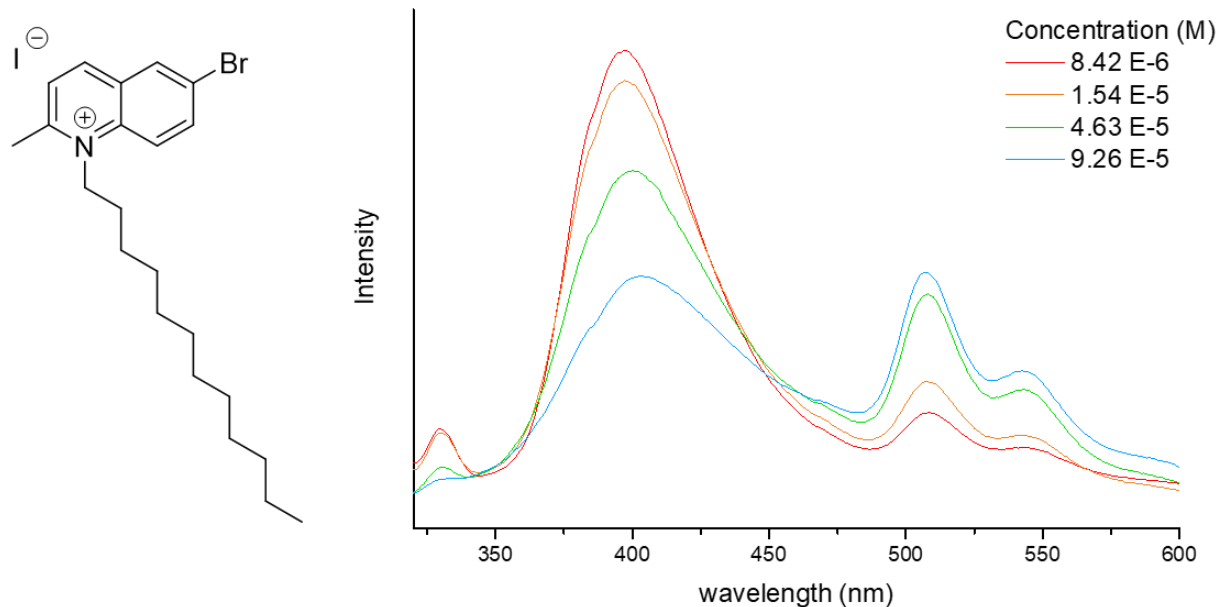


Figure 16: Structure and emission spectra (excited at 300 nm) of IDQ

As seen in the absorbance spectra (figure 17A), as the concentration of IDQ increases, a shoulder begins to appear around 360 nm. When this shoulder is probed by excitation at 350 nm in order to avoid excitation at the major absorbance, the emission spectrum changes to appear as shown in figure 17B. It is worth noting that the intensity of emission at 505 nm increases at a greater rate relative to concentration than the main emission at 394 nm. In the highest concentration solutions there is also a second emission component which can be seen at 545 nm.

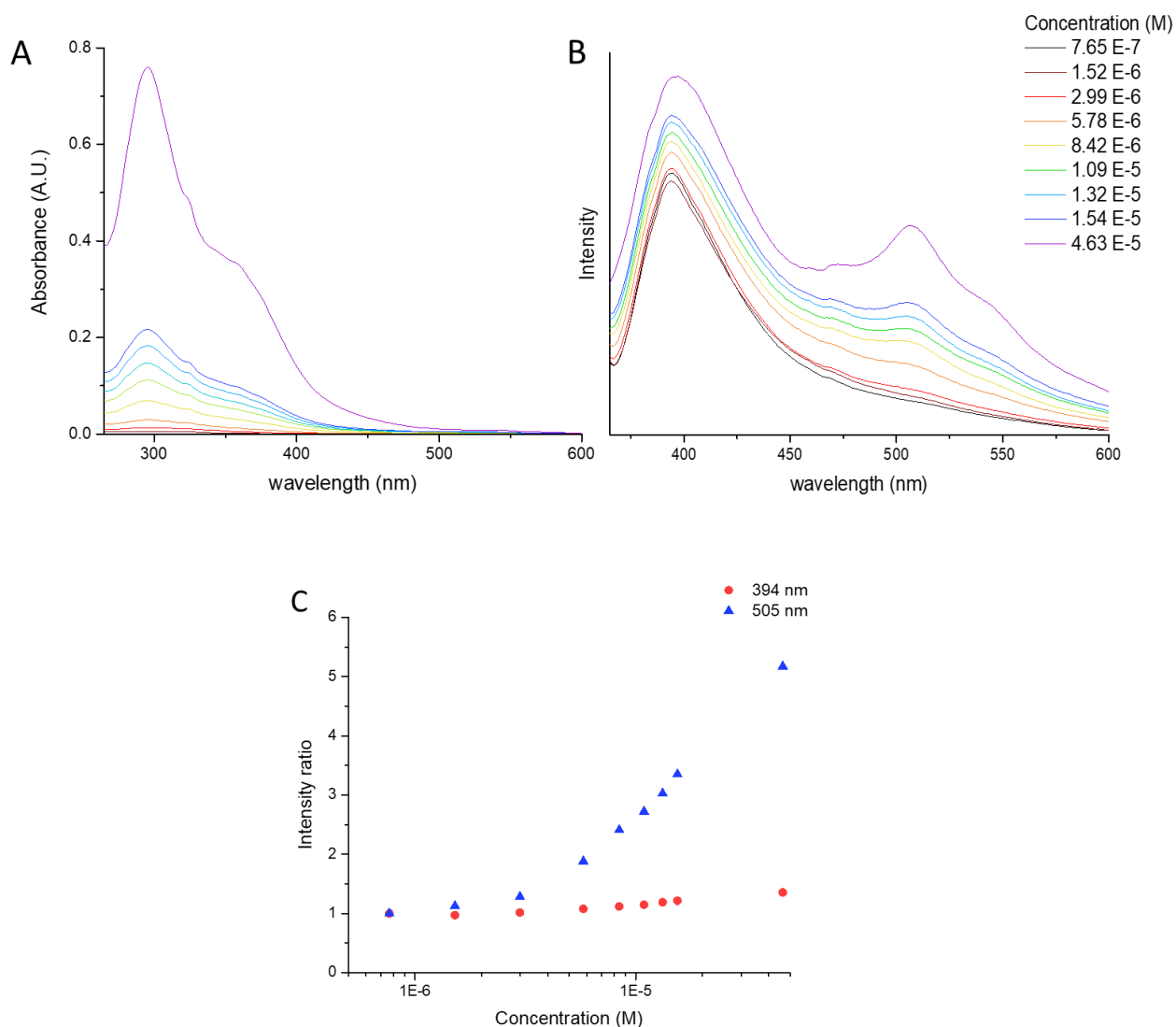


Figure 17: A) Absorption and B) emission (ex 350 nm) spectra of IDQ at a range of concentrations C) Plot of emission intensities at 394 nm and 505 nm versus concentration of IDQ

When plotted as concentration versus a ratio of intensity over the initial intensity (figure 17C), it becomes even clearer that the peak at 505 nm grows at a faster rate than that at 394 nm, indicating that this is not simply an additive consequence of monomer concentration but an increasing proportion of aggregates. The red shifted absorbance maximum indicates that "head-to-tail" type aggregates are the preferred orientation. The emission of these aggregates is important because in the practical application in devices

such as BHJ cells or other thin films, the dyes are not in dilute solution, so these higher order species are the actual active components.

2.2.3 Absorbance and emission of IDQ-SQ and IDQ-SQ-P

After IDQ is coupled with squaraine, IDQ-SQ exhibits an absorbance maximum that has moved from 300 nm all the way to 749 nm, with another local maximum at 689 nm. This is expected as the molecule is planar and the expanded conjugation allows a long pi-cloud across the total molecule. The presence of the two peaks has been previously attributed to the formation of aggregates, where the peak at 689 nm is attributed to parallel type and the peak at 749 nm is attributed to head-to-tail type. This behavior is maintained from the IDQ moiety, as shown above. At the absorbance maximum, the molar extinction coefficient is $279,300 \text{ M}^{-1} \text{ cm}^{-1}$.

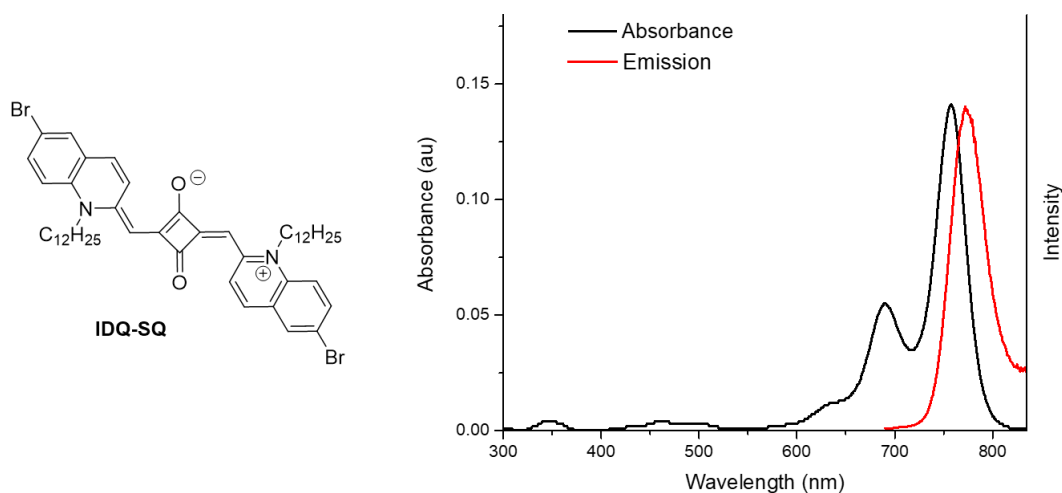


Figure 18: IDQ-SQ structure and spectra showing absorbance and emission (670 nm excitation) at $5.05 \times 10^{-7} \text{ M}$

To look at its emissive properties, the sample was excited with 670 nm light, which should have been able to excite both transitions at 685 nm and 749 nm (figure 18). Only one emission maximum was observed at 774 nm, however, and there was no secondary emission which may have been expected to appear behind the 689 nm absorbance. This indicated that only one aggregate form contributed to this emission. As such the Stokes shift is 25 nm.

After pyrene is added to make IDQ-SQ-P, the changes in absorbance are less significant than they were in the previous step.

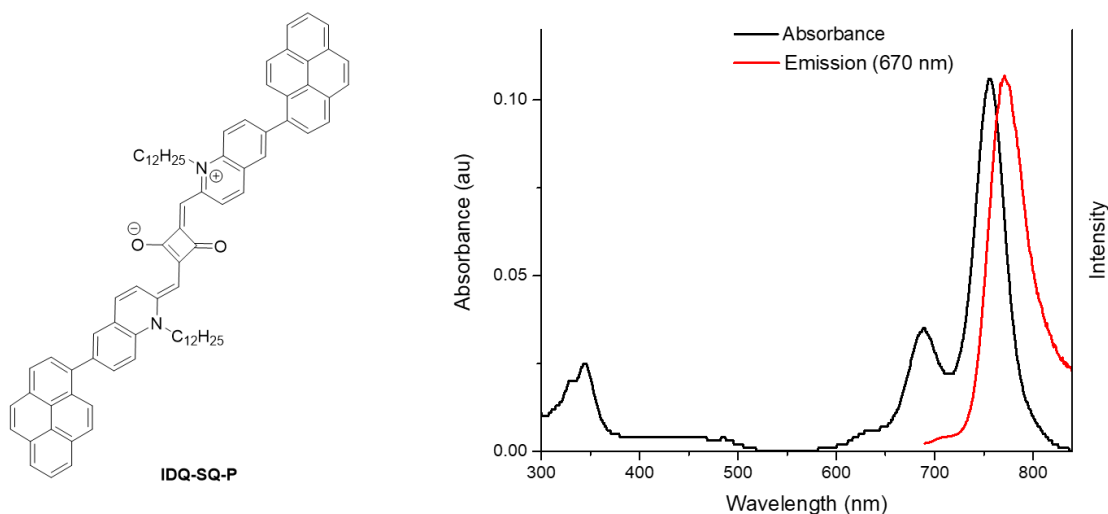


Figure 19: IDQ-SQ-P structure and spectra showing absorbance and emission (670 nm excitation) at 5.01×10^{-7} M

There are two absorbance maxima in the 600 nm to 800 nm range, at 689 nm and 757 nm, which aside from being slightly red shifted are very similar to that of IDQ-SQ (figure 19). At the absorbance maximum, the molar extinction coefficient is $211,500 \text{ M}^{-1} \text{ cm}^{-1}$. The only other major difference in the spectrum is the pyrene absorbance which appears with its characteristic shape at 345 nm. If the pyrene moiety added had contributed to extension of the pi system, it would be expected that the spectra of IDQ-SQ-P would be significantly altered (red-shifted) relative to that of IDQ-SQ. Because this is not seen it suggests that the pyrene moiety is not in conjugation, likely twisted out of plane, and therefore can instead only act as a donor inductively. It may also be that the quinoline-squaraine-quinoline triad has a pi system that operates independently owing to its zwitterionic character, and that the introduction of the pyrene moiety's pi-system was not enough to disrupt it. To confirm which is the reason, crystal structures would need to be attained, which would be able to determine the dihedral angle between the pyrene and quinoline moieties. This factor is also important to electron mobility and BHJ device efficiency.

The emission of IDQ-SQ-P is at 771 nm, which is hypsochromically shifted relative to IDQ-SQ by 3 nm. Slight increase in energy is consistent with inductive donor effects.

2.2.4 Solvent effect on emission

The effects of solvent on the aggregation behavior of IDQ-SQ-P with respect to UV-Vis absorbance data has been previously shown by work in our lab, however even more significant differences in the emission spectra were found in the current investigations. Two emission spectra are shown in figure 20, where both have the same concentration (5×10^{-7} M) and are excited at the pyrene excitation of 345 nm. While the inlay shows that the absorbance spectra do not differ beyond the anticipated solvatochromic shift, the shape of their emission spectra differ significantly. The peak between 400 nm and 500 nm dominates the spectrum when in NMP, and the only other maximum is at 783 nm with just 14% of the intensity of the major emission. In contrast the spectrum taken in chloroform has a more even distribution of emission across the visible spectrum. There is an additional peak present at 710 nm which is entirely absent when in NMP.

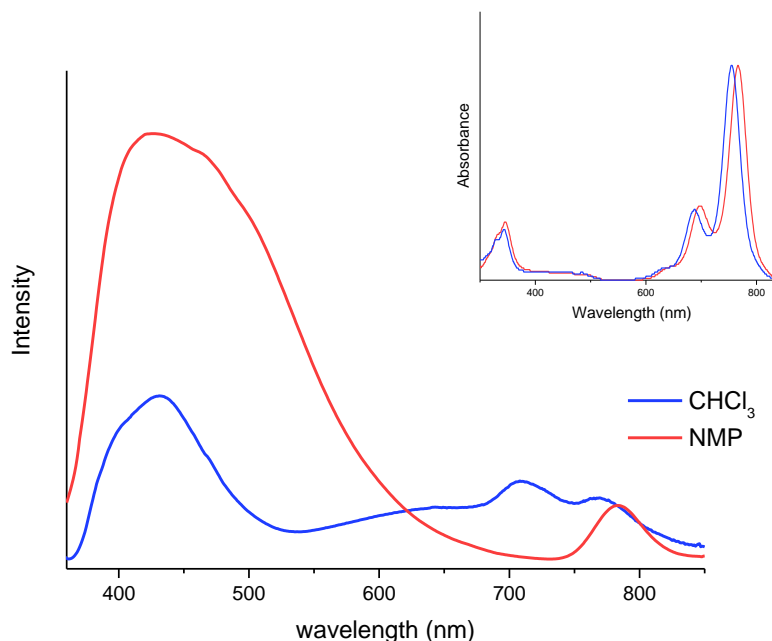


Figure 20: Emission spectra (345 nm excitation) of IDQ-SQ-P in NMP and CHCl₃ with inlay of the respective absorbance spectra

There are a number of factors that may contribute to this observed phenomenon. NMP is known to be an aggregate inducing solvent, and it has previously been shown to facilitate pyrene excimer formation in higher concentrations solutions, which lead emission between 500 nm and 650 nm⁴³. It could be that the excitation of these excimers inhibits the transition that leads to emission 710 nm. It was also hypothesized that it could instead be the basicity of NMP, leading it to coordinate with the positively charged nitrogen on either of

the quinoline moieties, which could disrupt the flow of electrons which normally allows delocalization of charges and as such changes the possible emissive transitions. To test whether this really was a factor, drops of glacial acetic acid were added to IDQ-SQ-P in NMP, as this may disrupt NMP's basicity and hoped to return the original shape of the emission spectra.

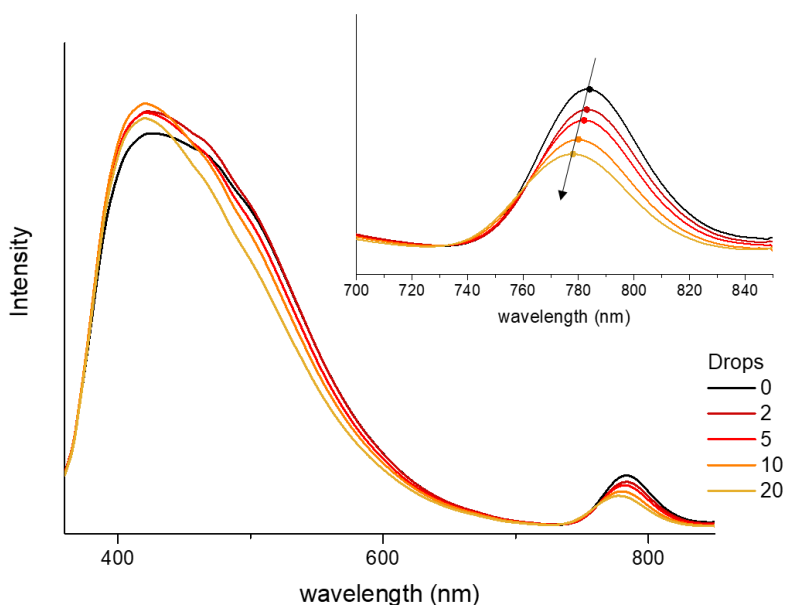


Figure 21: Emission spectra (345 nm excitation) of IDQ-SQ-P in NMP with additions of glacial Acetic Acid

Following a series of additions of acetic acid to the IDQ-SQ-P and NMP solution, absorbance and emission spectra were collected. There was an observable blue shift of the peak which began at 783 nm, as highlighted by the inlay in figure 21, as well as a reduction in emission. This blue shift may indicate instead that the acid protonated the negative oxygen of the squaraine moiety. Blue shifts like this have been observed previously when IDQ-SQ-P was dissolved in protic solvents such as methanol which could participate in hydrogen bonding with said oxygens. The narrowing of the broadness in the major emission peak is likely due to a disruption of pi-pi stacking between pyrene moieties. There was no affect in the region of 710 nm, though. This indicates that the emissive species responsible for this peak was not regenerated through changing pH of the solution, and as such was likely not a consequence of NMP's basicity. Rather it is more likely a consequence of aforementioned pyrene excimer formation.

2.2.5 Energy level determination with cyclic voltammetry

To run cyclic voltammetry measurements across a broad range of voltages, acetonitrile is often a strong choice of solvent, as it has one of the largest windows, covering -3.1 eV to +3.2 eV, and relatively high boiling point⁴⁴. An issue with this is that IDQ-SQ and IDQ-SQ-P have very low solubility in acetonitrile. They have much higher solubility in dichloromethane, but the window of this solvent only spans about -1.7 eV to +1.8 eV and has a very low boiling point. If the solvent used is prone to evaporation it can quickly change the environment in solution, making good measurements difficult to attain. For these reasons CV measurements were attained by using DCM to deposit a film of the dye onto the WE, evaporating the solvent, and then using acetonitrile for the electrolyte solution.

The redox couple of ferrocene/ferrocenium was used as an internal standard for the voltammograms, and all values were calibrated based on this. The $E_{1/2}$ for the IDQ-SQ dye was found to be 0.41 V and for IDQ-SQ-P the $E_{1/2}$ was found to be 0.43 V. The ferrocene/ferrocenium couple is often used as a reference reaction because it has a known reversible reaction within the range of measurement of many organic molecules. While the exact energy of the HOMO of ferrocene is not universally agreed upon, and many simplified equations exist that aim to account for the observed reduction potential in a given cell set up, for this thesis the value of -5.1 eV was used²⁸.

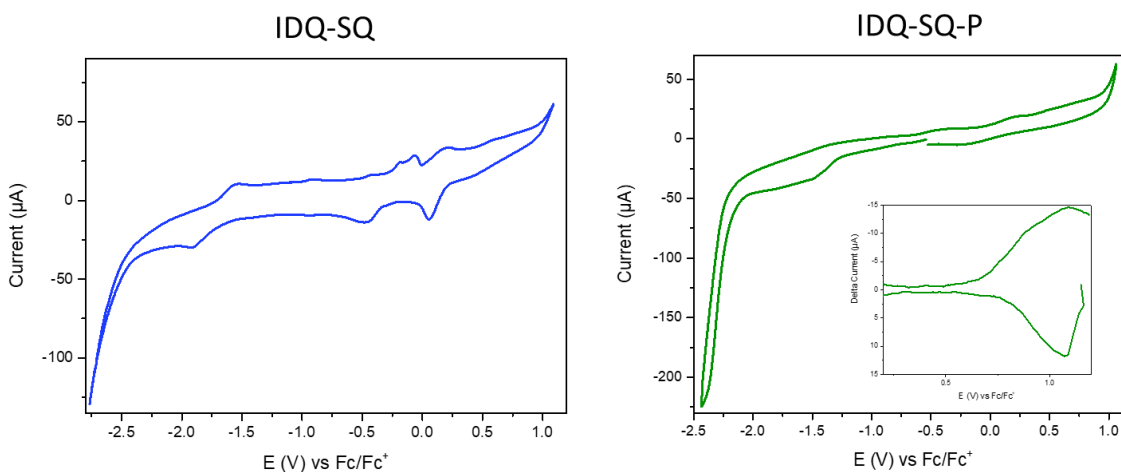


Figure 22: Cyclic voltammograms for IDQ-SQ (blue) and IDQ-SQ-P (green) in solid state, Inset shows DPV of IDQ-SQ-P in the solid state. Electrolyte: 0.1 M TBAPF₆ in CAN. Scan rate: 50 mV/s

Table 5: Energy level data from CV measurements of IDQ-SQ and IDQ-SQ-P

Molecule	$E_{\text{red}}, E_{\text{red}}^{\text{onset}}$ (V)	$E_{\text{ox}}, E_{\text{ox}}^{\text{onset}}$ (V)	LUMO ^a (eV)	HOMO ^a (eV)	E_g^b (eV)	$E_g^{\text{opt } c}$ (eV)
IDQ-SQ	-1.90, -1.75	-0.19, -0.26 -0.07 0.18	3.35	4.84	1.49	1.51
IDQ-SQ-P	-1.44, -1.31	0.21, -0.05 1.09	3.79	5.05	1.26	1.48

^a measured value from CV ^b calculated from LUMO-HOMO ^c calculated from the onset of the major absorbance

The CV trace for IDQ-SQ shows several reversible redox events. Based on the ferrocene HOMO and adjustments described above and the first reduction potential, the E^{LUMO} was found to be -3.35 eV. There are also two reversible oxidation processes near zero, one oxidation peak at -0.19 V, with a second process at -0.07 V and one at 0.18 V. The HOMO level can be estimated by the first oxidation process at -0.19 V (onset at -0.26 V) which yields a HOMO level 4.84 eV. The difference between the electrochemically determined E^{LUMO} and E^{HOMO} gives an energy bandgap of 1.49 eV, which is in excellent agreement with the optically determined bandgap of 1.51 eV. The optical bandgap is determined from the onset of the absorbance peak in the UV-Vis spectra.

Measurement of IDQ-SQ-P resulted in less intense peaks which were at noticeably lower potentials. In this case there is an oxidation process at 0.21 V and a reduction process at -1.44 V. Despite numerous attempts the characteristic oxidation of pyrene could not be observed via cyclic voltammetry but only through differential pulse voltammetry (inset in figure 22). This is centered around 1.09 V in good agreement with other pyrene molecules in the literature. From the onset of the first oxidation (-0.05 V) and reduction (-1.31 V) the HOMO and LUMO are estimated at 5.05 eV and 3.79 eV respectively. The electrochemical bandgap is calculated at 1.26 eV and has a bigger difference from the optical gap than observed in IDQ-SQ, however it is still considered in good agreement with the optically determined bandgap from optical spectroscopy (1.48 eV). Some disagreement between the optical energy gaps and energy gaps determined with CV is, in fact, seen most of the time and caused by differences in the allowed transitions which can be observed with optical methods like UV-Vis and PL and the absolute energies⁴⁵. The decrease in energy of both the E^{HOMO} and E^{LUMO} levels of IDQ-SQ-P relative to IDQ-SQ is surprisingly not consistent with the

inductive electron donor effect of pyrene. It is expected that it should destabilize these energy levels, yet this does not appear to be the case.

The phenomena of one reduction and two oxidation events has been observed in D-A-D type dyes before such as with a dithinenopyrrole-pyrrolopyrrole dye investigated by *Rybakiewicz-Sekita et.al.*⁴⁶. Here they discussed that the formation of two stable cation species, a mono and di cation, would explain the CV results and the ability of the dye to be twice oxidized is a positive sign for exciton dissociation. Additionally, the reversibility of redox events indicates that the ionizations do not result in the formation of new species, such as intramolecular reactions, dimersization, or protonated/deprotonated species⁴⁷. The peaks in the forward and reverse direction are more intense and so easiest seen in the CV trace of IQD-SQ, where the pairs are all offset by about 0.2 eV. In IDQ-SQ-P the peaks are more shallow so the offset of their maxima are more difficult to determine, but the reversibility is likewise seen.

2.2.6 Emission quenching behavior

Although IDQ-SQ and IDQ-SQ-P are very intense chromophores that strongly absorb light within the solar spectrum, there are questions raised by their electrochemical characterizations. One issue is that their HOMO levels are much too high for the typical arrangements of BHJ cells with the fluorine tin oxide (FTO) transparent electrode. The other significant problem is the solubility, as they dye exhibits aggregation even at very low concentrations. In order to establish whether these dyes are able to act as efficient electron donors, some experiments were conducted using exfoliated graphene. The selection of graphene was based on its excellent electron accepting ability and 2D aromatic structure which may be able to stabilize the pyrene moiety of IDQ-SQ-P via pi-pi stacking.

In order to better understand the behavior of such complex systems both the emission quenching of both IDQ-SQ and IDQ-SQ-P by graphene were measured over the course of several the additions of exfoliated graphene. The preparation and quantification of exfoliated graphene suspension was done as described in section 3.3. While the dye was dissolved in CHCl_3 and NMP was used for exfoliation, the graphene was added in microliter quantities with a micropipette, and even at the maximum quantity added NMP never exceeded 1% of the total volume of solvent in the cuvette, and thus determined not to have a meaningful effect on the overall solution. Following each addition of graphene to the dyes in solution, the cuvette was shaken vigorously, then absorption and emission spectra measured.

Upon addition of graphene to the parent molecule IDQ-SQ, the dye exhibited some quenching of its emission peak at 774 nm, though only up to 17% before subsequent additions of graphene made no change to the emission maximum (figure 23). The appearance of an emission at 824 nm at first may have suggested pi stacking with graphene leading to a new emission at a reduced energy, however upon testing a solution of only 120.4 μg graphene in chloroform with no dye, it was confirmed that this emission was independent of IDQ-SQ. This peak does, however, act like an internal standard and aids to support that the plateau in quenching beyond 86 μg graphene was due to a bottle neck in the interaction between IDQ-SQ and graphene, as opposed to an issue of dilution, instrument response, or other, as the increase at 824 nm continues linearly in the same period.

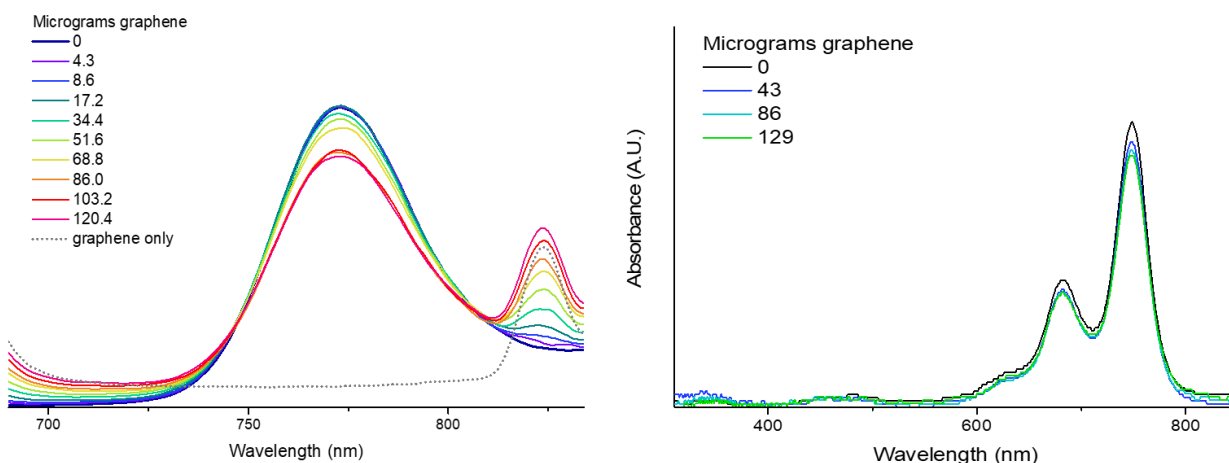


Figure 23: Emission (670 nm excitation) and absorbance spectra of IDQ-SQ in CHCl₃ with additions of graphene

UV-Vis data can aid in the determination of the mechanism of quenching. Because graphene itself absorbs across the visible range, it can make the comparison of mixtures difficult. In order to better compare peaks, three concentrations were selected and absorbance spectra of each of those concentrations of graphene were recorded then subtracted from the spectra of the mixtures. These corrected spectra are shown in figure 23.

As discussed in section 1.6, if pi-pi stacking were occurring between the ground state of IDQ-SQ and graphene, changes to the absorbance would be seen in the UV-Vis spectra, but none were observed. There is no appearance of new peaks or changes to the distribution of the two major absorbances. This suggests that graphene does not engage in static quenching with IDQ-SQ, and any interactions are occurring in the excited state.

The changes in emission that occur when graphene is added to IDQ-SQ-P are significantly more interesting.

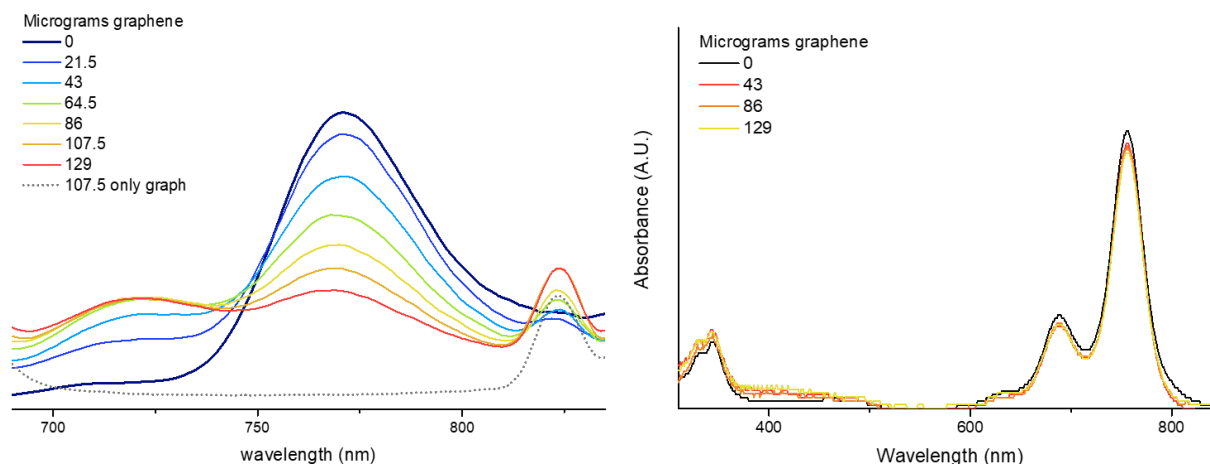


Figure 24: Emission (670 nm excitation) and absorbance spectra of IDQ-SQ-P in CHCl₃ with additions of graphene

Like IDQ-SQ, the UV-Vis spectra do not show any shifts or changes indicative of Static Quenching (figure 24). The emission spectra show a number of changes, however. The major peak at 771 nm can be significantly quenched by graphene. At the same time, the peak at 710 nm which is normally only visible when the dye is excited at higher energy wavelengths is induced. This same recovery of the 710 nm peak was seen when experiments of a similar nature were executed with additions of C₆₀ fullerene to IDQ-SQ-P. Fullerene was chosen as it is a small molecule with well defined optical characteristics that do not interfere with spectral range of interest. It also does not possess any of the structural "uncertainties" that exfoliated graphene can, where the exfoliation process can introduce planar defects that may interfere with conjugation. Fullerenes possess the same affinity for pi-pi stacking that graphene does, and so should be able to interact similarly with the pyrene moiety.

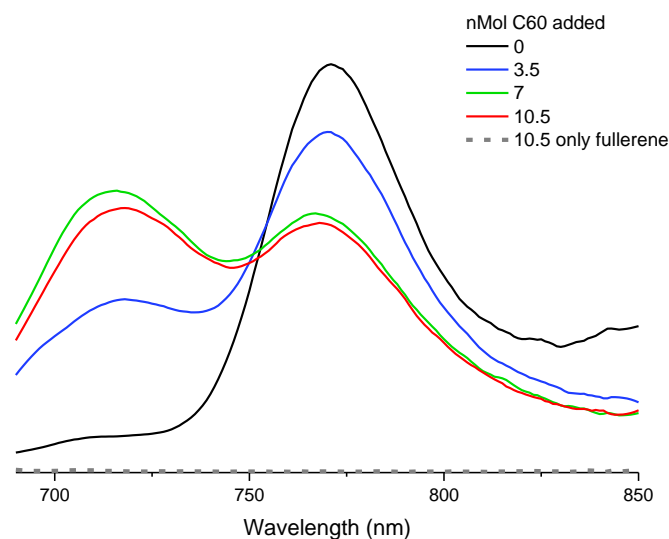


Figure 25: Emission of IDQ-SQ-P (670 excitation) in CHCl₃ with additions of fullerene

Owed to the fact that fullerene is a small molecule with a defined molar mass, more detailed quantities for addition could be calculated based on molar ratio of C₆₀ to IDQ-SQ-P.

Nanomolar equivalents were added such that the ratio of pyrene moieties to fullerene in the sample would be 1:1, 1:2, and 1:3. As seen by the dotted line near the baseline in figure 25, fullerene has no emission in the region measured, so all changes can be attributed to intermolecular interactions. Beyond a 1:2 ratio, little change is seen in the emission, which in addition to the generation of the 710 nm emission peak, supports that this is not simply a matter of the carbon nanomaterials absorbing incident photons before they can escape the sample. The blue shifted emission must therefore result as a consequence of pi stacking with the carbon nanomaterials.

2.2.7 TCSPC for determination of time constants and quenching mechanisms

Time resolved photoluminescence was employed in order to better understand the emissive components of this system and which are affected by interactions with the carbon nanomaterial. Time Correlated Single Photon Counting was executed using a 670 nm picosecond laser to excite IDQ-SQ and IDQ-SQ-P and measure the lifetimes of their relaxation processes.

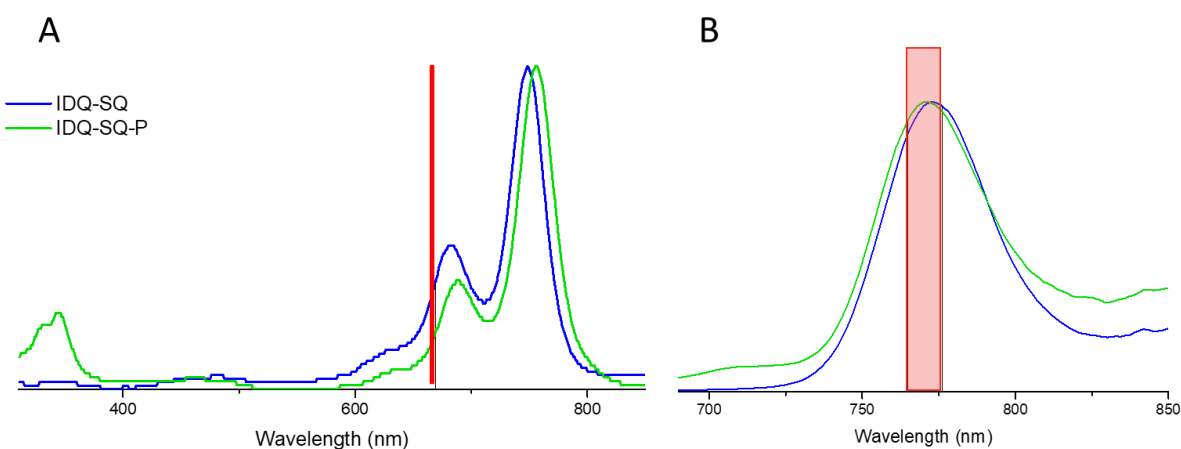


Figure 26: A) Normalized absorbance spectra of IDQ-SQ and IDQ-SQ-P where the red line indicates the excitation of the laser at 670 nm B) Normalized emission spectra where the red box indicates the 10 nm window around 770 nm measured during TCSPC measurements

All TCSPC measurements were taken on solutions of dye at 5×10^{-7} M in CHCl_3 , with a 100 ns pulse period, and 10 nm slit width on the detector (shown in figure 26), until the most populated bin reached 10,000 counts. Decays were also recorded for a mixture of the dyes with graphene. For both dyes, analysis was done with additions of 86 μg graphene, as this would allow an observation of quenching behavior without inhibiting emission so much that measurements would take unreasonable amounts of time. In IDQ-SQ this quantity corresponded to the plateau where no further reduction in emission was observed and in IDQ-SQ-P this corresponded to a 55% reduction in emission. These reductions in emission intensity were directly reflected in the acquisition times.

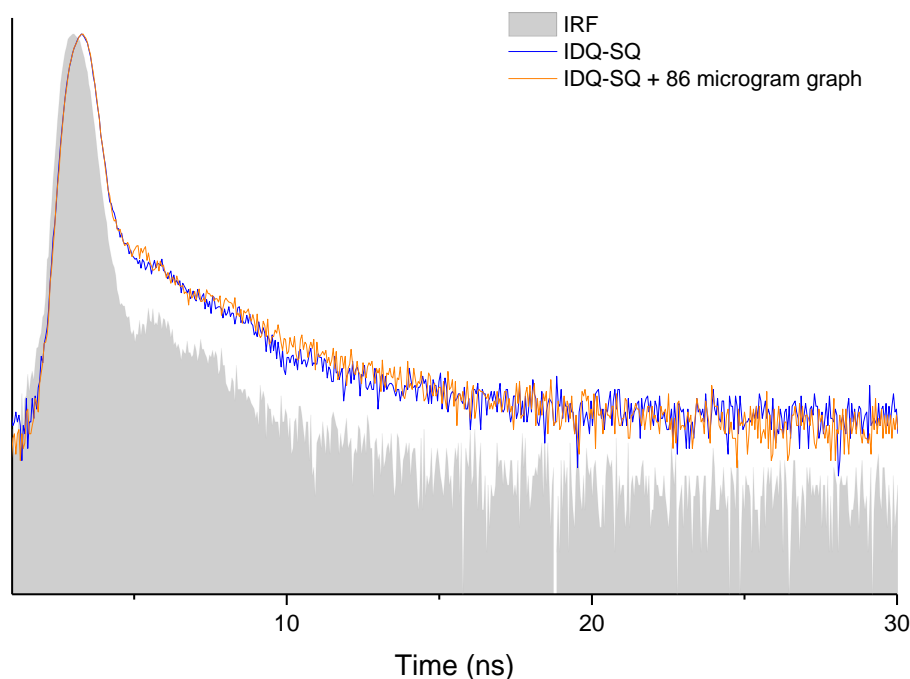


Figure 27: Decay curve of IDQ-SQ with and without graphene, with the instrument response function

Table 6: Time constant parameters determined from fitting functions to the decays of IDQ-SQ with and without graphene

IDQ-SQ		
Parameter	Time (ns)	Population
τ_1	0.0674	91.62
τ_2	3.1922	8.38
χ^2	2.498	

IDQ-SQ + 86 μg graphene		
Parameter	Time (ns)	Population
τ_1	0.0674	88.93
τ_2	3.1922	7.01
τ_3	9.4475	4.07
χ^2	2.644	

The decay of IDQ-SQ shows little visual variation from the instrument response (IRF), indicating that the majority of processes are very fast and near the detection limit of the instrument. A two-term fitting was used as the number of time constants must align with the number of possible transition events that can contribute. There are two emissive components. The slowest emission has a lifetime of ~ 3.1 ns. This can safely be attributed to the direct LUMO to HOMO relaxation of individual IDQ-SQ molecules and accounts for ~ 8.3 % of the counts. The major contribution, however, comes from a 67 picosecond process accounting for about 91.6 % of emission counts. Because there is only IDQ-SQ in the

sample, the logical explanation is to attribute this to excimer pairs where the only emission which can be observed is that which occurs faster than the intermolecular electron/energy transfer that occurs between two neighboring dye molecules. Electron transfer between excimers is expected to take place on the order of tens of picoseconds, so the observed 67 picosecond emission is consistent⁴⁸. It is worth noting that in spite of the low concentration of the solution (on the order of 10^{-7} M) and choice of solvent selected for measurements, the sample is still dominated by excimers and the single molecule emission characteristics are in the minority. Their relatively low contribution is also consistent with the lack of a clear monomer absorbance in absorbance spectra of the same solution.

When graphene is introduced, a third component is added as a 3-exponential solution exhibits better fitting with the observed decay curve. The third process that takes place on the order of 9.5 ns and makes up 4% of total events. The third component of the system appears to have the longest lifetime. As evidenced by the modest emission quenching results between the IDQ-SQ and graphene nanoparticles (figure 23) there should be little interaction between the two components. Additional experiments are required to understand the nature of a third component emissive at 770 nm with a lifetime of ~ 9 ns in this system.

While the χ^2 values for the fits reported are not as close to one as is preferred, if only one type of emission event is assumed, the fitting becomes significantly worse, having a χ^2 of 8.8. It should be noted that the addition of extra terms did not improve χ^2 values to a degree that supported them having any physical meaning, so the reported values are the best possible fits with a number of time constants which have meaning in the system.

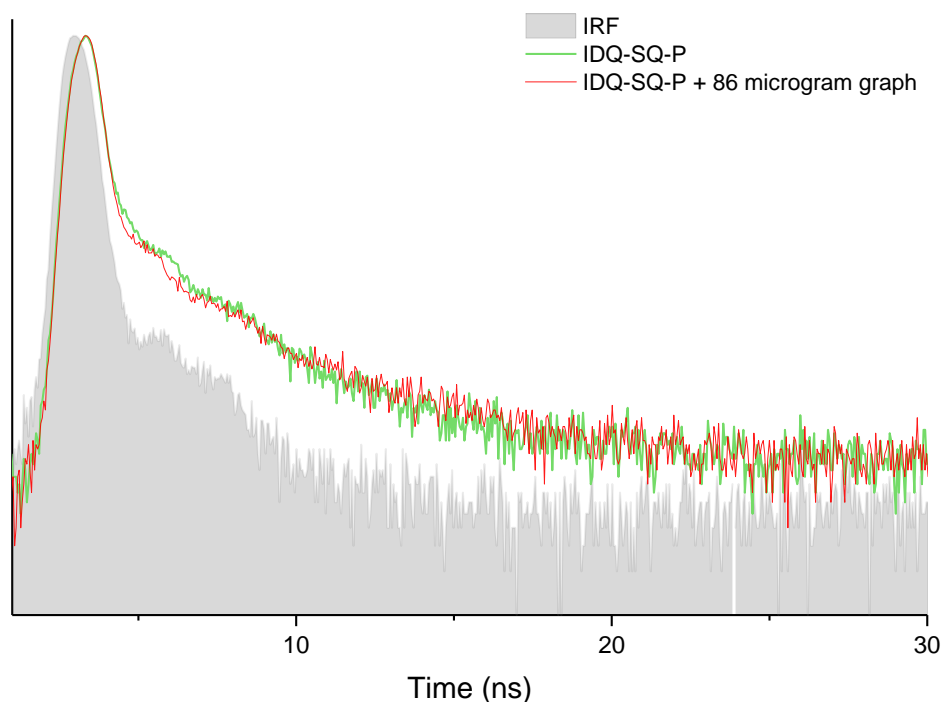


Figure 28: Decay curve of IDQ-SQ-P with and without graphene, with the instrument response function

Table 7: Time constant parameters determined from fitting functions to the decays of IDQ-SQ-P with and without graphene

IDQ-SQ-P		
Parameter	Time (ns)	Population
τ_1	0.0634	84.71
τ_2	2.5761	11.69
τ_3	3.6976	3.61
χ^2	2.986	100

IDQ-SQ-P + 86 μg graphene		
Parameter	Time (ns)	Population
τ_1	0.0634	84.95
τ_2	2.5761	8.14
τ_3	3.6976	2.33
τ_4	16.6343	4.57
χ^2	2.594	100

In IDQ-SQ-P, an extra potential electron transfer event which would inhibit emission has been introduced by the addition of pyrene. This is why an extra term has been added to the fitting equation. The fastest term, τ_1 for IDQ-SQ-P is nearly the same as in IDQ-SQ, at 63

picooseconds, though slightly reduced. This is still attributed to the intramolecular quinoline-squaraine core's excimer interaction. The reduction in time may be because pairs are more tightly held to each other by pi-pi stacking between pyrene moieties, allowing for faster electron transfer. On the other hand the decrease in population from ~92% in IDQ-SQ to ~85% in IDQ-SQ-P may be a result of the more complex geometry of IDQ-SQ-P which requires a more specific orientation of the molecules to be able to come together and form the exciton pair. The second time constant, τ_2 , is 2.6 nanoseconds, and has been attributed to an electron transfer directly related to the pyrene moieties. It was considered whether an intramolecular electron transfer could occur as electron transfers from the donor to the excited acceptor moiety of molecules have been shown to occur on the order of 1-10 ns in other molecules where the donor and acceptor are perpendicular to each other^{48,49}. The electronic structure of IDQ-SQ-P, however, does not exhibit characteristics that would allow this to happen at the excitation wavelength used. The excitation of pyrene is much higher in energy, with its absorbance maximum at 345 nm. Even considering the ground state of the pyrene moiety, cyclic voltammetry determined that the HOMO of pyrene lies at -6.19 eV, which is far below the energy levels of the core of the molecule and the uphill transition would not occur. With this in mind, the 2.6 nanosecond time constant has been attributed to an interaction between pi-pi stacked ground state pyrenes which would lead to the inhibition of the 770 nm emission. At 3.7 nanoseconds, τ_3 is the direct HOMO-LUMO relaxation of the IDQ-SQ core in the individual molecule.

There lifetime of the excited state of a molecule can be affected by many factors, and solvent plays many different roles. Previous research in our lab performed TCSPC of IDQ-SQ-P in NMP and found time constants of 40 ps (90%), 1.85 ns (6%), and 5.92 ns (5%)⁴³. Comparing the two, the lifetime τ_1 is 24 picoseconds longer in chloroform than in NMP. The difference in lifetime associated with the excimer pair relaxation may be owed to the increased aggregation induced by NMP. Likewise the promotion of aggregation would affect τ_2 in the same way, however the tighter proximity may make the excimer relaxation pathway even more favorable than the pyrene-pyrene pathway, leading to the decreased population of τ_2 and increase in τ_1 . In addition to proximity, there is a positive correlation between the polarity of the solvent and the rate of ICT, and therefore a negative correlation with observed lifetime⁵⁰. NMP is significantly more polar than chloroform, where the former has a dielectric constant of 32 and the latter 4.8⁵¹, giving it a greater ability to stabilize intermolecular electron transfers as it can reorganize in a way that allows charges to survive in solution. These effects help support the assignment of τ_2 to an intermolecular phenomenon. With respect to the fluorescence of the LUMO to HOMO relaxation, there is a

correlation between excited state lifetime and solvent viscosity. An increased viscosity inhibits intramolecular motions like rotation which lead to non-radiative relaxations, therefore allowing for longer excited state lifetimes. This follows with the increase in τ_3 from 3.7 ns in chloroform to 5.92 ns in NMP, because the viscosity of NMP is significantly higher than that of chloroform (cp of 1.67 versus 0.58)⁵². With only two solvents these trends cannot be attributed for certain, but they follow with theory and observations of other chromophores.

Upon addition of graphene to IDQ-SQ-P, lifetimes are essentially maintained but a significant difference in the population distribution is observed. Most clearly, the addition of graphene reduces the electron/energy transfer contribution from 11.7% to 2.1%. This can be explained by pi-pi stacking of graphene with the pyrene moiety inhibiting the ability of pyrene's electrons to participate in intermolecular interactions with other IDQ-SQ-P molecules. The redistribution of the lost contribution from τ_2 leads to an ~ 3 % increase in observed emissions faster than exciton pair electron transfer and the remainder is from the lifetime of the LUMO-HOMO relaxation. The lifetime increase of ~ 270 picoseconds could be the result of decreased motion allowed in pi-pi stacked IDQ-SQ-P, similarly to the effect described with NMP. Although the addition of another component to the system may sometimes necessitate the addition of another time constant, it is important to remember that the time constants represent relaxation pathways that inhibit a given fluorescence pathway, and not necessarily physical components. With the addition of graphene to IDQ-SQ-P, the three component fit remained the most logical with respect to the χ^2 values. As a result of the fast component being so close to the instrument response time, it is possible that the interaction between graphene and IDQ-SQ-P that is responsible for the 55% quenching of the 770 nm emission peak is too fast for quantification with the instrument available for this study. In this case τ_1 would be an average of two processes. If the graphene is instead not able to directly interact with the IDQ-SQ core such that it introduces a new relaxation pathway, only inhibiting the role of pyrene, then this also means that the three component fit is correct.

While not immediately obvious, the fact that there is very little difference between the decays of IDQ-SQ and IDQ-SQ-P makes sense. As previously discussed the addition of pyrene did not expand pi conjugation in the molecule, either as a result of geometric constraints or the zwitterionic core maintaining an independent pi system, and thus its orbitals did not mix with the quinoline-squaraine core. The excitement local to pyrene lies at

much higher energies, with its major absorbance is at 345 nm, so the 670 nm laser is not anticipated to excite the pyrene, and so the emission being measured is still only attributed to the IDQ-SQ moiety emission.

2.2.8 Applying photophysical and electrochemical data to possible device function

When looking at the practical application of an organic semiconductor in BHJ devices, one very important aspect of the donor is its compatibility with the electrode to allow hole transport. Upon dissociation of the exciton, holes travel through the donor bulk to the electrode in order to facilitate the positively charged side of current generation. Two commonly used electrodes are fluorene doped tin oxide (FTO) and indium doped tin oxide (ITO), as they are transparent and allow light to reach the solar absorbing materials^{53,54}.

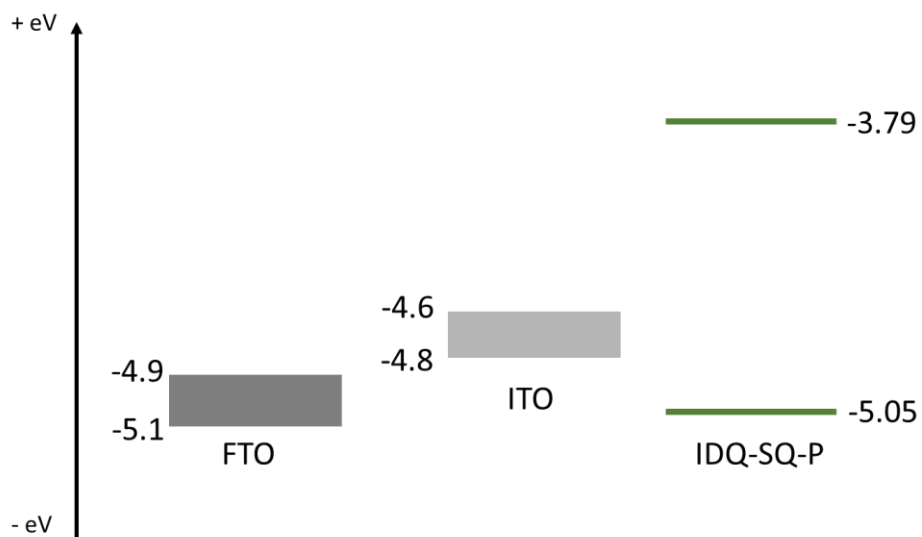


Figure 29: Energy levels of IDQ-SQ-P and the work functions of FTO and ITO electrodes

The issue regarding IDQ-SQ-P is that the HOMO level is high relative to most commonly applied donors (figure 29). The HOMO of a donor that is too close in energy to the work function of the electrode may allow hole transfer but it does this, in fact, too easily. The similarity in the energy levels means that back transfer is almost just as likely to occur causing recombination and inhibiting current generation. In the case of IDQ-SQ-P with its HOMO of -5.05 eV, it is essentially identical to the work function of FTO and thus is not expected to result in a well-functioning device. Comparing with ITO, there is about 0.3 eV difference between the HOMO and work function of the electrode. This has the potential to allow for hole transport without back recombination, however there is a certain degree of

bending of energy levels which occurs at the interface which may result in a reduction of the hole transport barrier as well⁵⁵. In materials with a similar difference between HOMO and work function it has been shown that is possible to employ the use of hole transport materials such as MoO₃ to improve several parameters of the device including current generation, open circuit voltage, and fill factor⁵⁶. These materials are able to promote efficient hole extraction through the creation of a built-in electric field near the interface of the donor and electrode⁵⁷.

The compatibility of IDQ-SQ-P with common acceptor materials such as PCBM is a different issue. Attention needs to be given to the difference between the LUMOs of the two materials. The dissociation of the exciton into the charge transfer state must be favorable, with no positive barrier, as well as a greater decrease than the binding energy of the exciton. It has been shown that the average binding energy of the exciton at the interface is 0.4 eV, so the energy offset between LUMOs should be greater than 0.5 eV⁴. PCBM has a LUMO level of -3.7 eV⁷, and so in a theoretical system of IDQ-SQ-P and PCBM, there is virtually no difference in the energy levels, with the donor potentially even having the lower LUMO. In this system there would be no driving force for charge transfer, and thus charge separation to generate current.

While IDQ-SQ-P exhibits intense absorbance of red light and an affinity for charge separation as evidenced by the high population of ICT between molecules in the aggregated dye seen from the TCSPC experiments, it is not a good candidate as a donor for BHJ cells as they are constructed today. Modifications to the dye should focus on combating aggregation and lowering the HOMO level. The use of branched alkyl groups on the quinoline moiety nitrogen is one way to do this. The installation of bulky groups on the donor moieties would also help inhibit this tendency. On the other hand, lowering the HOMO would likely require the addition of electron withdrawing groups, as shown in section 1.4. IDQ-SQ based molecules with other donor moieties, such as carbazole or phenothiazine, installed on the quinolines may help facilitate these adjustments and lead to improvement in the electronic characteristics.

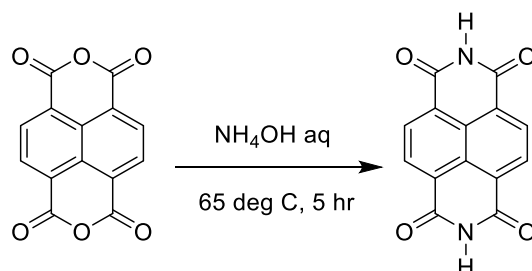
3 Methods

All reagents used in synthesis were purchased from Sigma Aldrich.

Reactions with microwave irradiation were executed with a Biotage Initiator+ and the built in software. Power level: 70 Watts, FHT: off, Cooling: on, Pressure: 5 bar

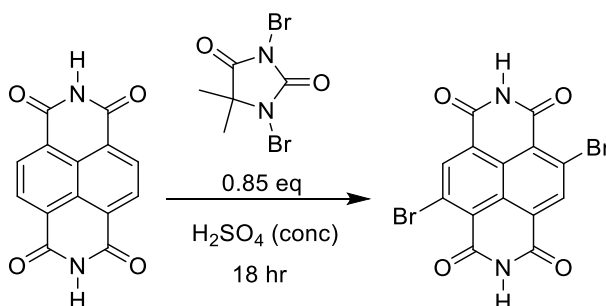
3.1 Synthetic methods for molecules based on naphthalenediimide core

3.1.1 Immidation of 1,4,5,8-naphthalenetetracarboxylic dianhydride



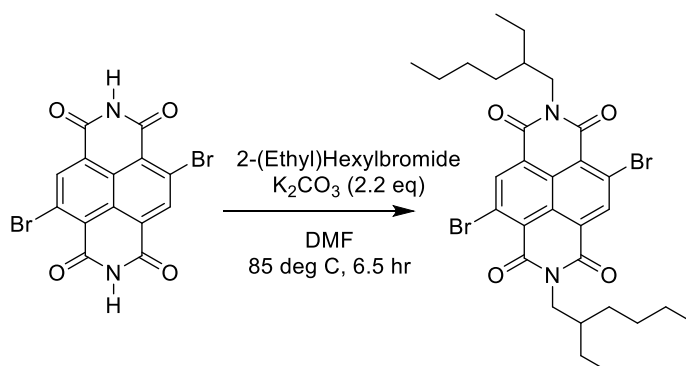
1,4,5,8-naphthalenetetracarboxylic dianhydride (4.26 mmol) was stirred in ammonium hydroxide solution (57.0 mL, 30 w/w%) at 65°C for 5 hours under inert atmosphere. The reaction solution was then poured into ice (200 mL), followed by vacuum filtration to collect the beige/pink solid product, X (0.59 g), in 52 % yield. $^1\text{H NMR}$ ($\text{d}_6\text{-DMSO}$, 600 MHz, ppm) δ 11.93 (s, 2H), 8.62 (s, 4H)

3.1.2 Dibromination of 1,4,5,8-naphthalenetetracarboxylic diimide



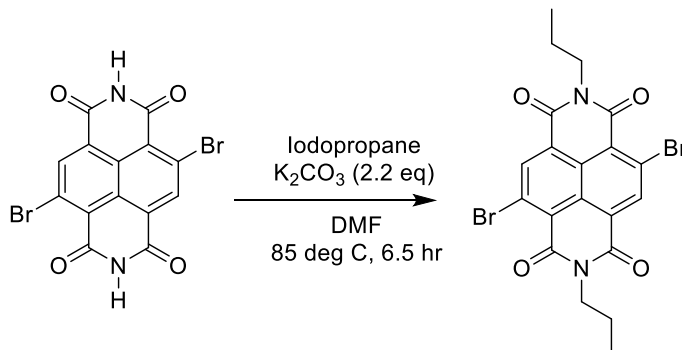
1,4,5,8-naphthalenetetracarboxylic diimide (1.5 mmol) was dissolved in concentrated H_2SO_4 (96%, 6.8 mL). The reaction mixture was cooled to 0°C and protected from light. 1,3-Dibromo -5,5-dimethylhydantoin (1.1 eq, 1.65 mmol) was added in parts over 30 minutes. The reaction was stirred for 18 hours before it was quenched by pouring into ice (200 g) and allowed to stand for one hour. The bright yellow solid was then collected via vacuum filtration, where it was washed with water (100 mL) then methanol (25 mL). The solid was dried under reduced pressure, leaving 0.57g of X (90 % yield). $^1\text{H NMR}$ ($\text{d}_6\text{-DMSO}$, 600 MHz, ppm) δ 12.10 (s, 2H), 8.61 (s, 2H) MS calcd for M^+ $\text{C}_{14}\text{H}_5\text{Br}_2\text{N}_2\text{O}_4$: 422.8616, found 422.8620

3.1.3 Alkylation of 2Br-NDI with 2-(Ethyl)-Hexyl bromide



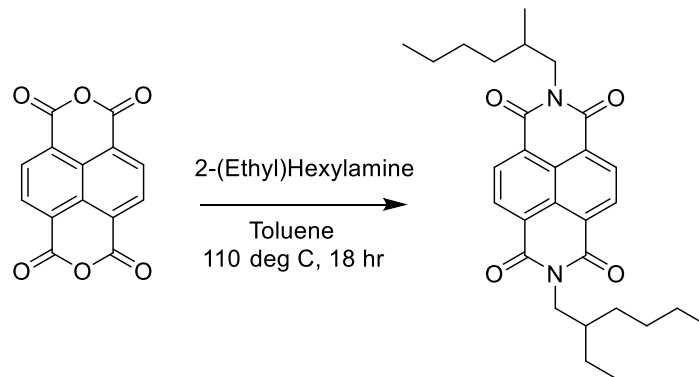
2Br-NDI (94.5 mg, 0.22 mmol) and K_2CO_3 (0.075, 0.52 mmol) were combined and dried under vacuum, then refilled and kept under inert atmosphere. The solids were dissolved in dry Dimethyl Formamide (4.5 mL). 2-(Ethyl)-hexyl bromide (0.15 mL, 0.80 mmol) was added, then the reaction mixture was stirred at 85°C for 6.5 hr. The reaction was removed from heat and solvent removed under vacuum. The crude product was reconstituted in $CHCl_3$ (20 mL), the organic layer was washed with H_2O (3 x 10 mL), then the aqueous layer was extracted with $CHCl_3$ (2 x 10 mL). The organic layers were combined, dried with Na_2SO_4 , and filtered. The volume was reduced under vacuum before the mixture transferred to a centrifugation vial, then dried under high vacuum. Acetone (10 mL) was added to the crude solid and it was sonicated for 30 seconds. The mixture was centrifuged at 4k rpm for 5 minutes, then the supernatant removed. This was repeated twice more. The remaining yellow solid product was collected and dried under vacuum, resulting in a 19% yield (26.6 mg, 0.041 mmol) 1H NMR (600 MHz, $CDCl_3$) δ : 9.00 (s, 2H), 4.15 (dq, 4H), 1.94 (sept, 2H), 1.34-1.42 (m, 8H), 1.28-1.32 (m, 8H), 0.94 (t, 6H), 0.88 (t, 6H), ^{13}C NMR (600 MHz, $CDCl_3$) δ : 161.26, 161.19, 139.32, 128.52, 127.91, 125.43, 124.23, 45.29, 37.91, 30.76, 28.67, 24.11, 23.21, 14.22, 10.71

3.1.4 Alkylation of 2Br-NDI with Iodo-propane



2Br-NDI (104.0 mg, 0.25 mmol) and K₂CO₃ (0.0765, 0.52 mmol) were combined and dried under vacuum, then refilled with and kept under inert atmosphere. The solids were then dissolved in dry Dimethyl Formamide (4.5 mL). Iodo-propane (0.09 mL, 0.88 mmol) was added, then the reaction mixture was stirred at 85°C for 6.5 hr. The reaction was removed from heat and solvent removed under vacuum. The crude product was reconstituted in CHCl₃ (20 mL), the organic layer was washed with H₂O (3 x 10 mL), then the aqueous layer was extracted with CHCl₃ (2 x 10 mL). The organic layers were combined, dried with Na₂SO₄, and filtered. The volume was reduced under vacuum before the mixture transferred to a centrifugation vial, then dried under high vacuum. Acetone (10 mL) was added to the crude solid and it was sonicated for 30 seconds. The mixture was centrifuged at 4k rpm for 5 minutes, then the supernatant removed. This was repeated twice more. The remaining beige solid product was collected and dried under vacuum, resulting in a 25% yield of 80% pure product (30.1 mg, 0.061 mmol) ¹H NMR (400 MHz, CDCl₃) δ: 9.00 (s, 2H), 4.17 (t, 4H), 1.78 (q, 4H), 1.03 (t, 6H)

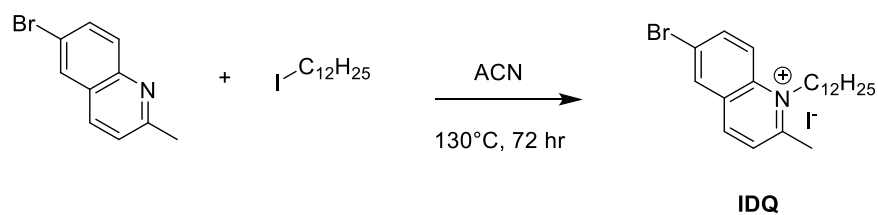
3.1.5 Imidation of naphthalene dianhydride with ethyl hexyl amine



1,4,5,8-naphthalenetetracarboxylic dianhydride (1.003 g, 3.74 mmol) and 2-(ethyl)-hexyl amine (1.3 mL, 7.9 mmol) were dissolved in toluene (dry, 15 mL). The reaction mixture was stirred at 110°C for 18 hours under inert atmosphere. The reaction was allowed to cool, then the solvent was removed under vacuum. The crude product was reconstituted in CHCl_3 (20 mL), the organic layer was washed with H_2O (3 x 10 mL), then the aqueous layer was extracted with CHCl_3 (2 x 10 mL). The organic layers were combined, dried with Na_2SO_4 , and filtered. The volume was reduced under vacuum before the mixture transferred to a centrifugation vial, then dried under high vacuum. Acetone (10 mL) was added to the crude solid and it was sonicated for 30 seconds. The mixture was centrifuged at 4k rpm for 5 minutes, then the supernatant removed. This was repeated twice more. The product, N,N'-bis(2-ethylhexyl)-1,4,5,8-naphthalenetetracarboxydiimide, was a white solid, collected at 25% yield (0.46 g, 0.94 mmol). ^1H NMR (600 MHz, CDCl_3) δ : 8.75 (s, 4H), 4.13 (dq, 4H), 1.93 (sept, 2H), 1.26-1.42 (m, 16H), 0.93 (t, 6H), 0.88 (t, 6H), ^{13}C NMR (600 MHz, CDCl_3) δ : 163.37, 131.16, 126.88, 126.73, 44.74, 38.08, 30.83, 28.77, 24.17, 23.18, 14.21, 10.74

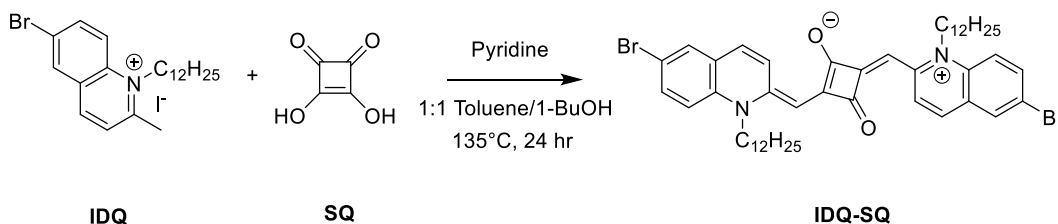
3.2 Synthesis of dye based on squaraine core

3.2.1 Alkylation of quinoline with iodododecane



6-bromo-2-methylquinoline (1.00 g, 4,50 mmol) and iodododecane (1.788 g, 6,0 mmol) were dissolved in acetonitrile (3 mL) in a microwave vial then sealed with a septum cap. The reaction solution was stirred at 130°C for 72 hours. After the reaction mixture was cooled, the solvent was removed under reduced pressure. The crude solid was added to Ethyl Acetate and centrifuged at 4000 rpm for 5 minutes, then the supernatant removed. This was repeated until pure product remained. The recovered 6-Bromo- *N*-dodecyl-2-methyl-quinolinium iodine salt was a yellow/orange solid, and a final yield of 47% (1.10 g, 1,36 mmol) was obtained. ¹H NMR (400 MHz, CDCl₃) δ: 0.90 (t, 3H), 1,27 (s, 14H), 1.41 (p, 2H), 1.65 (p, 2H), 2,00 (p, 2H), 3.35 (s, 3H), 5.09 (t, 2H), 8.06 (d, 1H), 8.21 (d, 1H), 8.28 (d, 1H), 8.37 (m, 1H), 8.78 (d, 1H).

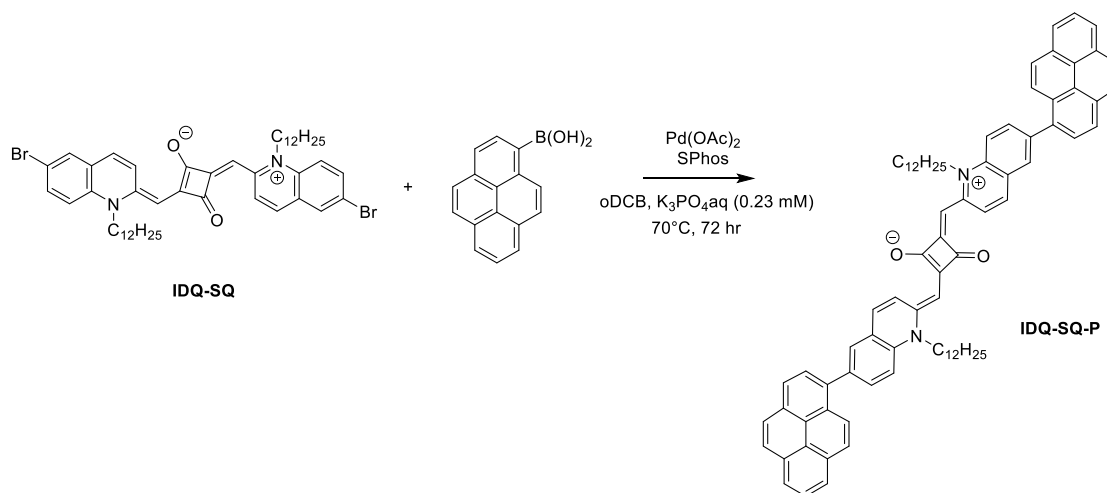
3.2.2 Di-substitution of squaric acid with 6-bromo- *N*-dodecyl-2-methyl-quinolinium



6-Bromo- *N*-dodecyl-2-methyl-quinolinium iodine salt (0.411 g, 0.79 mmol) and squaric acid (0.041 g, 0.36 mmol) were combined with pyridine (1.0 mL) and dissolved in a mixture of toluene and 1-BuOH (1:1) in a dean-stark apparatus under an inert atmosphere. The reaction was heated to reflux (135°C) and stirred for 24 hours. The solvent was removed under reduced pressure. The crude product was reconstituted in methanol and then allowed to precipitate while the solution stirred overnight, then vacuum filtered. The insoluble orange/red powder was the product, (Z)-4-((6-bromo-1-dodecylquinolinium-2-yl)methylene)-2-(((E)-6-bromo-1-dodecylquinolin-2(1H)-ylidene)methyl)-3-

oxocyclobutenolate, recovered at 70% yield. Rf: 0.92 (dichloromethane/MeOH, 90:10) ^1H NMR (400 MHz, CDCl_3) δ : 9.35 (d, 1H, $J = 10.18$ Hz), 7.58 (m, 2H, $J = 8.9$ Hz), 7.31 (d, 1H, $J = 7.6$ Hz), 7.16 (d, 1H, $J = 8.9$ Hz), 5.77 (s, 1H), 4.11 (t, 2H, $J = 8.4$ Hz), 1.84 (m, 2H, $J =$ unresolved), 1.52 (m, 2H, $J = 8.3$ Hz), 1.42 (m, 2H, $J =$ unresolved), 1.26 (m, 14H, $J = 8.3$ Hz), 0.88 (m, 3H, $J = 6.5$ Hz)

3.2.3 Suzuki coupling of Pyrene and IDQ-SQ



IDQ-SQ (0.100 g, 0.101 mmol) and pyrene-1-boronic acid (0.86 g, 0.35 mmol) were dissolved in 1,2 dichlorobenzene and degassed with nitrogen gas for 30 minutes. In another flask, $\text{Pd}(\text{OAc})_2$ (0.003 g, 0.013 mmol) and SPhos (0.016 g, 0.039 mmol) were combined, before the IDQ-SQ/Pyrene-1-boronic acid solution was added. The reaction mixture was then heated to 70°C and reacted for 72 hr. An aqueous solution of K_3PO_4 (degassed, 3 ml, 0.23 mM) was added in portions throughout the reaction. The reaction mixture extracted with chloroform (2 x 50 mL), organic phases were combined and dried with MgSO_4 . Solvents were removed under reduced pressure. The crude product was purified via Soxhlet, with MeOH as the washing solvent overnight, then the product was collected with CHCl_3 . A final yield of 56% (0.07g, 0.56 mmol) was obtained, Rf : 0,53 (CHCl_3 :MeOH 90:10) , ^1H NMR (400 MHz, CDCl_3) δ : 0.87 (t, 6H), 1.27 (s, 26H), 1.92 (m, 4H), 4.18 (t, 4H), 5.82 (s, 2H), 7.44 (d, 2H), 7.52 (d, 2H), 7.74 (s, 2H), 7.77 (d, 2H), 7.97 – 8.25 (m, 18H), 9.42 (d, 2H). ^{13}C NMR (400 MHz, CDCl_3) δ : 14.15, 22.72, 26.77, 26.98, 29.38, 29.44, 29.62, 29.67, 29.70, 29.98, 31.94, 48.20, 93.01, 114.33, 124.51, 124.85, 125.03, 125.40, 126.20, 127.28, 127.38, 127.56, 128.50, 130.09, 130.20, 131.49, 131.67, 132.64, 133.48, 135.71, 136.72, 138.88, 150.05, 150.09

3.3 Preparation of graphene

3.3.1 Exfoliation by sonification

Graphene flakes (12 mg) were added to NMP (20 mL) then the mixture was sonicated with a Bandelin SONOPULS HD 2000.2 homogenizer using a MS 72 probe tip at 90% power for three 30 min sessions, with 30 min intervals between each. Following sonication, the solution was centrifuged for 5 min at 4k rpm, and the supernatant collected for use in the experiments.

3.3.2 Quantification with Thermogravimetric Analysis

The procedure described above was repeated to make three batches of exfoliated graphene, which were then combined. To quantify how much exfoliated graphene was suspended, 1.5 mL of the combined graphene suspension was added to a platinum pan and the solvent evaporated off to deposit the graphene on the TGA pan. Once loaded into the instrument, the pan was heated to 250°C for 40 minutes to ensure the removal of residual solvents, after which the mass stabilized at 647 μg . It was therefore determined that the exfoliated graphene solution had a concentration of 0.43 mg/mL. All thermogravimetric analysis was performed on a TA instruments TGA Q55 under N_2 atmosphere.

3.3.3 Photophysical characterization

3.3.4 Ultraviolet Visible spectroscopy

UV-Vis spectroscopy was completed using a HitachiU-1900 spectrometer and 10 mm quartz cuvettes

3.3.5 Photoluminescence spectroscopy

PL spectroscopy was completed using an Edinburgh Instruments Spectrofluorometer FS3 and Fluoracle software

3.3.6 Time Correlated Single Photon Counting

TCSPC was completed with the Edinburgh Instruments Spectrofluorometer FS3 and an Edinburgh Instruments 670 nm laser with 64.6 ps pulse width. Analysis was assisted with Fluoracle software.

3.3.7 Cyclic Voltammetry

CV experiments were completed using platinum electrodes, tetrabutylammonium hexafluorophosphate electrolyte, the Ametek Scientific Instruments VersaSTAT 3, and VersaStudio software

Ferrocene was purified by sublimation at 110°C

4 Conclusion

Synthesis of newly designed NDI based semiconducting molecules was undertaken and the procedures for the first steps developed. The poor solubility of the core NDI structure complicated the synthetic process, and the addition of alkyl groups was determined to be necessary as soon in the synthetic process as possible, at the expense of ease of later modulation. Recommendations for future synthesis include the use of acid catalyzed imidation, as opposed to the base mediated methods used in this work.

Focus was then placed on the development of donor type semiconductors. Improvements in purification and scaling up of reactions for gram scale synthesis of IDQ-SQ-P were achieved prior to the photophysical and electrochemical characterization of the chromophore. The aggregation behavior of the molecule and its precursors were characterized with UV-Vis and PL spectroscopy, where it was found that even at concentrations on the order of 10^{-7} M, aggregates dominate the solution. Investigation of the emission quenching of IDQ-SQ and IDQ-SQ-P with graphene showed a strong difference between the two molecules, indicating that the pyrene moieties and pi-pi stacking play an important role in the mechanism of relaxation in IDQ-SQ-P. Electrochemical characterization found that while the absorbance profiles of IDQ-SQ and ISQ-SQ-P are nearly identical at their major absorbances, the addition of pyrene had a marked effect on the frontier energy levels. The HOMO and LUMO levels of IDQ-SQ-P were found to be -5.05 eV and -3.79 eV respectively (IDQ-SQ has -4.84 eV and -3.35 eV). These energy levels are incompatible with materials currently used in BHJ devices, so modification to IDQ-SQ-P will need to be made, with specific focus on combating aggregation and lowering its HOMO energy level.

5 References

- (1) Spanggaard, H.; Krebs, F. C. A Brief History of the Development of Organic and Polymeric Photovoltaics. *Solar Energy Materials and Solar Cells* **2004**, *83* (2–3), 125–146. <https://doi.org/10.1016/j.solmat.2004.02.021>.
- (2) Ghosh, A. K.; Morel, D. L.; Feng, T.; Shaw, R. F.; Rowe, C. A. Photovoltaic and Rectification Properties of Al/Mg Phthalocyanine/Ag Schottky-barrier Cells. *J Appl Phys* **1974**, *45* (1), 230–236. <https://doi.org/10.1063/1.1662965>.
- (3) Tang, C. W. Two-layer Organic Photovoltaic Cell. *Appl Phys Lett* **1986**, *48* (2), 183–185. <https://doi.org/10.1063/1.96937>.
- (4) Markina, A.; Lin, K.; Liu, W.; Poelking, C.; Firdaus, Y.; Villalva, D. R.; Khan, J. I.; Paleti, S. H. K.; Harrison, G. T.; Gorenflot, J.; Zhang, W.; De Wolf, S.; McCulloch, I.; Anthopoulos, T. D.; Baran, D.; Laquai, F.; Andrienko, D. Chemical Design Rules for Non-Fullerene Acceptors in Organic Solar Cells. *Adv Energy Mater* **2021**, *11* (44), 2102363. <https://doi.org/10.1002/aenm.202102363>.
- (5) Yu, G.; Gao, J.; Hummelen, J. C.; Wudl, F.; Heeger, A. J. Polymer Photovoltaic Cells: Enhanced Efficiencies via a Network of Internal Donor-Acceptor Heterojunctions. *Science (1979)* **1995**, *270* (5243), 1789–1791. <https://doi.org/10.1126/science.270.5243.1789>.
- (6) Sariciftci, N. S.; Smilowitz, L.; Heeger, A. J.; Wudl, F. Photoinduced Electron Transfer from a Conducting Polymer to Buckminsterfullerene. *Science (1979)* **1992**, *258* (5087), 1474–1476. <https://doi.org/10.1126/science.258.5087.1474>.
- (7) Ganesamoorthy, R.; Sathiyam, G.; Sakthivel, P. Review: Fullerene Based Acceptors for Efficient Bulk Heterojunction Organic Solar Cell Applications. *Solar Energy Materials and Solar Cells* **2017**, *161*, 102–148. <https://doi.org/10.1016/j.solmat.2016.11.024>.
- (8) Di Motta, S.; Siracusa, M.; Negri, F. Structural and Thermal Effects on the Charge Transport of Core-Twisted Chlorinated Perylene Bisimide Semiconductors. *The Journal of Physical Chemistry C* **2011**, *115* (42), 20754–20764. <https://doi.org/10.1021/jp207333y>.
- (9) Gogoi, G.; Bhattacharya, L.; Sahoo, S. R.; Sahu, S.; Sarma, N. Sen; Sharma, S. Enhancement of Air-Stability, π -Stacking Ability, and Charge Transport Properties

of Fluoroalkyl Side Chain Engineered n-Type Naphthalene Tetracarboxylic Diimide Compounds. *RSC Adv* **2021**, *11* (1), 57–70. <https://doi.org/10.1039/D0RA08345C>.

(10) Meng, Q.; Hu, W. Recent Progress of N-Type Organic Semiconducting Small Molecules for Organic Field-Effect Transistors. *Physical Chemistry Chemical Physics* **2012**, *14* (41), 14152. <https://doi.org/10.1039/c2cp41664f>.

(11) Gao, X.; Di, C.; Hu, Y.; Yang, X.; Fan, H.; Zhang, F.; Liu, Y.; Li, H.; Zhu, D. Core-Expanded Naphthalene Diimides Fused with 2-(1,3-Dithiol-2-Ylidene)Malonitrile Groups for High-Performance, Ambient-Stable, Solution-Processed n-Channel Organic Thin Film Transistors. *J Am Chem Soc* **2010**, *132* (11), 3697–3699. <https://doi.org/10.1021/ja910667y>.

(12) Vuk, D.; Radovanović-Perić, F.; Mandić, V.; Lovrinčević, V.; Rath, T.; Panžić, I.; Le-Cunff, J. Synthesis and Nanoarchitectonics of Novel Squaraine Derivatives for Organic Photovoltaic Devices. *Nanomaterials* **2022**, *12* (7), 1206. <https://doi.org/10.3390/nano12071206>.

(13) Strassel, K.; Hu, W.-H.; Osbild, S.; Padula, D.; Rentsch, D.; Yakunin, S.; Shynkarenko, Y.; Kovalenko, M.; Nüesch, F.; Hany, R.; Bauer, M. Shortwave Infrared-Absorbing Squaraine Dyes for All-Organic Optical Upconversion Devices. *Sci Technol Adv Mater* **2021**, *22* (1), 194–204. <https://doi.org/10.1080/14686996.2021.1891842>.

(14) Tonzola, C. J.; Kulkarni, A. P.; Gifford, A. P.; Kaminsky, W.; Jenekhe, S. A. Blue-Light-Emitting Oligoquinolines: Synthesis, Properties, and High-Efficiency Blue-Light-Emitting Diodes. *Adv Funct Mater* **2007**, *17* (6), 863–874. <https://doi.org/10.1002/adfm.200600542>.

(15) Mao, M.; Wang, J.-B.; Liu, X.-L.; Wu, G.-H.; Fang, X.-Q.; Song, Q.-H. Insight into the Effects of Modifying Chromophores on the Performance of Quinoline-Based Dye-Sensitized Solar Cells. *Spectrochim Acta A Mol Biomol Spectrosc* **2018**, *190*, 23–32. <https://doi.org/10.1016/j.saa.2017.09.002>.

(16) Aivali, S.; Tsimpouki, L.; Anastasopoulos, C.; Kallitsis, J. K. Synthesis and Optoelectronic Characterization of Perylene Diimide-Quinoline Based Small Molecules. *Molecules* **2019**, *24* (23), 4406. <https://doi.org/10.3390/molecules24234406>.

(17) Zhang, T.-T.; Jia, J.-F.; Wu, H.-S. Substituent and Solvent Effects on Electronic Structure and Spectral Property of $\text{ReCl}(\text{CO})_3(\text{N}\wedge\text{N})$ ($\text{N}\wedge\text{N}$ = Glyoxime): DFT

and TDDFT Theoretical Studies. *J Phys Chem A* **2010**, *114* (46), 12251–12257.

<https://doi.org/10.1021/jp104458u>.

(18) Rettig, I. D.; Halvorsen, K. M.; McCormick, T. M. Synthesis, Photophysical Characterization, and Aerobic Redox Reactivity of Electron-Rich Tellurorhodamine Photocatalysts. *Dalton Transactions* **2023**. <https://doi.org/10.1039/D2DT03534K>.

(19) Klein, B. P.; Ruppenthal, L.; Hall, S. J.; Sattler, L. E.; Weber, S. M.; Herritsch, J.; Jaegermann, A.; Maurer, R. J.; Hilt, G.; Gottfried, J. M. Topology Effects in Molecular Organic Electronic Materials: Pyrene and Azupyrene**. *ChemPhysChem* **2021**, *22* (11), 1065–1073. <https://doi.org/10.1002/cphc.202100222>.

(20) Zöphel, L.; Enkelmann, V.; Müllen, K. Tuning the HOMO–LUMO Gap of Pyrene Effectively via Donor–Acceptor Substitution: Positions 4,5 Versus 9,10. *Org Lett* **2013**, *15* (4), 804–807. <https://doi.org/10.1021/ol303476g>.

(21) Kasha, M. Energy Transfer Mechanisms and the Molecular Exciton Model for Molecular Aggregates. *Radiat Res* **1963**, *20* (1), 55. <https://doi.org/10.2307/3571331>.

(22) Yu, Y.-J.; Zhao, Y.; Ryu, S.; Brus, L. E.; Kim, K. S.; Kim, P. Tuning the Graphene Work Function by Electric Field Effect. *Nano Lett* **2009**, *9* (10), 3430–3434. <https://doi.org/10.1021/nl901572a>.

(23) Zhang, Z.; Huang, H.; Yang, X.; Zang, L. Tailoring Electronic Properties of Graphene by π – π Stacking with Aromatic Molecules. *J Phys Chem Lett* **2011**, *2* (22), 2897–2905. <https://doi.org/10.1021/jz201273r>.

(24) Zhang, X.-F.; Shao, X. π – π Binding Ability of Different Carbon Nano-Materials with Aromatic Phthalocyanine Molecules: Comparison between Graphene, Graphene Oxide and Carbon Nanotubes. *J Photochem Photobiol A Chem* **2014**, *278*, 69–74. <https://doi.org/10.1016/j.jphotochem.2014.01.001>.

(25) The Basics of UV-Vis Spectrophotometry. Agilent Technologies December 23, 2021.

(26) Introduction to Time-Resolved Spectroscopy With Applications in Biophysics and Physical Chemistry; 2015.

- (27) Elgrishi, N.; Rountree, K. J.; McCarthy, B. D.; Rountree, E. S.; Eisenhart, T. T.; Dempsey, J. L. A Practical Beginner's Guide to Cyclic Voltammetry. *J Chem Educ* **2018**, *95* (2), 197–206. <https://doi.org/10.1021/acs.jchemed.7b00361>.
- (28) Cardona, C. M.; Li, W.; Kaifer, A. E.; Stockdale, D.; Bazan, G. C. Electrochemical Considerations for Determining Absolute Frontier Orbital Energy Levels of Conjugated Polymers for Solar Cell Applications. *Advanced Materials* **2011**, *23* (20), 2367–2371. <https://doi.org/10.1002/adma.201004554>.
- (29) Wang, X.-Y.; Zhuang, F.-D.; Zhou, X.; Yang, D.-C.; Wang, J.-Y.; Pei, J. Influence of Alkyl Chain Length on the Solid-State Properties and Transistor Performance of BN-Substituted Tetrathienonaphthalenes. *J. Mater. Chem. C* **2014**, *2* (38), 8152–8161. <https://doi.org/10.1039/C4TC01369G>.
- (30) Lucas, F.; McIntosh, N.; Jacques, E.; Lebreton, C.; Heinrich, B.; Donnio, B.; Jeannin, O.; Rault-Berthelot, J.; Quinton, C.; Cornil, J.; Poriel, C. [4]Cyclo-N-Alkyl-2,7-Carbazoles: Influence of the Alkyl Chain Length on the Structural, Electronic, and Charge Transport Properties. *J Am Chem Soc* **2021**, *143* (23), 8804–8820. <https://doi.org/10.1021/jacs.1c03240>.
- (31) Liu, X.; Kim, Y. J.; Ha, Y. H.; Zhao, Q.; Park, C. E.; Kim, Y.-H. Effects of Alkyl Chain Length on the Optoelectronic Properties and Performance of Pyrrolo-Perylene Solar Cells. *ACS Appl Mater Interfaces* **2015**, *7* (16), 8859–8867. <https://doi.org/10.1021/acsami.5b01444>.
- (32) Suseela, Y. V.; Sasikumar, M.; Govindaraju, T. An Effective and Regioselective Bromination of 1,4,5,8-Naphthalenetetracarboxylic Dianhydride Using Tribromoisocyanuric Acid. *Tetrahedron Lett* **2013**, *54* (47), 6314–6318. <https://doi.org/10.1016/j.tetlet.2013.09.029>.
- (33) Robitaille, A.; Jenekhe, S. A.; Leclerc, M. Poly(Naphthalene Diimide-Alt-Bithiophene) Prepared by Direct (Hetero)Arylation Polymerization for Efficient All-Polymer Solar Cells. *Chemistry of Materials* **2018**, *30* (15), 5353–5361. <https://doi.org/10.1021/acs.chemmater.8b02160>.
- (34) Chen, S.-M.; Chang, L.-M.; Yang, X.-K.; Luo, T.; Xu, H.; Gu, Z.-G.; Zhang, J. Liquid-Phase Epitaxial Growth of Azapyrene-Based Chiral Metal–Organic Framework Thin Films for Circularly Polarized Luminescence. *ACS Appl Mater Interfaces* **2019**, *11* (34), 31421–31426. <https://doi.org/10.1021/acsami.9b11872>.

- (35) Zhang, Y.-Y.; Mi, J.-L.; Zhou, C.-H.; Zhou, X.-D. Synthesis of Novel Fluconazoliums and Their Evaluation for Antibacterial and Antifungal Activities. *Eur J Med Chem* **2011**, *46* (9), 4391–4402.
<https://doi.org/10.1016/j.ejmech.2011.07.010>.
- (36) Céspedes-Guirao, F. J.; Martín-Gomis, L.; Ohkubo, K.; Fukuzumi, S.; Fernández-Lázaro, F.; Sastre-Santos, Á. Synthesis and Photophysics of Silicon Phthalocyanine-Perylenebisimide Triads Connected through Rigid and Flexible Bridges. *Chemistry - A European Journal* **2011**, *17* (33), 9153–9163.
<https://doi.org/10.1002/chem.201100320>.
- (37) Chao, C.-C.; Leung, M.; Su, Y. O.; Chiu, K.-Y.; Lin, T.-H.; Shieh, S.-J.; Lin, S.-C. Photophysical and Electrochemical Properties of 1,7-Diaryl-Substituted Perylene Diimides. *J Org Chem* **2005**, *70* (11), 4323–4331.
<https://doi.org/10.1021/jo050001f>.
- (38) Sharma, S. V.; Pubill-Ulldemolins, C.; Marelli, E.; Goss, R. J. M. An Expedient, Mild and Aqueous Method for Suzuki–Miyaura Diversification of (Hetero)Aryl Halides or (Poly)Chlorinated Pharmaceuticals. *Organic Chemistry Frontiers* **2021**, *8* (20), 5722–5727. <https://doi.org/10.1039/D1QO00919B>.
- (39) Etheridge, F. S.; Fernando, R.; Golen, J. A.; Rheingold, A. L.; Sauve, G. Tuning the Optoelectronic Properties of Core-Substituted Naphthalene Diimides by the Selective Conversion of Imides to Monothioimides. *RSC Adv* **2015**, *5* (58), 46534–46539. <https://doi.org/10.1039/C5RA05920H>.
- (40) Hu, X.; Zuo, L.; Pan, H.; Hao, F.; Pan, J.; Fu, L.; Shi, M.; Chen, H. Synthesis and Photovoltaic Properties of N-Type Conjugated Polymers Alternating 2,7-Carbazole and Arylene Diimides. *Solar Energy Materials and Solar Cells* **2012**, *103*, 157–163.
<https://doi.org/10.1016/j.solmat.2012.04.041>.
- (41) Kozycz, L. M.; Gao, D.; Tilley, A. J.; Seferos, D. S. One Donor-Two Acceptor (D-A1)-(D-A2) Random Terpolymers Containing Perylene Diimide, Naphthalene Diimide, and Carbazole Units. *J Polym Sci A Polym Chem* **2014**, *52* (23), 3337–3345.
<https://doi.org/10.1002/pola.27395>.
- (42) Elhert, P. Synthesis of Light Harvesting Molecules Based on Squaraine Chromophores to Maximize Solar Absorption in Organic Photovoltaics. Master's Thesis, Norwegian University of Science and Technology, Trondheim, 2018.

- (43) Henden, M. Synthesis, Morphological and Photophysical Characterization of Squaraine Based Chromophores. Masters Thesis, Norwegian University of Science and Technology, Trondheim, 2019.
- (44) Schotten, C.; Nicholls, T. P.; Bourne, R. A.; Kapur, N.; Nguyen, B. N.; Willans, C. E. Making Electrochemistry Easily Accessible to the Synthetic Chemist. *Green Chemistry* **2020**, *22* (11), 3358–3375. <https://doi.org/10.1039/D0GC01247E>.
- (45) Aderne, R. E.; Borges, B. G. A. L.; Ávila, H. C.; von Kieseritzky, F.; Hellberg, J.; Koehler, M.; Cremona, M.; Roman, L. S.; Araujo, C. M.; Rocco, M. L. M.; Marchiori, C. F. N. On the Energy Gap Determination of Organic Optoelectronic Materials: The Case of Porphyrin Derivatives. *Mater Adv* **2022**, *3* (3), 1791–1803. <https://doi.org/10.1039/D1MA00652E>.
- (46) Rybakiewicz-Sekita, R.; Toman, P.; Ganczarczyk, R.; Drapala, J.; Ledwon, P.; Banasiewicz, M.; Skorka, L.; Matyjasiak, A.; Zagorska, M.; Pron, A. D-A-D Compounds Combining Dithienopyrrole Donors and Acceptors of Increasing Electron-Withdrawing Capability: Synthesis, Spectroscopy, Electropolymerization, and Electrochromism. *J Phys Chem B* **2022**, *126* (22), 4089–4105. <https://doi.org/10.1021/acs.jpcc.2c01772>.
- (47) Loutfy, R. O.; Hsiao, C. K.; Ong, B. S.; Keoshkerian, B. Electrochemical Evaluation of Electron Acceptor Materials. *Can J Chem* **1984**, *62* (10), 1877–1885. <https://doi.org/10.1139/v84-322>.
- (48) Eisenthal, K. B. Intermolecular and Intramolecular Excited State Charge Transfer. *Laser Chemistry* **1983**, *3* (1–6), 145–162. <https://doi.org/10.1155/LC.3.145>.
- (49) Campioli, E.; Sanyal, S.; Marcelli, A.; Di Donato, M.; Blanchard-Desce, M.; Mongin, O.; Painelli, A.; Terenziani, F. Addressing Charge-Transfer and Locally-Excited States in a Twisted Biphenyl Push-Pull Chromophore. *ChemPhysChem* **2019**, *20* (21), 2860–2873. <https://doi.org/10.1002/cphc.201900703>.
- (50) Wan, J.; Ferreira, A.; Xia, W.; Chow, C. H.; Takechi, K.; Kamat, P. V.; Jones, G.; Vullev, V. I. Solvent Dependence of the Charge-Transfer Properties of a Quaterthiophene–Anthraquinone Dyad. *J Photochem Photobiol A Chem* **2008**, *197* (2–3), 364–374. <https://doi.org/10.1016/j.jphotochem.2008.01.016>.

- (51) ACS Division of Organic Chemistry. Common Solvents Used in Organic Chemistry: Table of Properties.
- (52) Sigma-Aldrich. Physical Properties of Solvents.
- (53) Nehate, S. D.; Prakash, A.; Mani, P. D.; Sundaram, K. B. Work Function Extraction of Indium Tin Oxide Films from MOSFET Devices. *ECS Journal of Solid State Science and Technology* **2018**, 7 (3), P87–P90. <https://doi.org/10.1149/2.0081803jss>.
- (54) Helander, M. G.; Greiner, M. T.; Wang, Z. B.; Tang, W. M.; Lu, Z. H. Work Function of Fluorine Doped Tin Oxide. *Journal of Vacuum Science & Technology A: Vacuum, Surfaces, and Films* **2011**, 29 (1), 011019. <https://doi.org/10.1116/1.3525641>.
- (55) Helander, M. G.; Wang, Z. B.; Qiu, J.; Lu, Z. H. Band Alignment at Metal/Organic and Metal/Oxide/Organic Interfaces. *Appl Phys Lett* **2008**, 93 (19), 193310. <https://doi.org/10.1063/1.3030979>.
- (56) Bernède, J. C.; Cattin, L.; Djobo, S. O.; Morsli, M.; Kanth, S. R. B.; Patil, S.; Leriche, P.; Roncali, J.; Godoy, A.; Diaz, F. R.; del Valle, M. A. Influence of the Highest Occupied Molecular Orbital Energy Level of the Donor Material on the Effectiveness of the Anode Buffer Layer in Organic Solar Cells. *physica status solidi (a)* **2011**, 208 (8), 1989–1994. <https://doi.org/10.1002/pssa.201127047>.
- (57) Lai, T.-H.; Tsang, S.-W.; Manders, J. R.; Chen, S.; So, F. Properties of Interlayer for Organic Photovoltaics. *Materials Today* **2013**, 16 (11), 424–432. <https://doi.org/10.1016/j.mattod.2013.10.001>.

6 Supplemental Information

SI 1 NMR spectra

Taken on a Bruker Avance III HD systems, with a 5 mm Smart-Probe Z-gradient probe. Spectra are indicated with † for 400 MHz and ‡ for 600 MHz

SI 1.1 NDI

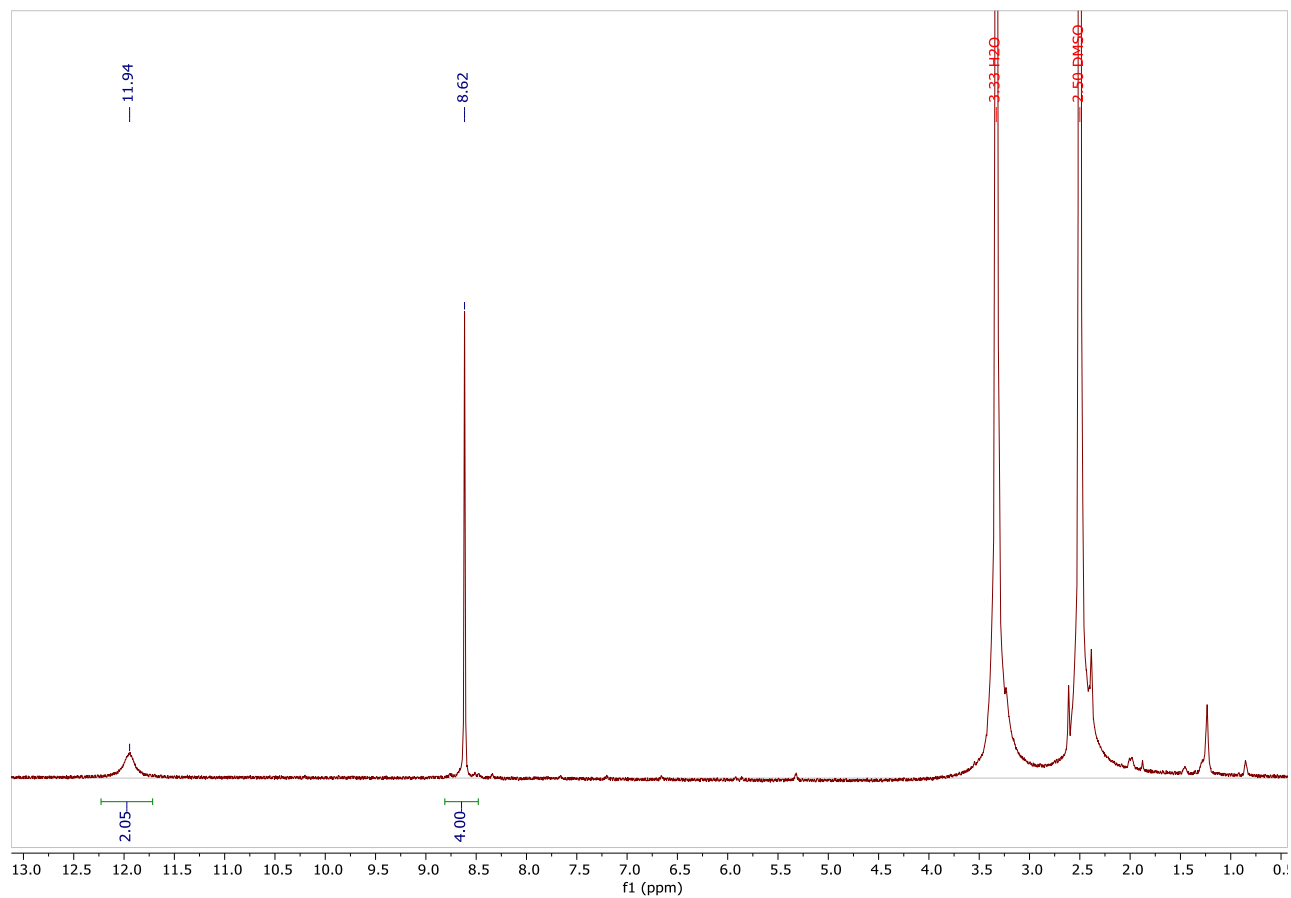
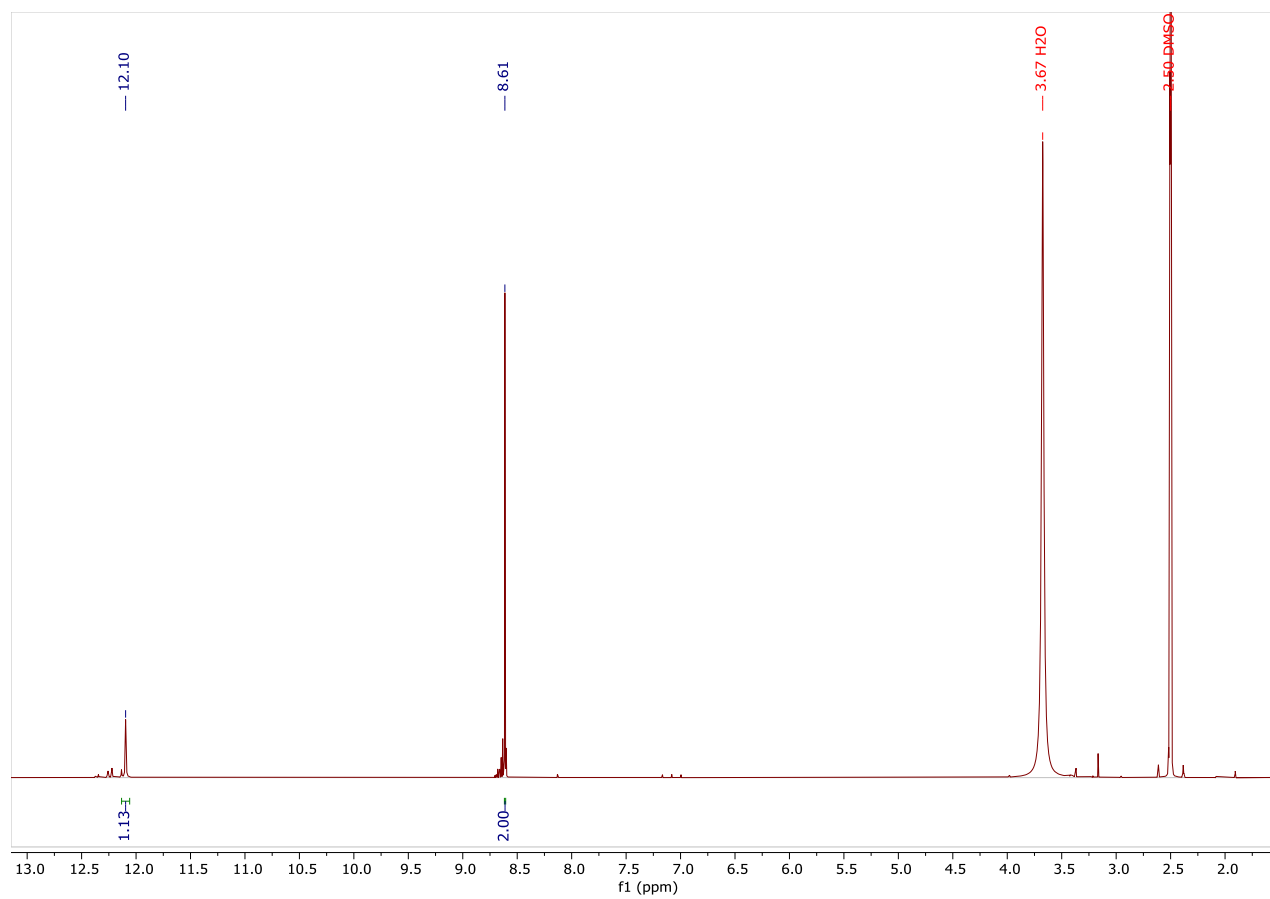
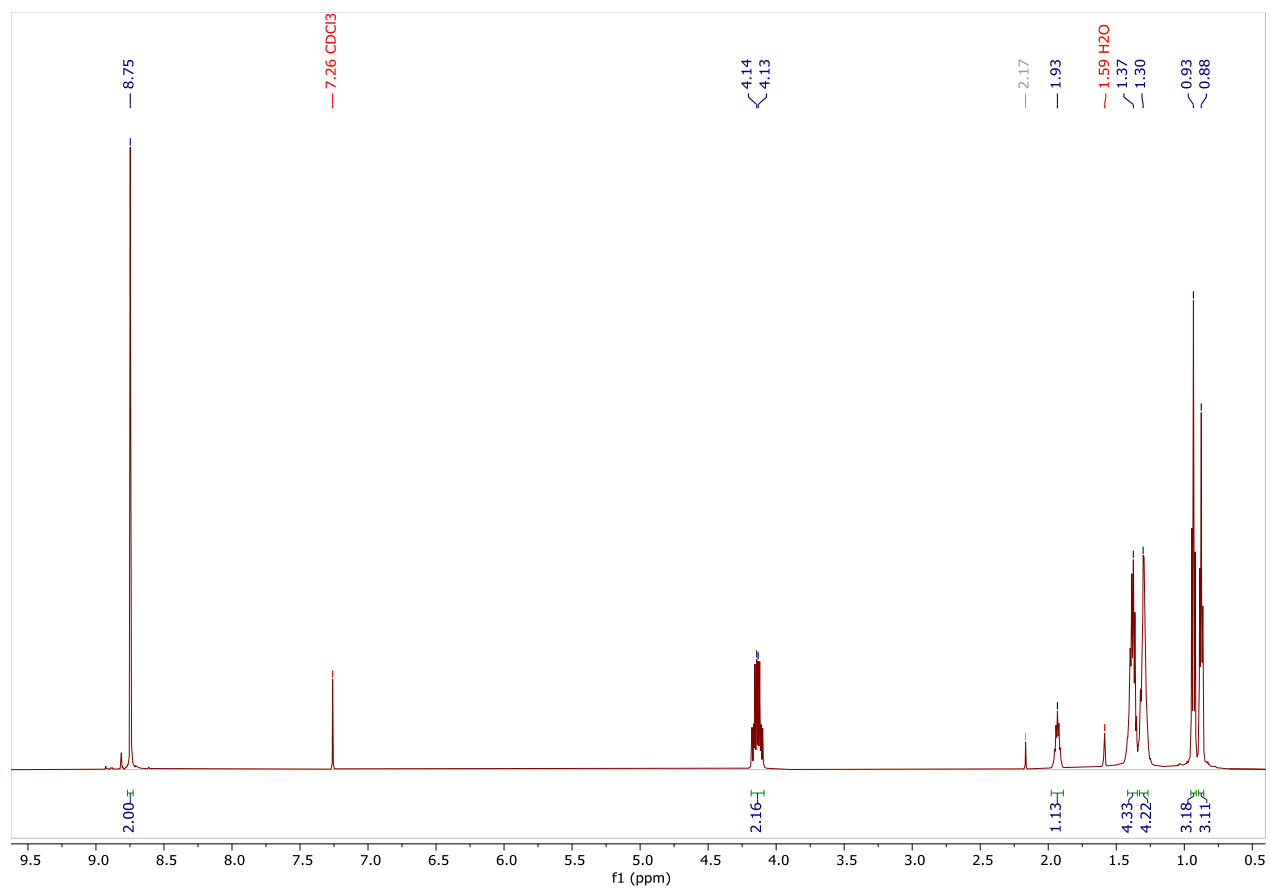


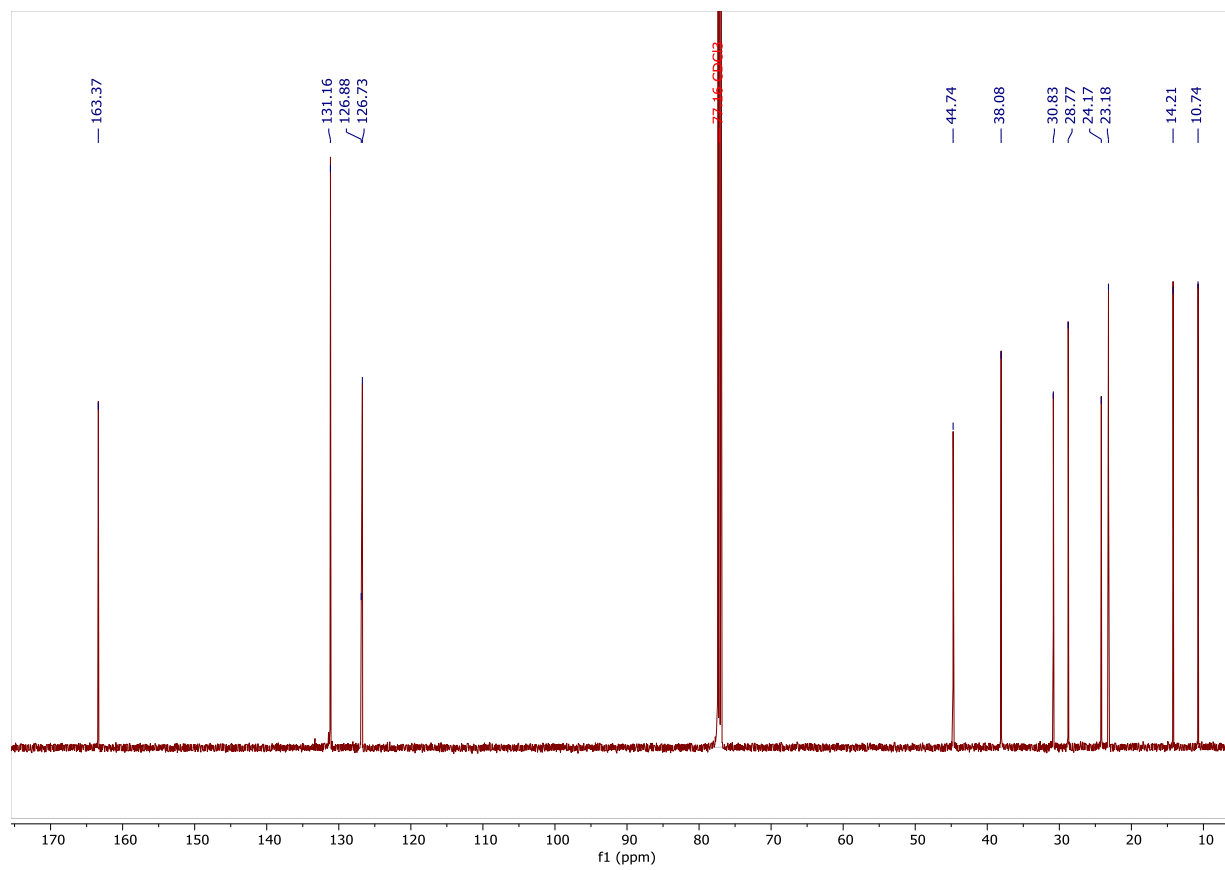
Figure 30: ^1H NMR of NDI in d_6 -DMSO ‡

SI 1.2 2Br-NDI

Figure 31: ^1H NMR of 2Br-NDI in d_6 -DMSO †

SI 1.3 EtHex-NDI

Figure 32: ^1H NMR of EtHex-NDI in CDCl_3

Figure 33: ^{13}C NMR of EtHex-NDI in CDCl_3

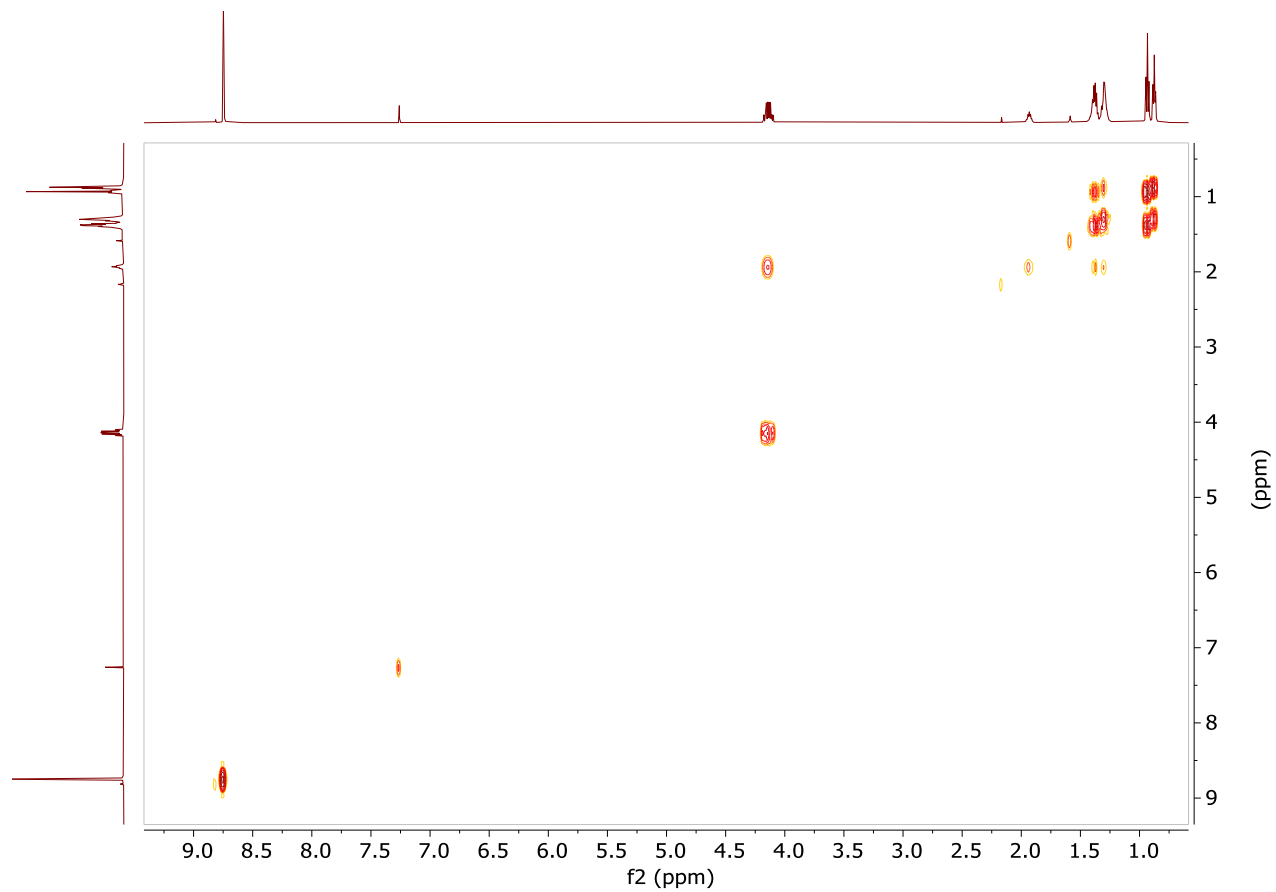
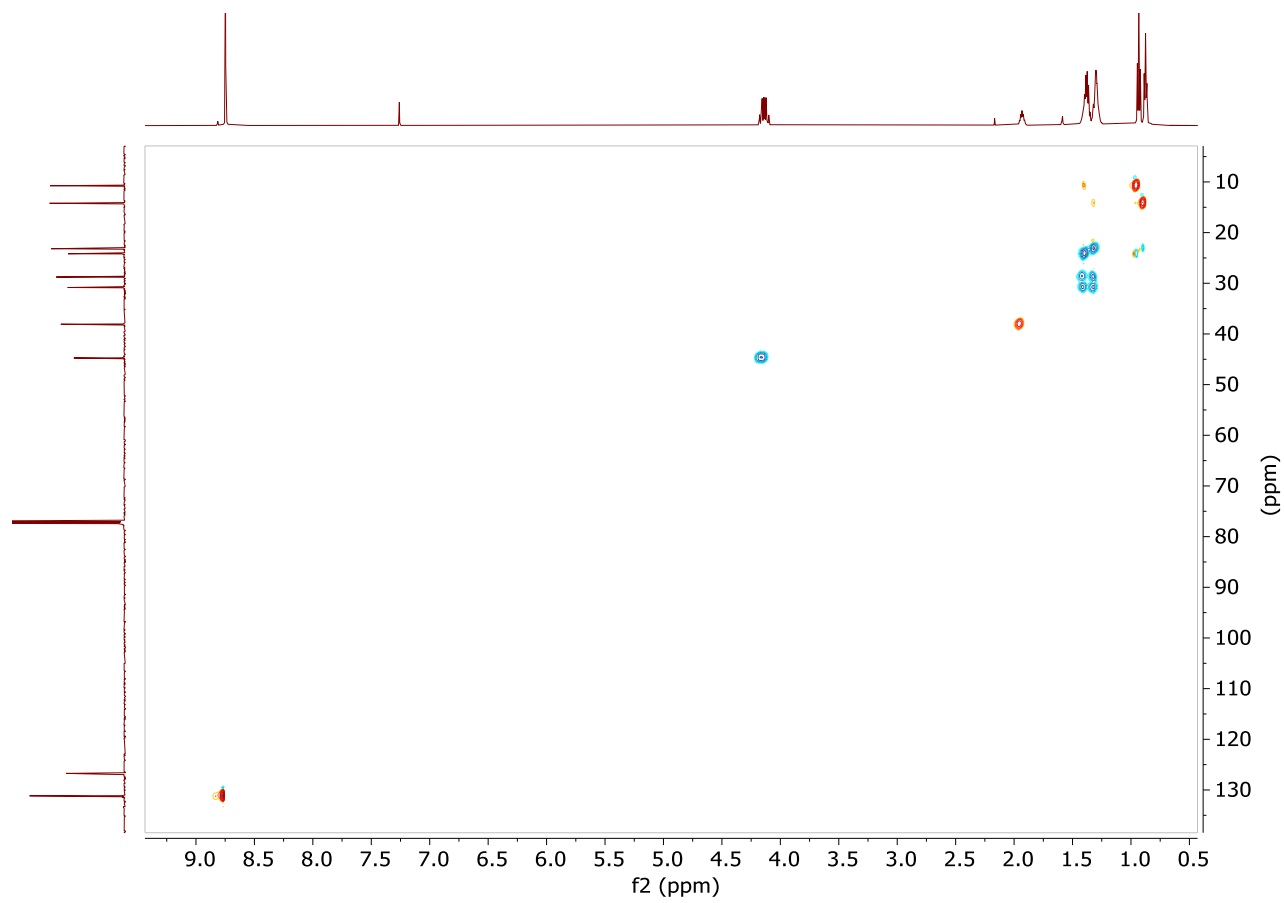
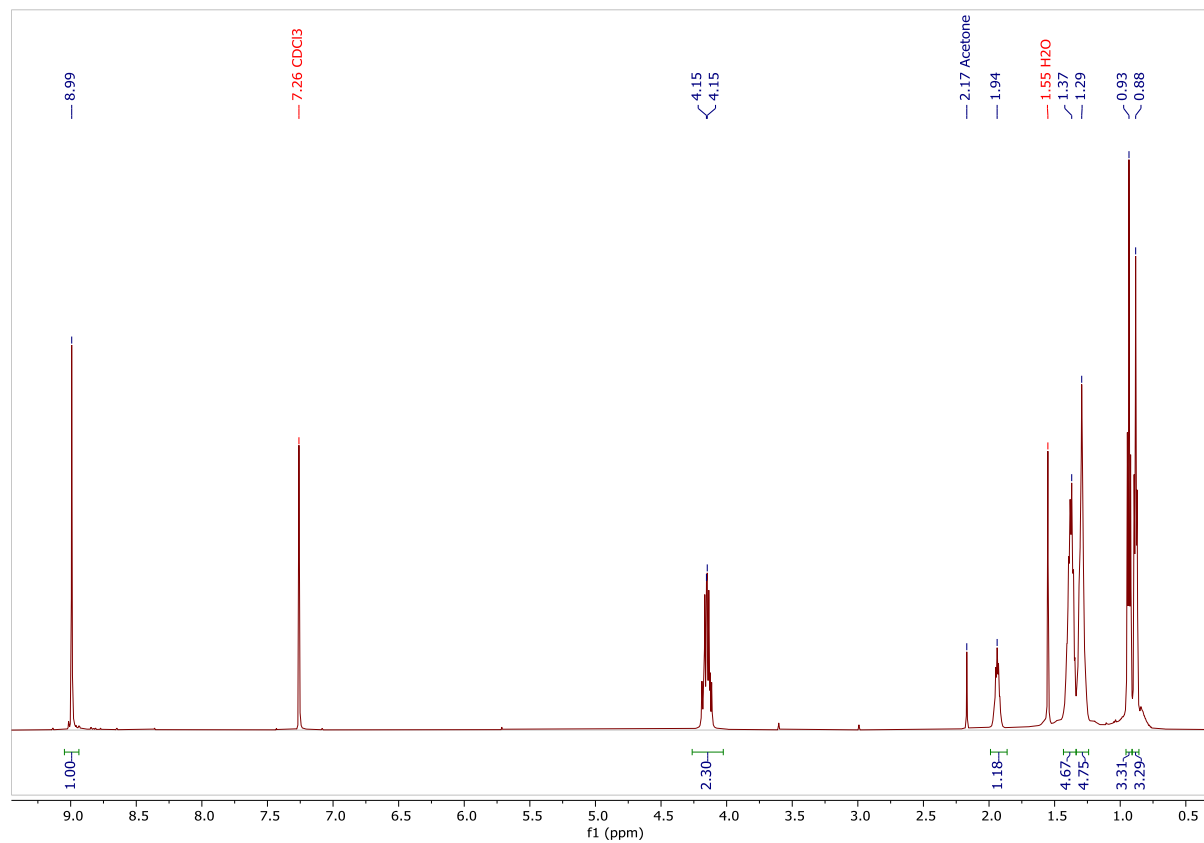
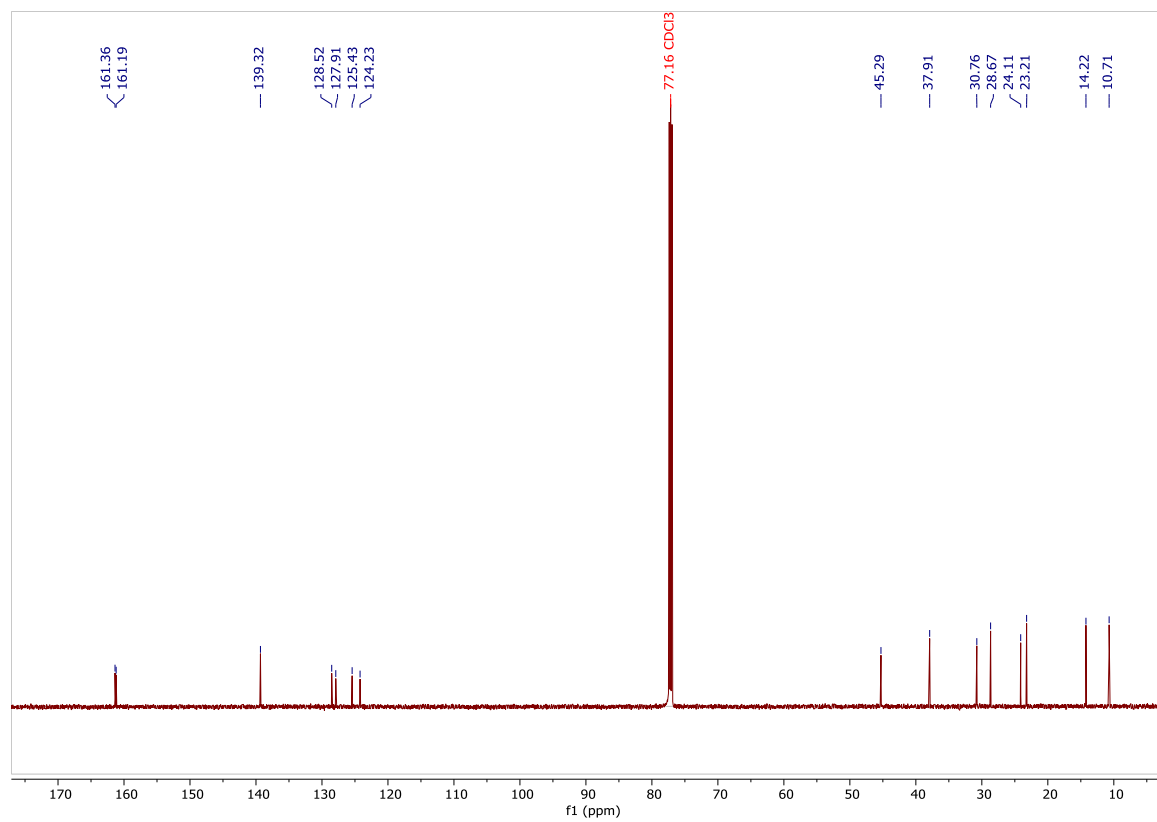


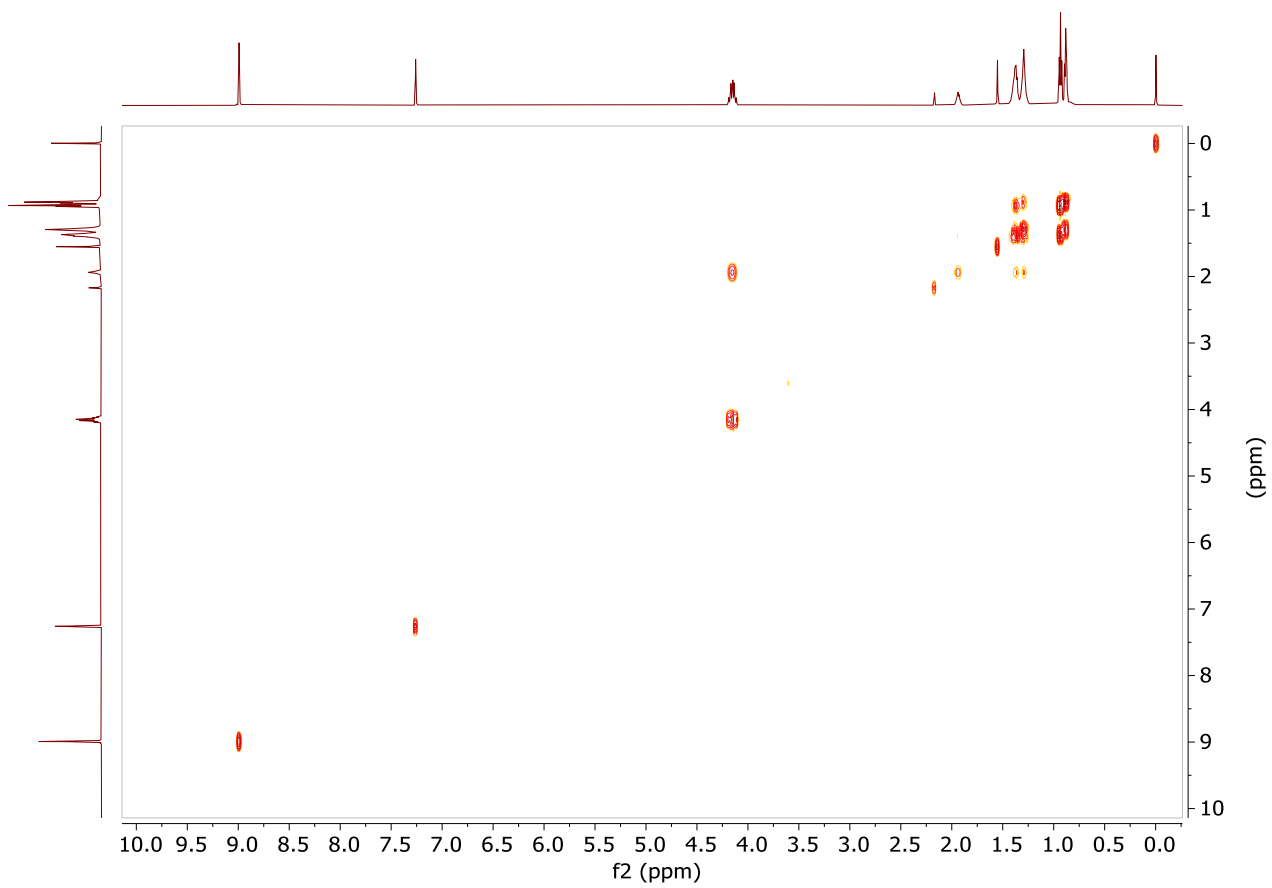
Figure 34: COSY NMR of EtHex-NDI in CDCl_3

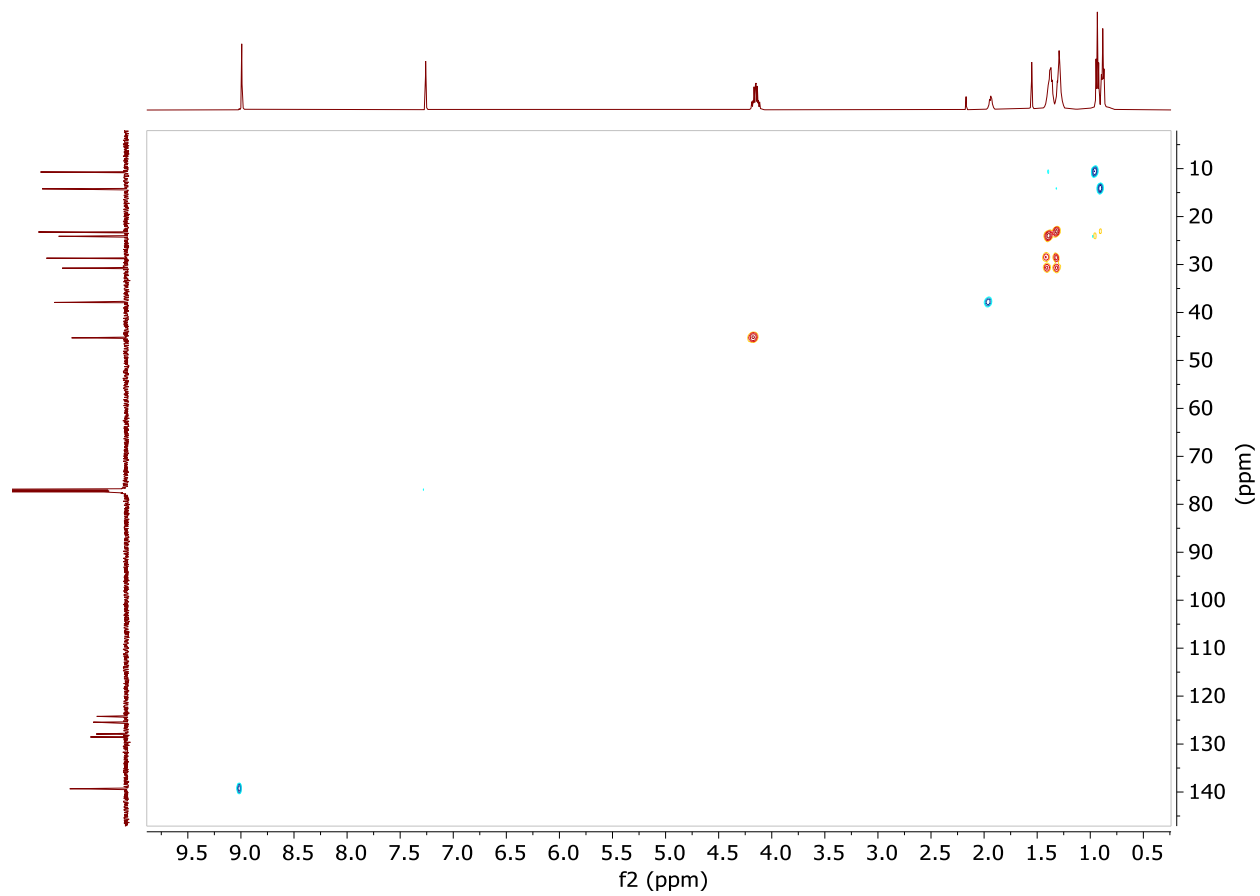
Figure 35: HSQC NMR of EtHex-NDI in CDCl₃†

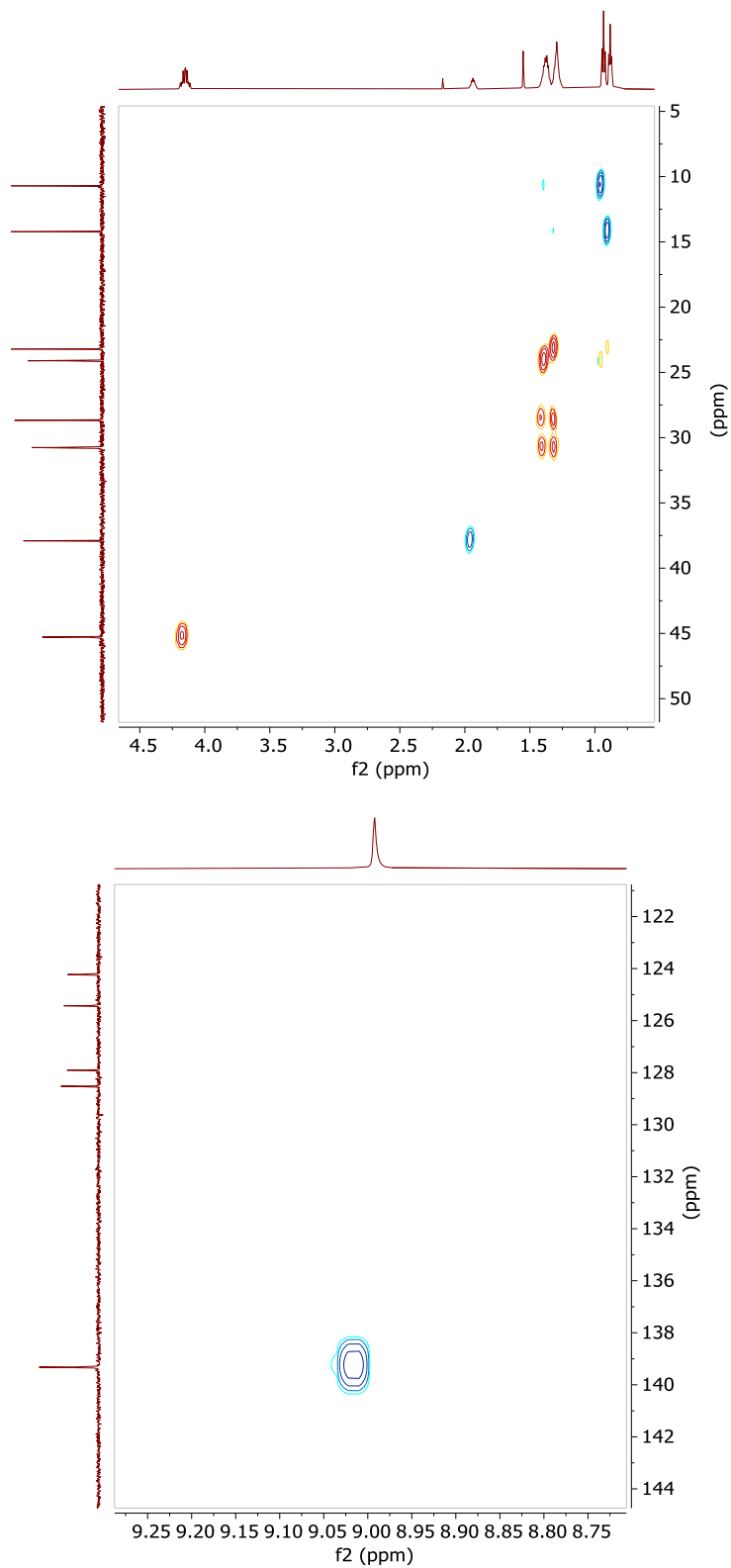
SI 1.4 EtHex-2BrNDI

Figure 36: ^1H NMR of EtHex-2BrNDI in CDCl_3

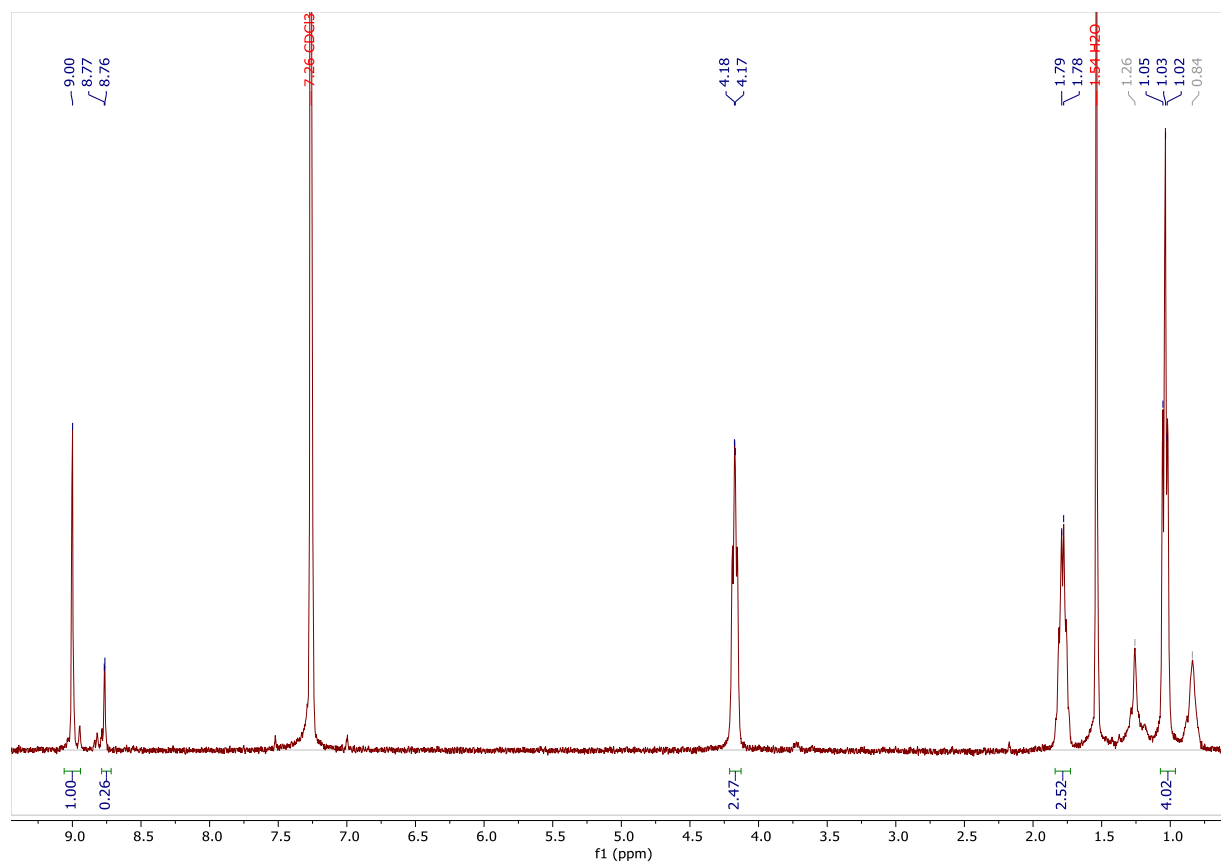
Figure 37: ^{13}C NMR of EtHex-NDI in CDCl_3

Figure 38: COSY NMR of EtHex-NDI in CDCl_3

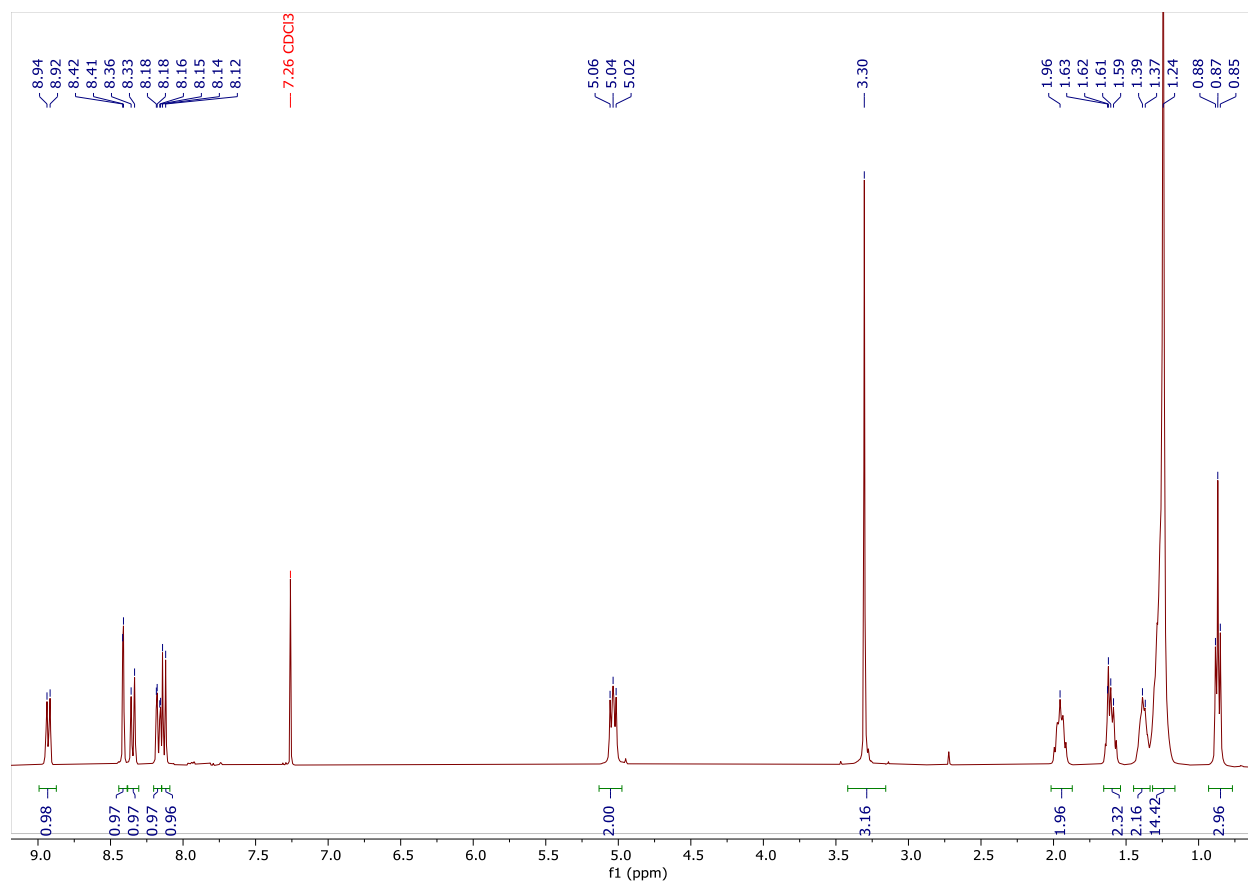
Figure 39: HSQC NMR (full) of EtHex-NDI in CDCl_3

Figure 40: HSQC NMR (upper: alkyl region, lower: aromatic region) of EtHex-NDI in CDCl₃†

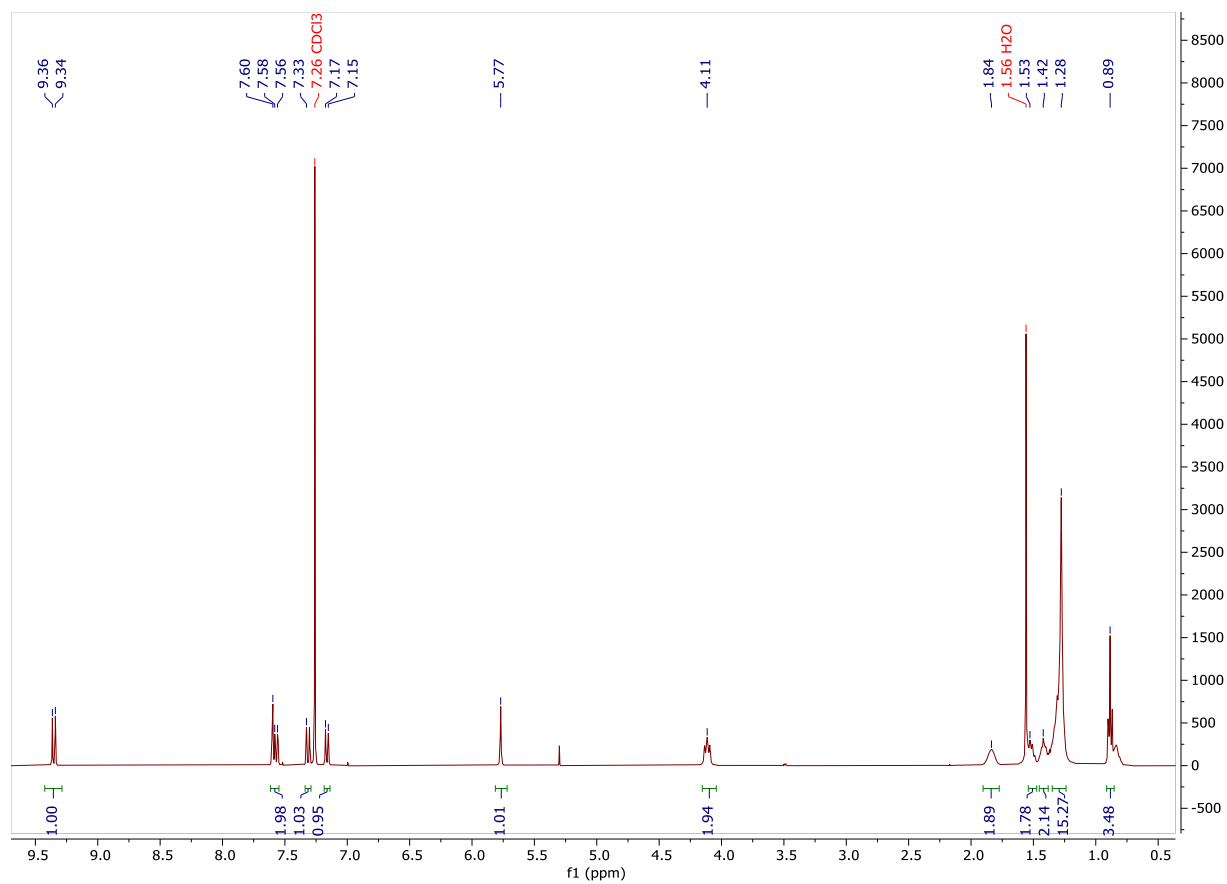
SI 1.5 Isopropyl-2BrNDI

Figure 41: ^1H NMR of Isopropyl-2BrNDI in CDCl_3

SI 1.6 IDQ

Figure 42: ¹H NMR of IDQ in CDCl₃ †

SI 1.7 IDQ-SQ

Figure 43: ^1H NMR of IDQ-SQ in CDCl_3 †

SI 1.8 IDQ-SQ-P

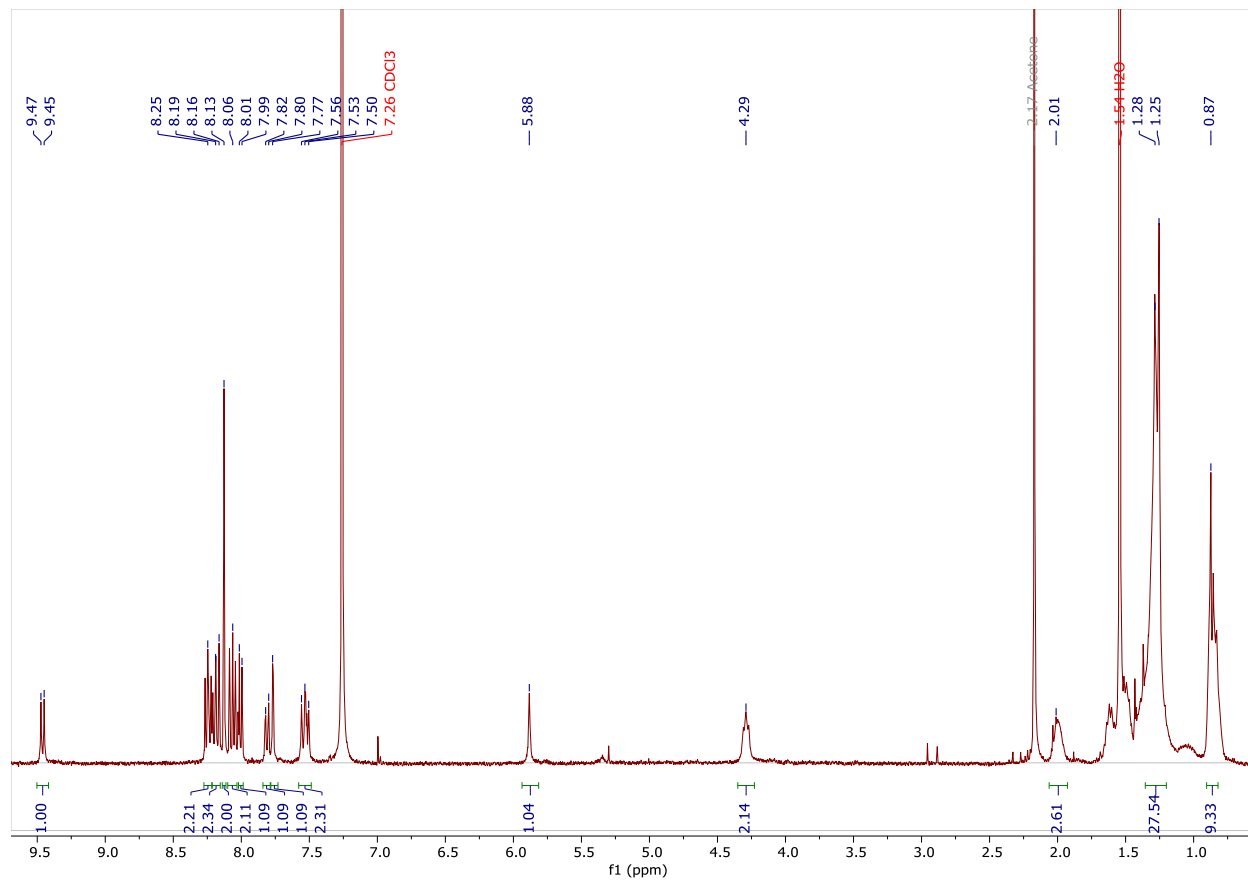
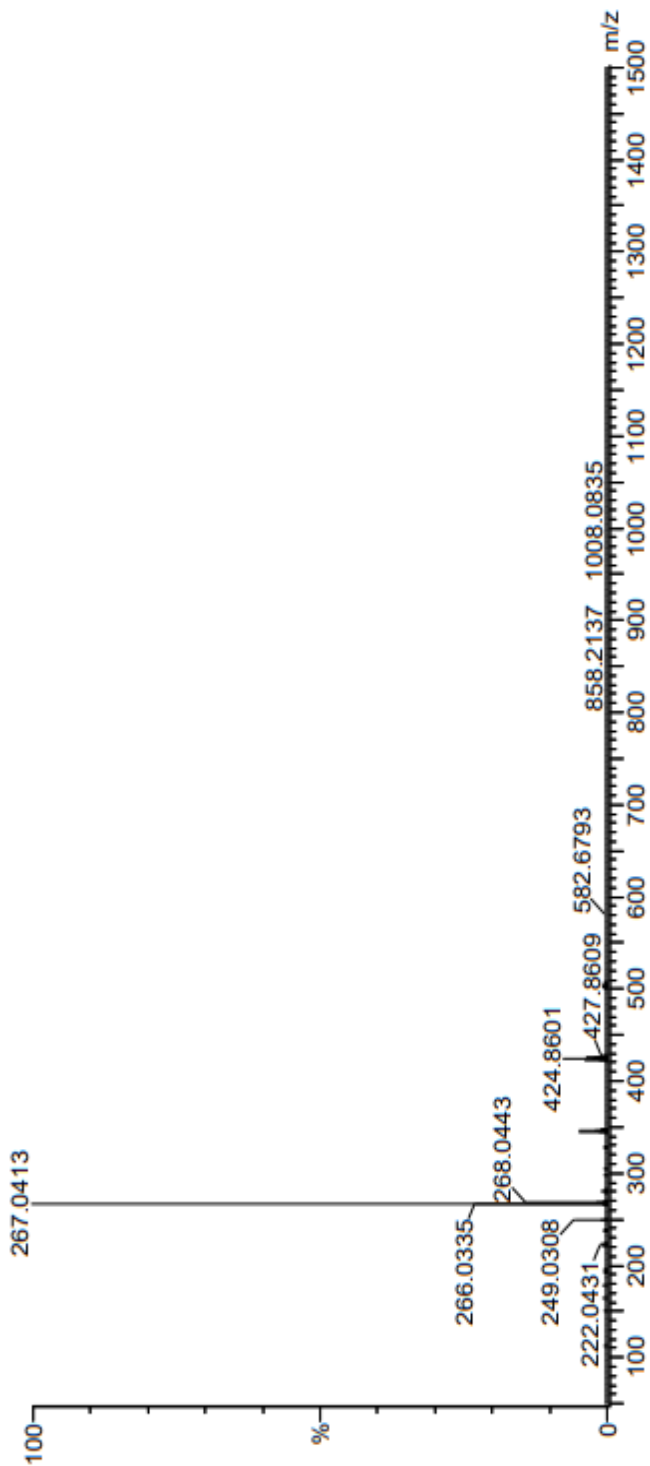


Figure 44: ¹H NMR of IDQ-SQ-P†

SI 2 Mass Spectrometry

2.1 Even Electron Mass Spectrum of 2Br-NDI





 **NTNU**

Norwegian University of
Science and Technology